Electron- versus neutrino-nucleus scattering

(Article begins on next page)

19 April 2024

Electron- versus neutrino-nucleus scattering

J.E. Amaro,[1] M.B. Barbaro,[2] J.A. Caballero,[3] R. González-Jiménez,[4] G.D. Megias,[5, 3] and I. Ruiz Simo[1]

[1]*Departamento de Física Atómica, Molecular y Nuclear,*
and Instituto de Física Teórica y Computacional Carlos I, Universidad de Granada, Granada 18071, Spain
[2]*Dipartimento di Fisica, Università di Torino and INFN,*
Sezione di Torino, Via P. Giuria 1, 10125 Torino, Italy
[3]*Departamento de Física Atómica, Molecular y Nuclear, Universidad de Sevilla, 41080 Sevilla, Spain*
[4]*Grupo de Física Nuclear, Departamento de Estructura de la Materia,*
Física Térmica y Electrónica, Facultad de Ciencias Físicas,
Universidad Complutense de Madrid and IPARCOS, Madrid 28040, Spain
[5]*University of Tokyo, Institute for Cosmic Ray Research,*
Research Center for Cosmic Neutrinos, Kashiwa, Japan
(Dated: July 14, 2020)

We illustrate the connection between electron and neutrino scattering off nuclei and show how the former process can be used to constrain the description of the latter. After reviewing some of the nuclear models commonly used to study lepton-nucleus reactions, we describe in detail the SuSAv2 model and show how its predictions compare with the available electron- and neutrino-scattering data over the kinematical range going from the quasi-elastic peak to pion-production and highly inelastic scattering.

Contents

I. Introduction

Electron scattering is a powerful probe to study the internal structure of atomic nuclei, due to the weakness of the electromagnetic interaction as compared to the strong forces [1, 2]. In the last years the field has seen renewed interest due to its connection to neutrino-nucleus scattering and the importance of nuclear physics for the interpretation of long baseline neutrino oscillation experiments [3, 4]. These experiments (MiniBooNE, T2K, NOvA, DUNE, T2HK, ...), will improve our knowledge of the Pontecorvo-Maki-Nakagawa-Sakata matrix, in particular the CP-violating phase which is related to the matter-antimatter asymmetry in the Universe. The achievement of the general goal requires a good control of the systematic uncertainties coming from the modelling of neutrino-nucleus interactions. Hence the accurate description of these reactions has become one of the top challenges for theoretical nuclear physics [3].

In the energy regime of the above mentioned experiments, going from about 100 MeV up to a few GeV, several mechanisms contribute to the nuclear response: from the excitation of nuclear collective states in the lowest energy part of the spectrum, up to the deep inelastic scattering at the highest energy transfers, encompassing the quasi-elastic region, corresponding to one-nucleon knockout, and the resonance region, corresponding to the excitation of nucleon resonances followed by their decay and subsequent production of pions and other mesons. Nuclear models should be able to describe, as consistently as possible, all these processes with a few percent accuracy, a very challenging task. Moreover, these models should be relativistic, as requested by the high energies involved in the experimental setup.

Due to the rareness of previous neutrino-nucleus experiments in this energy regime, nuclear models must be validated against electron scattering experiments, closely related to neutrino scattering. The huge amount of electron scattering data allows to discriminate between theoretical models much better than comparing with neutrino scattering data. Therefore, it is mandatory that any model used in the analysis of neutrino oscillation experiment is first validated against electron scattering data. In this paper we focus on the connection between these two processes, illustrating and comparing some of the models used to describe them simultaneously.

The paper is organized as follows: in Sect. II we introduce the general formalism for lepton-nucleus scattering and we comment on the similarities and differences between the electron and neutrino cases. In Sect. III we present different models for the quasielastic (QE) reaction, going from the simplest Relativistic Fermi Gas to more realistic descriptions of the nucleus. Then we discuss relativistic models for the reactions occurring at higher energy transfer: two-particle-two-hole (2p2h) excitations (Sect. IV), pion production (Sect. V), higher inelastic and deep inelastic scattering (Sect. VI). In Sect. VII we concentrate on the SuSAv2 model, developed by our group for both electron and neutrino reactions, collecting in a coherent way the main results obtained in our past work and illustrating the possible implementation of the model in Monte Carlo generators. Finally, in Sect. VIII, we draw our conclusions and outline the future developments of our approach.

II.   Connecting electron and neutrino scattering

In order to emphasize the similarities and differences between electron- and (anti)neutrino-nucleus scattering, here we present in parallel the general formalism for the two processes. Let us consider the scattering problem

$$l + A \rightarrow l' + X + B$$

where an incident lepton l of mass m and 4-momentum $K^\mu = (\epsilon, \mathbf{k})$ [1] scatters off a nuclear target of mass number A (a nucleus or a single nucleon) and a lepton l' of mass m' and 4-momentum $K'^\mu = (\epsilon', \mathbf{k}')$ emerges, with $\epsilon = \sqrt{\mathbf{k}^2 + m^2}$ and $\epsilon' = \sqrt{\mathbf{k}'^2 + m'^2}$, together with a system X and residual nucleus B.

For electron scattering $m = m' = m_e$, whereas for neutrino scattering $m = m_{\nu_l}$ and $m' = m_l$ for charged-current (CC) processes, where a W boson is exchanged, or $m' = m_{\nu_l}$ for neutral-current (NC) processes, associated to the exchange of a Z^0 boson.

Three kinds of cross sections can be considered in these reactions: (i) The *inclusive* cross section (l, l'), where only the outgoing lepton is detected. It corresponds to the integration over all the final particles, except the outgoing lepton, and a sum over all open channels compatible with the kinematics. (ii) The *semi-inclusive* cross section $(l, l'X)$, which corresponds to detecting, in coincidence, the lepton l' and the particle (or a system of particles) X. (iii) Finally, the *exclusive* cross section, corresponding to the simultaneous detection of *all* the final scattering products.

Exclusive processes are more challenging from both experimental and theoretical points of view: they are more difficult to measure and more sensitive to the details of the nuclear model description. Different nuclear models can describe equally well inclusive data, while exclusive or semi-inclusive data constitute a more stringent test for the validity of a model and can better discriminate between different theories.

In this article we mainly focus on the case of inclusive reactions, where more data are available and nuclear models are more solid. It should be kept in mind, however, that the validity of nuclear models is better tested against semi-inclusive and exclusive data, and that a good description of the latter is desirable for models to be implemented in Monte Carlo generators used to analyze neutrino oscillation experiments.

In Born approximation [5, 6] the lepton-nucleus differential cross section $d\sigma$ is proportional to the contraction of the leptonic $(\eta_{\mu\nu})$ and hadronic $(W^{\mu\nu})$ tensors, defined as

$$\eta_{\mu\nu}(K, K') = 2mm' \overline{\sum}_{ss'} j_\mu^*(K's', Ks) j_\nu(K's', Ks) \tag{1}$$

$$W^{\mu\nu} = \overline{\sum}_{SS'} J_{S'S}^{\mu\,*} J_{S'S}^\nu, \tag{2}$$

---

[1] In this paper we shall use the units $\hbar = c = 1$.

where $j^\mu_{s's}$ and $J^\mu_{S'S}$ are the leptonic and hadronic 4-current matrix elements, respectively. The symbol $\overline{\sum}$ represents average and sum over the initial and final leptonic (s, s') or hadronic (S, S') spin quantum numbers if the initial lepton and hadron are not polarized and the final polarizations are not measured.

The leptonic current entering the tensor $\eta^{\mu\nu}$ can be written as

$$j^\mu(K's', Ks) = \overline{u}(K', s')(a_V \gamma^\mu + a_A \gamma^\mu \gamma_5)u(K, s), \tag{3}$$

where $u(K, s)$ is the lepton Dirac spinor and, according to the Standard Model of electroweak interactions, $a_V = 1$ while $a_A = 0$ for unpolarized electron scattering (assuming only pure electromagnetic interaction [2]) and $a_A = \mp 1$ in the neutrino ($-$) or antineutrino ($+$) case. By inserting Eq. (3) into (1) and performing the traces one gets

$$\eta_{\mu\nu}(K, K') = \eta_{\mu\nu}^{VV} + \eta_{\mu\nu}^{AA} + \eta_{\mu\nu}^{VA} \tag{4}$$

with

$$\eta_{\mu\nu}^{VV} = a_V^2 \left[K_\mu K'_\nu + K'_\mu K_\nu - g_{\mu\nu} \left(K \cdot K' - mm' \right) \right] \tag{5}$$

$$\eta_{\mu\nu}^{AA} = a_A^2 \left[K_\mu K'_\nu + K'_\mu K_\nu - g_{\mu\nu} \left(K \cdot K' + mm' \right) \right] \tag{6}$$

$$\eta_{\mu\nu}^{VA} = -2ia_V a_A \varepsilon_{\mu\nu\alpha\beta} K^\alpha K'^\beta, \tag{7}$$

where the upper labels VV, AA and VA correspond to the vector-vector, axial-axial, and vector-axial components of the leptonic tensor.

The number of variables upon which the hadronic tensor $W^{\mu\nu}$, and hence the differential cross section, depend varies with the type of reaction considered: the inclusive (l, l') cross section is a function of only 2 independent kinematic variables, *e.g.* the energy and scattering angle of the outgoing lepton; the semi-inclusive $(l, l'N)$ cross section, where the final lepton and a nucleon N are detected in coincidence, depends on 5 variables, and so on. For semi-inclusive processes in which n final particles are detected beyond the lepton, the kinematical variables are $2+3n$. Therefore the degree of complexity of nuclear response increases with the "exclusiveness" of the process.

The number of components of the complex, hermitian ($W^{\mu\nu*} = W^{\nu\mu}$), hadronic matrix contributing to the cross section also depends on the specific process. In the most general case, the contraction $\eta_{\mu\nu}W^{\mu\nu}$ gives rise to 16 independent terms. These are usually organized into real linear combinations of the hadronic tensor components, the *nuclear response functions*

$$R_K, \qquad K = CC, CL, LL, T, TT, TC, TL, T', TC', TL', \underline{TT}, \underline{TC}, \underline{TL}, \underline{CL'}, \underline{TC'}, \underline{TL'}, \tag{8}$$

where the labels C, L, T and T' correspond to a reference frame where the z-axis ($\mu = 3$) is parallel to the momentum transfer $\mathbf{q} = \mathbf{k} - \mathbf{k}'$ and refer to the charge ($\mu = 0$), longitudinal ($\mu = 3$) and transverse ($\mu = 1, 2$) projections of the two currents building up the response. A similar decomposition can be performed for the leptonic tensor, in such a way that the tensor contraction can be written as

$$\eta_{\mu\nu}W^{\mu\nu} = v_0 \sum_K V_K R_K, \tag{9}$$

where the coefficients $v_0 V_K$ are linear combinations of the leptonic tensor components. Their explicit expressions are given in Sect. III.

In the case of semi-inclusive unpolarized electron scattering (pure electromagnetic interaction), due to absence of axial current and to the conservation of the vector current (CVC), the response functions reduce to 4:

$$d\sigma(e, e'N) \propto V_L R_L + V_T R_T + V_{TT} R_{TT} + V_{TL} R_{TL}. \tag{10}$$

In the case of inclusive lepton scattering, as a consequence of the integration over the full phase space of the outgoing hadron, some of the responses do not contribute and one has:

$$d\sigma(\nu_l, l') \propto V_{CC} R_{CC} + 2V_{CL} R_{CL} + V_{LL} R_{LL} + V_T R_T + V_{T'} R_{T'} \tag{11}$$

$$d\sigma(e, e') \propto V_L R_L + V_T R_T. \tag{12}$$

In the neutrino case, each response can be decomposed as

$$R_K = R_K^{VV} + R_K^{AA} + R_K^{VA} \tag{13}$$

where the upper labels denote the vector or axial nature of the two hadronic currents entering the response in Eq. (2). The above decomposition into response functions is valid in all kinematical regions (elastic, quasielastic, 2p2h excitations, inelastic), characterized by different nuclear currents. Further details for the response functions will be illustrated in Section III, where calculations of the quasielastic electromagnetic and weak cross sections will be presented in some specific nuclear models.

---

[2] Electrons can also interact weakly: in this case $a_V = 4\sin^2\theta_W - 1$ and $a_A = -1$.

What can we learn from electron scattering?

The formalism presented above shows that electron and neutrino scattering are closely related and validation against electron scattering data constrains models to be applied to neutrino scattering. Comparison with inclusive electron scattering data is a necessary, but not sufficient, test for nuclear models, because of two main differences:

- The weak current carried by neutrinos has a vector and an axial component, while the electromagnetic current is purely vector. As a consequence, neutrinos can probe the axial nuclear response, not accessible via unpolarized electron scattering. This introduces uncertainties related to the knowledge of the axial and pseudoscalar form factors. In principle valuable information on the axial response could also be extracted from parity-violating (PV) electron scattering off nuclei [7–9], which could also provide important complementary information on nuclear correlations [10–13] and on the radiative corrections entering in the isovector axial-vector sector [14]. However, few PV data on medium-heavy nuclei exist and are mostly limited to the elastic part of the spectrum.

- In typical electron scattering experiments the incident beam energy is known with good accuracy, hence the transferred energy, ω, and momentum, q, can be precisely determined by measuring the outgoing lepton kinematics. In long baseline neutrino experiments the beam is not monochromatic: neutrinos are produced from meson decay with a more or less - depending on the experiment - broad distribution around an average value. This implies that each kinematic (momentum and scattering angle) of the outgoing lepton corresponds in general to a finite range of ω and q, which can in turn correspond to various overlapping processes. An important example of this difference is represented by the mixing of 1p1h and 2p2h excitations: in the (e, e') the former correspond to the quasielastic peak, while the latter are peaked in the "dip" region between the QE and the Δ resonance peaks. In (ν_l, l) data there is no way to disentangle the two channels and one has to rely on nuclear models to reconstruct the neutrino energy from lepton kinematics.

A large set of high quality inclusive electron-nucleus scattering data has been collected in the past [15], covering an energy range from 100 MeV to several GeV, and various nuclei (from ^3He up to ^{238}U). Recently [16, 17] the (e, e') cross section on argon and titanium has been measured at JLab, with the specific purpose of constraining models used in the analysis of neutrino-nucleus scattering. Some data are also available for the separated longitudinal and transverse responses. These response functions allow for a more stringent test of the models because nuclear effects are different in the two channels.

Inclusive electron-nucleus scattering and Superscaling

A powerful mean of extracting information on nuclear effects from (e, e') data at different beam energies and on different nuclei is the superscaling analysis proposed in [18–20]. This approach factorizes the cross section into a single-nucleon term times a function - the *scaling function* - which embodies the nuclear dynamics. Assuming that the latter is independent of the specific probe, scaling allows one to predict inclusive neutrino-nucleus cross sections using electron-nucleus data [21].

Scaling phenomena occur in various different fields, including atomic, nuclear and hadronic physics, whenever a new scale is probed in a certain process. For example, x-scaling occurs in lepton-nucleon scattering when the lepton, at high values of Q^2, is resolving the inner structure of the proton (or neutron), interacting with its constituents, the quarks. Scaling manifests when the nucleon's structure function, $F_{1,2}(Q^2, \nu)$, becomes a function of only one variable (in this case the Bjorken variable x). In lepton-nucleus scattering scaling occurs when the nuclear response, depending in general on the two variables q, ω, becomes function of only one scaling variable, indicating that the probe interacts with the nucleus' constituents, the nucleons. Since these, unlike the quarks, are not point-like, the cross section has to be "reduced", *i.e.*, divided by a single-nucleon function which takes into account the internal structure of the nucleon. In this context the *scaling function* is defined as the ratio between the double differential cross section and a single-nucleon cross section $\overline{\sigma_{eN}}$:

$$f(q, \omega) = \frac{k_F}{\overline{\sigma_{eN}}} \frac{d^2\sigma}{d\Omega_e d\omega}. \tag{14}$$

The single-nucleon cross section is not unique and takes into account the added contribution from all the separate nucleons in average. In this work we use a single nucleon cross section averaged over the relativistic Fermi gas to take into account that the initial nucleon is not at rest:

$$\overline{\sigma_{eN}} = \sigma_{Mott}(v_L G_L^{ee'} + v_T G_T^{ee'}). \tag{15}$$

The single-nucleon factors $G_K^{ee'}$ are taken from the relativistic Fermi gas model (RFG), and are defined in Eqs. (46,49,50) of Sect.III A.

The factor k_F (Fermi momentum) in Eq. (14) is introduced to remove the dependence on the particular nucleus, also motivated by the RFG model.

The *scaling variable* is a particular combination of q and ω (see Appendix A). In this work we use the scaling variable $\psi = \psi(q, \omega)$, defined in detail in Appendix A. Another common choice in the quasielastic domain is the y-scaling variable, the difference being that y is defined in terms of nucleon momentum (or missing momentum) and ψ is defined in terms of nucleon kinetic energy. Scaling is satisfied when $f(q, \omega) = f(\psi(q, \omega))$. This occurs for high enough values of the momentum transfer q, able to resolve the internal structure of the nucleus. Qualitatively this corresponds to the region $q \gtrsim 300\text{-}400$ MeV/c, where low energy collective effects (like giant resonances) become negligible.

The analysis of (e, e') experimental data performed in Refs. [18, 19, 22] shows that scaling is satisfied with good accuracy in the "scaling region" $\omega < \omega_{QEP}$, where ω_{QEP} corresponds to the maximum of the quasielastic peak. It is broken at higher energies loss, indicating that processes other than QE scattering, like pion production and excitation of two-particle two-hole (2p2h) states contribute to the cross section.

The above described q-independence of the scaling function f when expressed in terms of ψ is also called *scaling of first kind*, in order to distinguish it from *scaling of second kind*, concerning the dependence of the function f upon the specific nucleus. Scaling of the second kind means that $f(q, \omega)$ is the same for different nuclei for conveniently chosen values of the Fermi momentum k_F. The analysis of data on different nuclei (with mass number A ranging from 4 to 197) proves that scaling of the second kind is respected with very good accuracy in the scaling region.

Superscaling is the simultaneous occurrence of scaling of first and second kind. The function 14 is referred to as *superscaling function*.

The superscaling analysis of cross sections can be extended to the separate longitudinal and transverse responses. In this case two superscaling functions can be introduced by dividing the longitudinal and transverse response functions by the corresponding single-nucleon factor G_L, G_T

$$f_L(\psi) = k_F \frac{R_L(q, \omega)}{G_L^{e,e'}(q, \omega)}, \qquad f_T(\psi) = k_F \frac{R_T(q, \omega)}{G_T^{e,e'}(q, \omega)}. \qquad (16)$$

The analysis of the separated L and T responses shows that scaling violations mainly reside in the transverse response, whereas in the longitudinal response scaling works quite well in the full quasielastic region, *i.e.* also at $\omega > \omega_{QEP}$. The reason for this difference is that the main contributions which violate scaling, namely the 2p2h and Δ resonance excitations, are essentially transverse, with small longitudinal contamination of relativistic origin. From the analysis of the L/T separated (e, e') data a phenomenological longitudinal superscaling function has been extracted [23]. The agreement with this function represents a strong constrain for nuclear models used in neutrino-nucleus scattering simulations. This topic is examined in detail in subsequent sections.

Semi-inclusive electron-nucleus scattering

The study of $(e, e'N)$ reactions on nuclei provides essential information about nuclear structure and dynamics, not only on single-particle properties such as the spectral function and the nucleon's momentum distribution, but also on more complex mechanisms as nucleon-nucleon correlations and meson-exchange currents [1, 24, 25]. These are essential inputs for the simulation of ν-A scattering and therefore neutrino energy reconstruction.

The theoretical prediction of semi-inclusive reactions is a much harder task than modelling the inclusive process since the related observables are far more sensitive to the details of the dynamics. This allows one to better discriminate among different models.

In Plane Wave Impulse Approximation (PWIA) the 6-th differential $(e, e'N)$ cross section can be written as [26]

$$\frac{d^6\sigma}{dp_N d\Omega_N dk'_e d\Omega_e} = \frac{p_N m_N M_{A-1}}{\sqrt{(M_{A-1})^2 + p^2}} \sigma_{eN}(q, \omega; p, \mathcal{E}) S(p_m, E_m), \qquad (17)$$

where p_N, Ω_N, k'_e, Ω_e are the momenta and solid angles of the outgoing nucleon and electron, respectively, M_{A-1} is the ground state mass of the recoiling system, $\mathbf{p_m} = \mathbf{p}_{A-1} \equiv -\mathbf{p} = \mathbf{q} - \mathbf{p}_N$ is the missing momentum, $E_m = W_{A-1} + m_N - M_A$ is the missing energy, $\mathcal{E} = \sqrt{W_{A-1}^2 + p^2} - \sqrt{M_{A-1}^2 + p^2}$ is the excitation energy of the residual nucleus having invariant mass W_{A-1}, related to the missing energy E_m and to the separation energy $E_s = M_{A-1} + m_N - M_A$ by $\mathcal{E} \simeq E_m - E_s$. Finally, σ_{eN} is the half-off-shell single-nucleon cross section [27] and $S(p_m, E_m)$ the nuclear *spectral*

function, which yields the probability of removing a nucleon of momentum $p = p_m$ from the nuclear ground state leaving the residual system with excitation energy $\mathcal{E}$. The spectral function is related to the nucleon's momentum distribution

$$n(p) = \int_0^\infty S(p, \mathcal{E}) \, d\mathcal{E} \,. \tag{18}$$

The factorization (17) breaks if effects beyond the PWIA, as Final State Interactions (FSI) of the knocked-out nucleon with the residual nucleus and effects of two- or many-body currents, are taken into account. Moreover, even in the plane wave limit, the factorized expression (17) no longer holds if dynamical relativistic effects in the bound nucleons, arising from the lower components in the relativistic wave functions, are incorporated. As long as all these effects are properly taken into account in a Relativistic Distorted Wave Impulse Approximation (RDWIA) framework, which describes the distortion of the ejected proton wave function, the experimental data for $(e, e'p)$ can provide reliable information on the nuclear spectral function.

Several $(e, e'p)$ experiments were performed in the past in various laboratories (Saclay, NIKHEF, MIT/Bates, Mainz, JLab) at different kinematic conditions and on a variety of nuclei, from ^2H to ^{208}Pb. New data on ^{40}Ar have recently been taken at JLab [17] and will provide a valuable input for the analyses of neutrino experiments. The comparison of existing data with theoretical models points to a systematic overestimation of the data from shell model based calculations. This discrepancy is interpreted as a probe of the limitations of the mean field approach and of the importance of NN correlations in the nuclear wave function. It is often quantified in terms of *spectroscopic factors*, Z_α, which measure the actual occupancy (different from 1) of each shell (being α the set of quantum numbers characterizing a given orbital). The spectroscopic factors extracted from $(e, e'p)$ data are typically of the order of 0.5-0.7, depending on the orbital and on the nucleus. The knowledge of these factors and the understanding of their microscopic origin are important ingredients for the modelling of semi-inclusive reactions.

In the next sections we provide a systematic study of the models developed by our group comparing our predictions with inclusive as well as more exclusive reactions. In the latter, a much more challenging task, we will develop reliable models for the description of semi-inclusive (ν_l, lN) reactions, which require a more detailed knowledge of the nuclear structure and dynamics.

III. Models for QE in the Impulse Approximation

A. Relativistic Fermi Gas (RFG)

The quasielastic electroweak cross section is proportional to the hadronic tensor or response function for single-nucleon excitations transferring momentum $\mathbf{q}$ and energy ω [20]. The relativistic Fermi gas gives the simplest approach to a fully relativistic nuclear system whose response functions can be analytically computed, because the uncorrelated single-nucleon wave functions are free plane waves multiplied by Dirac spinors

$$\psi_{\mathbf{p},s}(\mathbf{r}) = \frac{1}{\sqrt{V}} e^{i\mathbf{p}\cdot\mathbf{r}} u_s(\mathbf{p}) \tag{19}$$

with single nucleon energy $E = (m_N^2 + \mathbf{p}^2)^{1/2}$. The positive energy spinor, $u_s(\mathbf{p})$, with mass m_N, is normalized to $\overline{u}u = 1$. In the ground state of the RFG all the momenta $\mathbf{p}$ with $p < k_F$ (the Fermi momentum) are filled in the Lab system. In the impulse approximation, the electroweak current is approximated by a one-body operator, which can produce only one-particle one-hole (1p1h) excitations. Therefore the hadronic tensor is given in this model by

$$W^{\mu\nu}(q, \omega) = \sum_{\mathbf{p}} \sum_{s,s'} \delta(E' - E - \omega) \frac{m_N^2}{EE'} J_{s's}^{\mu*}(\mathbf{p}', \mathbf{p}) J_{s's}^\nu(\mathbf{p}', \mathbf{p}) \theta(k_F - p) \theta(p' - k_F) \tag{20}$$

where J^μ is the electroweak current matrix element while $E = \sqrt{\mathbf{p}^2 + m_N^2}$ is the initial nucleon energy in the Fermi gas. The final momentum of the nucleon is $\mathbf{p}' = \mathbf{p} + \mathbf{q}$ and its energy is $E' = \sqrt{\mathbf{p}'^2 + m_N^2}$. Initial and final nucleons have spin component s and s', respectively.

In the thermodynamic limit we substitute the sums by momentum integrations. Then the volume $V = 3\pi^2 \mathcal{N}/k_F^3$ of the system is related to the Fermi momentum k_F and proportional to the number $\mathcal{N}$ of protons or neutrons participating in the process:

$$W^{\mu\nu}(q, \omega) = \frac{V}{(2\pi)^3} \int d^3p \, \delta(E' - E - \omega) \frac{m_N^2}{EE'} 2w_{s.n.}^{\mu\nu}(\mathbf{p}', \mathbf{p}) \theta(k_F - p) \theta(p' - k_F) \,, \tag{21}$$

where we have defined the single-nucleon tensor for the 1p1h excitation

$$w_{s.n.}^{\mu\nu}(\mathbf{p}',\mathbf{p}) = \frac{1}{2}\sum_{ss'} J_{s's}^{\mu*}(\mathbf{p}',\mathbf{p})J_{s's}^{\nu}(\mathbf{p}',\mathbf{p}). \tag{22}$$

In the case of electron scattering the electromagnetic current matrix element is given by

$$J_{s's}^{\mu}(\mathbf{p}',\mathbf{p}) = \overline{u}_{s'}(\mathbf{p}')\left[F_1(Q^2)\gamma^\mu + F_2(Q^2)i\sigma^{\mu\nu}\frac{Q_\nu}{2m_N}\right]u_s(\mathbf{p}), \tag{23}$$

where F_1 and F_2 are, respectively, the Dirac and Pauli electromagnetic form factors of proton or neutron.

In the case of neutrino or antineutrino CC scattering the weak current matrix element is the sum of vector and axial-vector terms $J^\mu = V^\mu - A^\mu$, where the vector current is

$$V_{s's}^{\mu}(\mathbf{p}',\mathbf{p}) = \overline{u}_{s'}(\mathbf{p}')\left[2F_1^V\gamma^\mu + 2F_2^V i\sigma^{\mu\nu}\frac{Q_\nu}{2m_N}\right]u_s(\mathbf{p}) \tag{24}$$

being $F_i^V = (F_i^P - F_i^N)/2$ the isovector form factors of the nucleon. The axial current is

$$A_{s's}^{\mu}(\mathbf{p}',\mathbf{p}) = \overline{u}_{s'}(\mathbf{p}')\left[G_A\gamma^\mu\gamma_5 + G_P\frac{Q^\mu}{2m_N}\gamma_5\right]u_s(\mathbf{p}), \tag{25}$$

where G_A is the nucleon axial-vector form factor and G_P is the pseudo-scalar axial form factor. It is usual to assume the dipole parametrization of the axial form factor, with the axial mass $M_A = 1.032$ GeV. From partial conservation of the axial current (PCAC) and pion-pole dominance, G_P and G_A are related by

$$G_P = \frac{4m_N^2}{m_\pi^2 + |Q^2|}G_A, \tag{26}$$

where $Q^2 = \omega^2 - q^2 < 0$.

The single nucleon tensor for the electroweak current is computed by performing the traces in Appendix B. To obtain the quasielastic cross section for (e,e') reaction we use the standard expansion in terms of response functions

$$\frac{d\sigma}{d\Omega' d\epsilon'} = \sigma_{\text{Mott}}\left(v_L R_L^{e.m.} + v_T R_T^{e.m.}\right) \tag{27}$$

where σ_{Mott} is the Mott cross section, $v_L = Q^4/q^4$ and $v_T = \tan^2(\theta/2) - Q^2/2q^2$, with θ the scattering angle. The electromagnetic longitudinal and transverse response functions are the following components of the e.m. hadronic tensor in the scattering coordinate system with the z-axis in the $\mathbf{q}$ direction (longitudinal)

$$R_L^{e.m.}(q,\omega) = W_{e.m.}^{00} \tag{28}$$
$$R_T^{e.m.}(q,\omega) = W_{e.m.}^{11} + W_{e.m.}^{22}. \tag{29}$$

Analogously the (ν_l, l^-) charged-current quasielastic (CCQE) cross section for neutrino energy $E_\nu = \epsilon$ and final lepton energy $\epsilon' = E_l$, has been expanded in terms of five response functions. If the lepton scattering angle is θ_l, the double-differential cross section can be written as [21, 28]

$$\frac{d^2\sigma}{dE_l d\cos\theta_l} = \sigma_0\left\{V_{CC}R_{CC} + 2V_{CL}R_{CL} + V_{LL}R_{LL} + V_T R_T \pm 2V_{T'}R_{T'}\right\}, \tag{30}$$

where we have defined the cross section

$$\sigma_0 = \frac{G^2\cos^2\theta_c}{4\pi}\frac{k'}{\epsilon}v_0. \tag{31}$$

In (31) the Fermi weak constant is $G = 1.166 \times 10^{-11}$ MeV^{-2}, the Cabibbo angle is $\cos\theta_c = 0.975$, k' is the final lepton momentum, and we have defined the factor $v_0 = (\epsilon + \epsilon')^2 - q^2$. Note that the fifth response function $R_{T'}$ is added $(+)$ for neutrinos and subtracted $(-)$ for antineutrinos. The lepton V_K coefficients depend only on the lepton

kinematics and they are defined by

$$V_{CC} = 1 - \delta^2 \frac{|Q^2|}{v_0} \tag{32}$$

$$V_{CL} = \frac{\omega}{q} + \frac{\delta^2}{\rho'} \frac{|Q^2|}{v_0} \tag{33}$$

$$V_{LL} = \frac{\omega^2}{q^2} + \left(1 + \frac{2\omega}{q\rho'} + \rho\delta^2\right)\delta^2 \frac{|Q^2|}{v_0} \tag{34}$$

$$V_T = \frac{|Q^2|}{v_0} + \frac{\rho}{2} - \frac{\delta^2}{\rho'}\left(\frac{\omega}{q} + \frac{1}{2}\rho\rho'\delta^2\right)\frac{|Q^2|}{v_0} \tag{35}$$

$$V_{T'} = \frac{1}{\rho'}\left(1 - \frac{\omega\rho'}{q}\delta^2\right)\frac{|Q^2|}{v_0}. \tag{36}$$

Here we have defined the dimensionless factors $\delta = m_l/\sqrt{|Q^2|}$, proportional to the charged lepton mass m_l, $\rho = |Q^2|/q^2$, and $\rho' = q/(\epsilon + \epsilon')$.

The five nuclear response functions R_K, $K = CC, CL, LL, T, T'$ (C=Coulomb, L=longitudinal, T=transverse) in the same scattering coordinate system as for electrons are then given by the following components of the hadronic tensor:

$$R_{CC} = W^{00} \tag{37}$$

$$R_{CL} = -\frac{1}{2}(W^{03} + W^{30}) \tag{38}$$

$$R_{LL} = W^{33} \tag{39}$$

$$R_T = W^{11} + W^{22} \tag{40}$$

$$R_{T'} = -\frac{i}{2}(W^{12} - W^{21}). \tag{41}$$

It is convenient to introduce dimensionless variables measuring the energy and momentum in units of m_N, namely $\lambda = \omega/2m_N$, $\kappa = q/2m_N$, $\tau = \kappa^2 - \lambda^2$, $\eta_F = k_F/m_N$, and $\xi_F = \sqrt{1 + \eta_F^2} - 1$.

In Appendix C we calculate analytically the response functions of the RFG by integrating Eq. (21) for the different components of the single nucleon tensor computed in Appendix B. The RFG responses are given as an universal function, called superscaling function, times a response that depends mainly on the nucleon-boson vertex, although it also incorporates some "minor" contributions linked to the Fermi momentum. To make simpler the discussion that follows we simply denote this as "single-nucleon" response (see Appendix C and equations below for details). The superscaling function in the RFG model is given by

$$f(\psi) = \frac{3}{4}(1 - \psi^2)\theta(1 - \psi^2). \tag{42}$$

As shown in Appendix C, the scaling variable, $\psi \equiv \psi(q, \omega)$, is a specific combination of the two variables q and ω (or, equivalently, κ, λ and τ) related to the minimum energy ε_0 allowed for the initial nucleon to absorb the momentum and energy transfer (q, ω). This is given by

$$\varepsilon_0 = \text{Max}\left\{\kappa\sqrt{1 + \frac{1}{\tau}} - \lambda, \varepsilon_F - 2\lambda\right\}, \tag{43}$$

where $\varepsilon_F = \sqrt{1 + \eta_F^2}$ is the Fermi energy in units of m_N. The scaling variable is defined by

$$\psi \equiv \psi(\lambda, \tau) = \sqrt{\frac{\varepsilon_0 - 1}{\varepsilon_F - 1}}\text{sgn}(\lambda - \tau). \tag{44}$$

Note that $\psi < 0$ for $\lambda < \tau$ (on the left side of the quasielastic peak). The meaning of ψ^2 is the following: it is the minimum kinetic energy of the initial nucleon divided by the kinetic Fermi energy.

Using this definition, the electromagnetic responses can be written as

$$R_K^{e.m.}(\lambda, \tau) = \frac{1}{k_F}G_K^{ee'}(\lambda, \tau)f(\psi(\lambda, \tau)), \tag{45}$$

$$G_K^{ee'}(\lambda, \tau) = \frac{\xi_F}{\eta_F^2\kappa}(ZU_K^p(\lambda, \tau) + NU_K^n(\lambda, \tau)), \tag{46}$$

where Z (N) is the proton (neutron) number. Analogously, for the weak responses

$$R_K(\lambda, \tau) = \frac{1}{k_F} G_K(\lambda, \tau) f(\psi) \tag{47}$$

$$G_K(\lambda, \tau) = \frac{\xi_F}{\eta_F^2 \kappa} \mathcal{N} U_K(\lambda, \tau), \tag{48}$$

where $\mathcal{N} = N$ (Z) for neutrino (antineutrino) scattering. The explicit expressions for the functions G_K (likewise U_K) are given below. This factorization of the scaling function inspires the superscaling models discussed in Sect. III E using a phenomenological scaling function instead of the universal superscaling function of the RFG.

The remaining quantities are the integrated single nucleon response functions. The electromagnetic ones, for protons or neutrons, are given by

$$U_L^{p,n}(\lambda, \tau) = \frac{\kappa^2}{\tau} \left[(G_E^{p,n}(\tau))^2 + \frac{(G_E^{p,n}(\tau))^2 + \tau(G_M^{p,n}(\tau))^2}{1 + \tau} \Delta(\lambda, \tau) \right] \tag{49}$$

$$U_T^{p,n}(\lambda, \tau) = 2\tau(G_M^{p,n}(\tau))^2 + \frac{(G_E^{p,n}(\tau))^2 + \tau(G_M^{p,n}(\tau))^2}{1 + \tau} \Delta(\lambda, \tau), \tag{50}$$

where the quantity Δ has been introduced

$$\Delta(\lambda, \tau) = \frac{\tau}{\kappa^2} \left[-\frac{(\lambda - \tau)^2}{\tau} + \xi_F[(1 + \lambda)(1 + \psi^2) + \frac{\xi_F}{3}(1 + \psi^2 + \psi^4)] \right]. \tag{51}$$

In what follows we present the explicit expressions for the weak integrated single-nucleon responses.

The U_{CC} is the sum of vector and axial contributions. The vector part implements the conservation of the vector current (CVC). The axial part can be written as the sum of conserved (c.) plus non conserved (n.c.) parts. Then (the arguments of each function are omitted for brevity)

$$U_{CC} = U_{CC}^{VV} + \left(U_{CC}^{AA}\right)_{\text{c.}} + \left(U_{CC}^{AA}\right)_{\text{n.c.}}. \tag{52}$$

For the vector CC response we have

$$U_{CC}^{VV} = \frac{\kappa^2}{\tau} \left[(2G_E^V)^2 + \frac{(2G_E^V)^2 + \tau(2G_M^V)^2}{1 + \tau} \Delta \right], \tag{53}$$

where G_E^V and G_M^V are the isovector electric and magnetic nucleon form factors

$$G_E^V = F_1^V - \tau F_2^V \tag{54}$$
$$G_M^V = F_1^V + F_2^V. \tag{55}$$

The axial-vector CC responses are

$$\left(U_{CC}^{AA}\right)_{\text{c.}} = \frac{\kappa^2}{\tau} G_A^2 \Delta \tag{56}$$

$$\left(U_{CC}^{AA}\right)_{\text{n.c.}} = \frac{\lambda^2}{\tau} (G_A - \tau G_P)^2. \tag{57}$$

Using current conservation for the conserved part of the integrated single-nucleon responses $K = CL, LL$ we can express them as

$$U_{CL} = -\frac{\lambda}{\kappa} \left[U_{CC}^{VV} + \left(U_{CC}^{AA}\right)_{\text{c.}} \right] + \left(U_{CL}^{AA}\right)_{\text{n.c.}} \tag{58}$$

$$U_{LL} = \frac{\lambda^2}{\kappa^2} \left[U_{CC}^{VV} + \left(U_{CC}^{AA}\right)_{\text{c.}} \right] + \left(U_{LL}^{AA}\right)_{\text{n.c.}}, \tag{59}$$

where the n.c. parts are

$$\left(U_{CL}^{AA}\right)_{\text{n.c.}} = -\frac{\lambda\kappa}{\tau} (G_A - \tau G_P)^2 \tag{60}$$

$$\left(U_{LL}^{AA}\right)_{\text{n.c.}} = \frac{\kappa^2}{\tau} (G_A - \tau G_P)^2. \tag{61}$$

Finally, the transverse responses are given by

$$U_T = U_T^{VV} + U_T^{AA} \tag{62}$$

$$U_T^{VV} = 2\tau(2G_M^V)^2 + \frac{(2G_E^V)^2 + \tau(2G_M^V)^2}{1+\tau}\Delta \tag{63}$$

$$U_T^{AA} = G_A^2\left[2(1+\tau) + \Delta\right] \tag{64}$$

$$U_{T'} = 2G_A(2G_M^V)\sqrt{\tau(1+\tau)}[1 + \widetilde{\Delta}] \tag{65}$$

with

$$\widetilde{\Delta} = \frac{1}{\sqrt{\tau(1+\tau)}}\left[\frac{\tau}{\kappa}(1+\lambda) - \sqrt{\tau(\tau+1)} + \frac{\tau}{\kappa}\frac{1}{2}\xi_F(1+\psi^2)\right]. \tag{66}$$

For completeness we show in Fig. 1 the comparison of the experimental superscaling function extracted from the analysis of the separate longitudinal response data (denoted as SuSA) with the relativistic Fermi gas prediction. The variable ψ' differs from ψ by an energy shift related to the nucleon separation energy (see Appendix A for details). Note the striking difference between the RFG result and the experimental data: the RFG predicts a symmetric function around $\psi' = 0$, with a maximum value of 0.75 and restricted to the region $[-1, 1]$ (see Eq. (42)), while the data display a pronounced asymmetric tail at large ψ' (large ω) and a maximum of ~0.6.
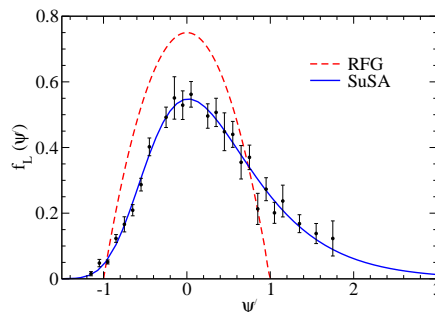

FIG. 1. The experimental longitudinal scaling function displayed versus the scaling variable ψ' and compared to the RFG prediction (red dashed curve). The solid blue curve is a fit of the data [23].

B. Semi-relativistic shell models

Nuclear models based on the Fermi gas describe the single nucleon wave functions as plane waves, thus neglecting the finite size of the nucleus, assuming that the response per particle is the same as for infinite nuclear matter. The validity of this assumption has been investigated theoretically in the nuclear shell model (SM) for the kinematics of interest [28–32]. The Fermi gas cannot describe the very low ω region of the nuclear response, dominated by excitation of discrete states and giant resonances. Besides, Pauli blocking, for small momentum transfer $q < 2k_F$, forbids emission from a subset of occupied momentum states in the Fermi gas, even if there is enough energy transfer, by momentum conservation. In a real nucleus, however, the nucleons are not plane waves. This makes the RFG inappropriate to precise modelling of the nuclear response at low momentum transfer $q < 500$ MeV/c [29].

In Ref. [29] the finite size effects on the electromagnetic QE response functions were studied using a continuum shell model (CSM) in the non relativistic regime for $q \le 550$ MeV/c. In the CSM the single nucleon wave functions were obtained by solving the Schrödinger equation with a mean field potential $V(\mathbf{r})$ of Woods-Saxon type, including central and spin orbit interactions, plus a Coulomb part for protons

$$V(\mathbf{r}) = \frac{-V_0}{1 + e^{(r-R)/a}} + \frac{1}{m_\pi^2}\frac{1}{r}\frac{d}{dr}\left(\frac{-V_{ls}}{1 + e^{(r-R)/a}}\right)\mathbf{l}\cdot\boldsymbol{\sigma} + V_{\text{Coul}}(r). \tag{67}$$

This potential is solved numerically for bound and continuum nucleon states, and the parameters V_0, V_{ls}, R, a are fitted to the experimental energies of the valence shells for protons and neutrons, obtained from the masses of the neighboring nuclei. The SM is the simplest model where the response of a confined quantum system of nucleons
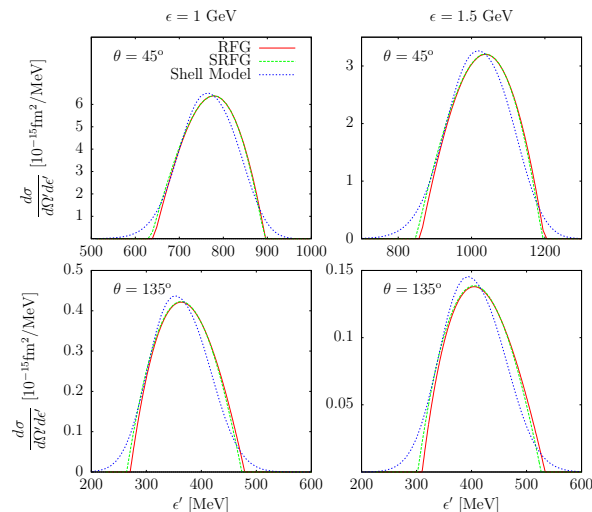
FIG. 2. Differential cross section of the reaction ^{12}C(ν_μ, μ^-) for incident neutrino energies $\epsilon = 1$ and 1.5 GeV and for two scattering angles: RFG with $k_F = 215$ MeV/c. SRFG and shell model from [28].

can be evaluated, and thus, it allows us to explore the importance of finite size against the infinite Fermi Gas (FG) model. This study was made theoretically by comparing the separate longitudinal and transverse response functions. While the FG model reproduces the position and width of the separate SM responses, it cannot fully account for the detailed energy dependence. Specifically, the SM responses present tails in the low and high ends of the energy transfer, reminiscent of the momentum distribution of a finite system.

In Ref. [30] the shell model was extended to a semi-relativistic (SR) shell model by implementing relativistic kinematics and using a semi-relativistic expansion of the electromagnetic current. The relativistic electroweak current was expanded in powers of the initial nucleon momentum, while treating exactly the relativistic kinematics of the final ejected particle. The SR expansion of the current and relativistic kinematics was tested in the Fermi gas model by comparison of the RFG and semi relativistic Fermi gas (SRFG) response functions. The two models are in great accord for all values of the momentum transfer. This is seen in Fig. 2, where results for the semi relativistic shell model (SRSM) are compared to the RFG and the SRFG models for the reaction ^{12}C(ν_μ, μ^-) [28]. The RFG and SRFG results are essentially equal, while the SRSM also gives similar results, with the exception of the characteristic finite size tails and a small shift of the maximum.

The semi-relativistic shell model was extended in [31] to improve the description of the final-state interaction of relativistic nucleons by performing a Schrödinger reduction of the Dirac equation with scalar and vector potentials, taken from the relativistic mean field (RMF) model [33]. The longitudinal scaling function computed with the SR shell model with Dirac Equation Based (DEB) potentials was shown to be very similar to the experimental data, with the appropriate asymmetry and long tail for large ω. This suggests that relativistic dynamics take into account the effects necessary to describe QE lepton scattering. In this respect the RMF of the next section is a clear candidate to achieve this goal.

C. Relativistic Mean Field (RMF)

The high energy and momentum transfer involved in electroweak reactions require a fully relativistic formalism, not only for the kinematics but also for the nuclear dynamics. This was the basic motivation to introduce the Relativistic Mean Field (RMF) approach to describe electron and neutrino scattering with nuclei. In this section we summarize the formalism of RMF approach [33–40], and show its capability to describe inclusive and semi-inclusive reactions. The RMF model is described here within the framework of the Impulse Approximation (IA), where the scattering is described as an incoherent sum of single-nucleon scattering reactions. Although this is an oversimplified description of the real process, it accounts for the main effects for quasielastic (QE) kinematics. Ingredients beyond the IA, such as nucleon correlations, meson exchange currents (MEC), etc., should be taken into account for a proper description of the data. This topic is discussed in subsequent sections.

The analysis of the QE data for (e, e') shows that scaling is fulfilled at high level. Thus any theoretical model aiming at explaining electron scattering is constrained to satisfy scaling, and to describe the particular shape of the
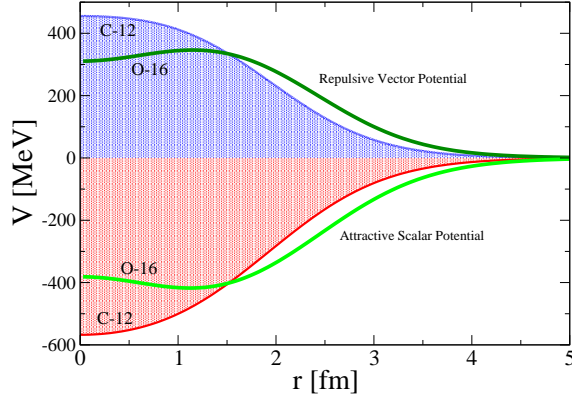
FIG. 3. Relativistic attractive scalar and repulsive vector potentials corresponding to ^{12}C and ^{16}O.

experimental scaling function with a long tail extended to high values of the energy transfer (high positive values of the scaling variable). Most of the models based on the IA satisfy scaling; this is the case of the RFG, the semirelativistic approach presented in the previous section, and non relativistic spectral function approaches. However, most of them lead to symmetrical scaling functions that depart significantly from the data analysis, without the high energy tail.

On the contrary, the RMF model leads to an asymmetrical superscaling function in accordance with data. This proves the capability of the RMF model to describe inclusive electron scattering reactions and its extension to neutrino processes. Not only that, the model has been also applied to semi-inclusive $(e, e'p)$ reactions providing a good description of the reduced cross section (distorted momentum distribution), as well as the spectroscopic factors. Within the general framework of $(e, e'p)$ processes, the reduced cross section is defined as the semi-inclusive differential cross section divided by the single-nucleon cross section evaluated using different options for the nucleon current operators and gauges [24, 25, 39–42].

The single-nucleon current matrix element entering in the electromagnetic and weak tensors is

$$\langle J^\mu(Q) \rangle = \int d\mathbf{r} e^{i\mathbf{q} \cdot \mathbf{r}} \overline{\psi}_F(\mathbf{p}_F, \mathbf{r}) \hat{\Gamma}^\mu \psi_B^{jm}(\mathbf{r}) \tag{68}$$

with $\hat{\Gamma}^\mu$ the corresponding single-nucleon current operator for electron or weak neutrino scattering, and Ψ_B^{jm} ($\Psi_F(\mathbf{p}_F, \mathbf{r})$) the wave function for the initial bound (emitted) nucleon. The RMF model incorporates a fully relativistic description of the scattering reaction based on the impulse approximation. We use the relativistic free nucleon expressions for the current operators corresponding to the usual options, denoted as CC1 and CC2,

$$\hat{\Gamma}_{CC1}^\mu = (F_1 + F_2)\gamma^\mu - \frac{F_2}{2m_N}(\overline{P} + P_F)^\mu \tag{69}$$

$$\hat{\Gamma}_{CC2}^\mu = F_1 \gamma^\mu + \frac{iF_2}{2m_N}\sigma^{\mu\nu}Q_\nu \, , \tag{70}$$

where F_1 and F_2 are the Pauli and Dirac nucleon form factors, respectively, that depend only on Q^2. We have introduced the on-shell four-momentum $\overline{P}^\mu = (\overline{E}, \mathbf{p})$ with $\overline{E} = \sqrt{p^2 + m_N^2}$ and $\mathbf{p}$ the bound nucleon momentum. These two operators are equivalent for on-shell nucleons, as occurs in the RFG model. However, bound and ejected nucleons are off-shell, and hence the $CC1$ and $CC2$ operators lead to different results. Moreover, the current is not strictly conserved and uncertainties linked to the election of the gauge also occur [35, 42]. In the case of neutrino scattering processes the current operator also includes the axial term,

$$\hat{\Gamma}_A^\mu = \left[G_A \gamma^\mu + \frac{G_P}{2m_N} Q^\mu \right] \gamma^5 \tag{71}$$

with G_A and G_P the axial-vector and pseudoscalar nucleon form factors, respectively.

Concerning the nucleon wave functions, they are given as solutions of the Dirac equation in presence of phenomenological relativistic potentials with scalar and vector terms. We describe the bound nucleon states, ψ_B^{jm}, as self-consistent Dirac-Hartree solutions, using a Lagrangian with local potentials fitted to saturation properties of nuclear matter, radii and nuclear masses. In Fig. 3 we show the potentials of ^{12}C and ^{16}O. As shown, large scalar (attractive) and vector (repulsive) potentials, that do not depend on the energy, are present. It is important to point out that the RMF does get saturation, even with no Fock terms neither explicit nucleon correlations included. This
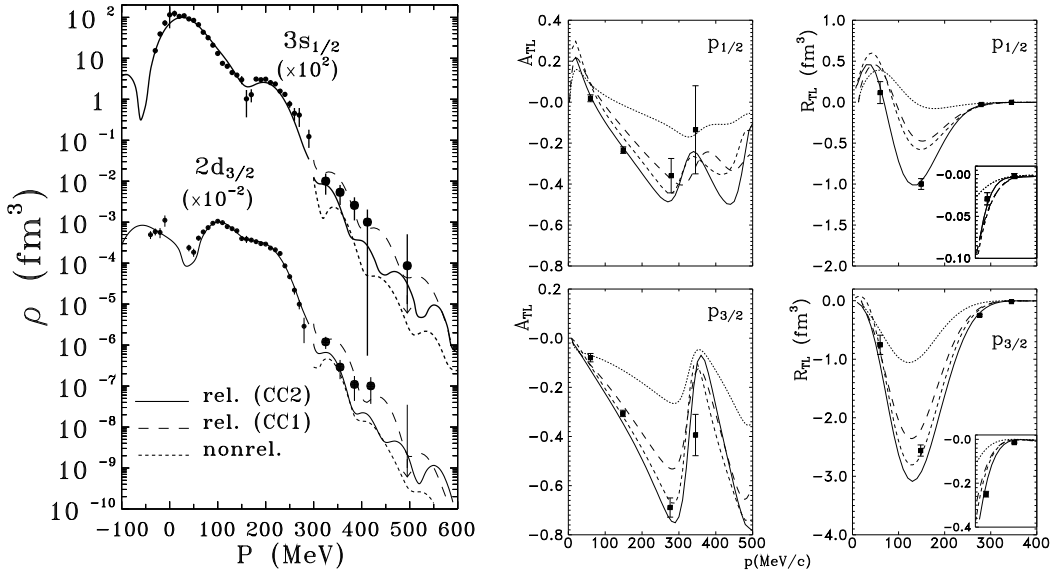
FIG. 4. (Left panel) Reduced cross sections versus missing momentum for the shells $3s_{1/2}$ and $2d_{5/2}$ of ^{208}Pb. Small circles with error bars are data from Ref. [43]. In the high missing momentum region the relativistic results obtained with the currents CC2 (solid line) and CC1 (long-dashed lines), as well as the nonrelativistic results (short-dashed lines) are compared with data from Ref. [44]. Figure taken from Ref. [39]. (Middle and right panels) Interference longitudinal-transverse response R_{TL} and TL asymmetry A_{TL} for proton knockout from ^{16}O for the $1p_{1/2}$ (top panels) and $1p_{3/2}$ (bottom panels) orbits. Results correspond to a fully relativistic calculation using the Coulomb gauge and the current operator CC2 (solid line), a calculation performed by projecting the bound and scattered proton wave functions over positive-energy states (short-dashed line) and two nonrelativistic calculations with (long-dashed) and without (dotted) the spin-orbit correction term in the charge density operator.

comes from the combination of the strong scalar and vector potentials that incorporate repulsive and attractive interactions, and it makes a big difference with most non-relativistic approaches where correlations are needed in order to get saturation.

In the exclusive $(e, e'p)$ reactions, the final-state interaction (FSI) of the ejected nucleon is described using phenomenological energy-dependent complex optical potentials fitted to elastic proton-nucleus scattering. The imaginary part of the potential produces absorption, namely, flux lost into the unobserved non-exclusive channels. The RMF model with complex optical potentials yields very good agreement with $(e, e'p)$ data. Not only reasonable values for the spectroscopic factors are given [36, 40] but also the cross section describes the data even at high values of the missing momentum [39]. It should be emphasized that the high p region is very sensitive to theoretical models, and in particular, to the strong enhancement of the lower components in the Dirac wave functions produced by the relativistic potentials mainly in the final scattering state. The remarkable agreement between the RMF predictions and data for the reduced cross sections (divided by the single nucleon cross section) and, particularly, for the interference longitudinal-transverse response and TL asymmetry, is a clear signal of dynamical relativistic effects [41] (see Fig. 4).

The extension of the RMF approach to inclusive processes such as (e, e') and (ν_ℓ, ℓ) requires to retain the contributions from the inelastic channels. One approach is to use the real part of the optical potential (rROP). However orthogonalization is violated as bound and ejected nucleon states are evaluated using different potentials. The same happens in a second approach in which FSI are turned off, known as the relativistic plane wave impulse approximation (RPWIA). A third approach consists of describing the scattered states as solutions of the Dirac equation with the same real energy-independent RMF potential considered for the initial bound nucleon states. This RMF model (same potential for bound and scattered nucleons) preserves orthogonality, verifies current conservation, and fulfills the dispersion relations.

In Fig. 5 we compare the three models of FSI, RPWIA, rROP and RMF models, for inclusive (e, e'). Results are presented for the two current operators, CC1 and CC2. Only the RMF model leads to a significant tail extended to large values of ω. This points to the capability of the RMF model to describe successfully inclusive electron scattering data in the QE domain. Not only superscaling emerges from the calculations, as illustrated below, but also the specific shape of the scaling function with a long tail extended to high ω.

To show how scaling of the first kind works, in Fig. 6 we compare the longitudinal scaling function evaluated with
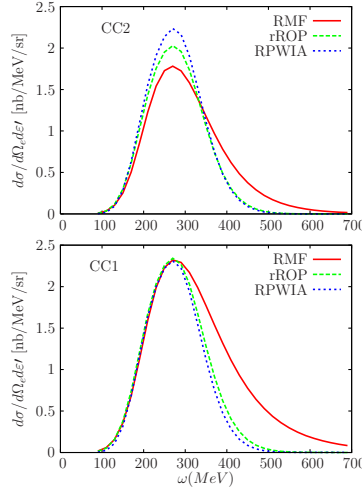
FIG. 5. Double differential cross section for (e, e') scattering on ^{12}C. Results correspond to the electron beam energy fixed to 1 GeV and scattering angle $\theta = 45^o$. Top (bottom) panel refers to results obtained with the CC2 (CC1) current operators. Coulomb gauge has been considered.
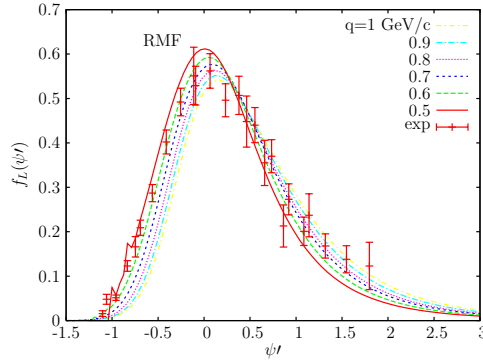

FIG. 6. Longitudinal scaling function for ^{12}C(e, e') evaluated in the RMF model for several values of the momentum transfer. Experimental data from Ref. [19].

the RMF approach for different values of q. A comparison with data is also provided. Notice the shift in the RMF results to larger positive ψ-values as the momentum transfer gets higher. In spite of its merits, the strong energy-independent scalar and vector potentials involved in RMF lead to a very significant shift of the scaling functions to higher ω, and correspondingly, too severe a decrease in the maxima.

In Fig. 7 (top panels) we analyze the off-shell effects in the global RMF scaling function (including the contribution of both the longitudinal and transverse channels). We consider the two current operators, CC1 and CC2, and show results for three different gauges: Coulomb, Lorentz and Weyl [35, 42, 47–49]. As observed, the CC2 current leads to very similar results in the three gauges whereas the Weyl prediction for the CC1 operator deviates very significantly from the others. This gives us confidence in the use of the CC2 current. The bottom panels of Fig. 7 show the scaling function for ^{12}C, ^{16}O and ^{40}Ca for the two current operators. As observed, scaling of second kind, i.e., independence of the scaling function on the nucleus, is highly satisfied in the case of the CC2, while some discrepancies, mainly connected with ^{40}Ca, are present with the CC1 current. Again, this reinforces our confidence in the use of the CC2 current operator.

The capability of the RMF model to provide a successful description of the world QE (e, e') data constitutes a benchmark in its extension to the study of neutrino-nucleus reactions [31–33, 35, 46, 50–52]. To show some illustrative results, the differential cross sections for CCQE neutrino scattering ^{12}C(ν_μ, μ^-) is compared in Fig. 8 for different models. The energy of the neutrino beam has been fixed to $\varepsilon_\nu = 1$ GeV and the muon scattering angle to $\theta_\mu = 45^o$. We
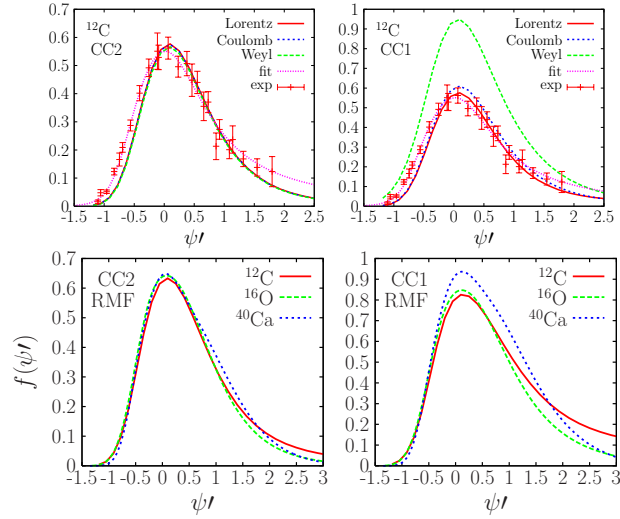
FIG. 7. Global scaling function corresponding to (e, e') evaluated with the RMF model. Results are presented for the two current operators: CC2 (left panels) and CC1 (right panels). Off-shell effects are shown in the top panels where results are presented for ^{12}C and three gauges: Lorentz, Coulomb and Weyl. Bottom panels refer to the analysis of second kind scaling comparing the results obtained for carbon, oxygen and calcium.
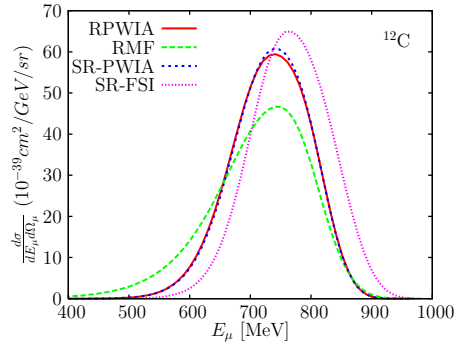

FIG. 8. Double differential cross section for charged-current neutrino scattering on ^{12}C. Results correspond to fixed values of the neutrino energy and muon scattering angle: $\varepsilon_\nu = 1$ GeV and $\theta_\mu = 45^o$. Predictions of the RMF and RPWIA are compared with the results of a semirelativistic calculation (see text and Ref. [28] for details).

compare the RPWIA and RMF predictions with the semi-relativistic model of [28] with and without a WS potential (see previous section). The similarity between the RPWIA and SR-PWIA results shows that, within the plane wave approximation for the final state, the particular description of the initial bound states as well as the current operator (relativistic versus nonrelativistic) leads to almost identical cross sections. On the contrary, the effects ascribed to final state interactions, RMF versus SR-FSI (with WS potential), produce cross sections that differ significantly. Not only the strength in the maximum is very different, but also the shape of the cross section with the long tail at smaller values of the final muon energy being present in the RMF case.

In Fig. 9 we present the neutrino scaling functions obtained by dividing the (ν_μ, μ^-) cross section by the weak single-nucleon cross sections [53],

$$f^\nu(\psi) = \frac{k_F}{\overline{\sigma_{\nu l}^{s.n.}}} \frac{d^2\sigma}{dE_l d\cos\theta_l} \tag{72}$$

$$\overline{\sigma_{\nu l}^{s.n.}} = \sigma_0 \left\{ V_{CC}G_{CC} + 2V_{CL}G_{CL} + V_{LL}G_{LL} + V_T G_T \pm 2V_{T'}G_{T'} \right\}. \tag{73}$$

where σ_0 is given in Eq. (31), and the single nucleon factors G_K are defined in Eq. (48). In the panels on the left we study scaling of the first kind for the three models RPWIA, rROP and RMF. Panels on the right refer to scaling of second kind by showing the results for carbon, oxygen and calcium. As noticed, both kinds of scaling are fulfilled
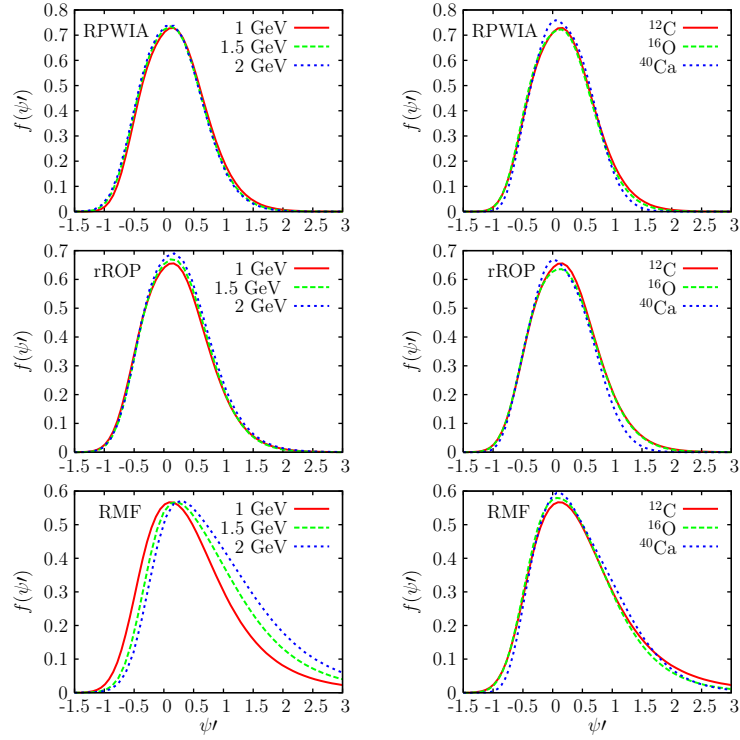
FIG. 9. Scaling function evaluated from (ν, μ^-) on ^{12}C. Results are shown for RPWIA (top panels), rROP (middle) and RMF (bottom). Scaling of the first kind is analyzed in the graphs on the left that compare results for different values of the energy beam. Scaling of the second kind is shown in the right panels that contain the scaling functions corresponding to ^{12}C, ^{16}O and ^{40}Ca.
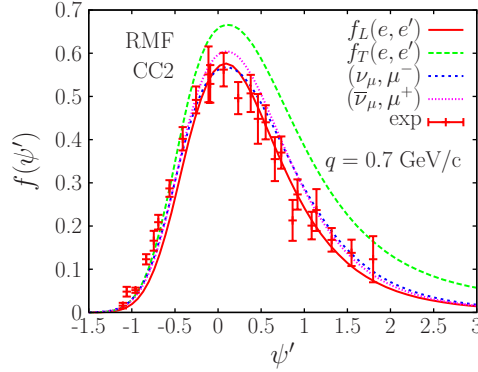

FIG. 10. (Color online) Longitudinal and transverse scaling functions for (e, e') compared with $f(\psi')$ evaluated from (ν, μ^-) and $(\overline{\nu}, \mu^+)$. All results correspond to the RMF approach using the CC2 current operator. The kinematics selected corresponds to fixed values of the incident lepton energy, $\varepsilon = 1$ GeV, and momentum transfer, $q = 0.7$ GeV/c. The averaged experimental function extracted from longitudinal electron scattering data is also shown [45]. Figure taken from Ref. [46].

at high level except for the first kind within the RMF model where a shift to higher values of the scaling variable is clearly observed as the energy of the neutrino beam increases. This was also the case for (e, e') reactions. Thus we conclude that, within the present models, scaling works at the same level of precision for electron and neutrino scattering reactions with nuclei.

In Fig. 10 we compare the scaling functions corresponding to the two processes. In the case of electron scattering we show separately the contributions ascribed to the two channels, longitudinal and transverse, and compare with the results for CC muon neutrinos (antineutrinos) processes. Notice that the scaling function for neutrinos (antineutrinos), even being basically transverse (the longitudinal channel is negligible), is more similar to the longitudinal (e, e') result
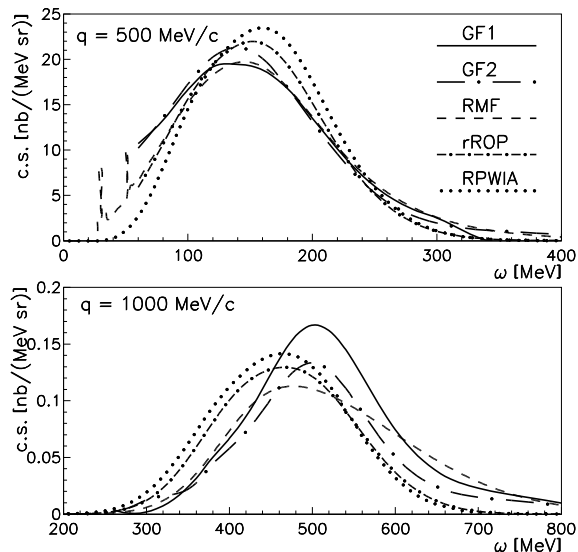
FIG. 11. Differential cross section of the ^{12}C(e, e') reaction at electron beam energy of 1 GeV. The GF predictions are compared with the RMF, rROP and RPWIA approaches. GF1 and GF2 refer to the RGF results obtained with EDAD1 and EDAD2 optical potentials. Figure taken from [54].

than to the transverse one. This is connected with the isoscalar/isovector contributions in electron scattering processes compared with the pure isovector character of CC neutrino reactions [46]. Moreover, the enhancement shown by the T contribution in (e, e') is a consequence of the role played by the lower components of the relativistic nucleon wave functions. This effect is in accordance with the analysis of the separate longitudinal/transverse data.

D.   Other models: RGF, SF, RPA, CRPA, GFMC

An alternative, relativistic approach to FSI in (e, e') and (ν_ℓ, ℓ) reactions is provided by the Relativistic Green Function (RGF) model. Here the description of the initial nucleon states is analogous to the RMF model presented in the previous section, but the scattered nucleon wave function is computed with Green's function techniques. The RGF method treats FSI consistently in the inclusive and exclusive channels by using a complex relativistic optical potential that describes elastic nucleon scattering. The flux reduction by the imaginary part of the optical potential is redistributed into the other channels, so the total flux is conserved in the inclusive process. The RGF has been applied to electron and neutrino-nucleus scattering in Refs. [50, 54–60]. As an example we present in Fig. 11 the inclusive ^{12}C(e, e') cross section for fixed momentum transfers and initial electron energy $\varepsilon = 1$ GeV. In each panel we compare the RGF predictions with two different optical potentials (GF1 and GF2), with the results of the RMF, rROP and RPWIA approaches. As seen in the figure, there are large differences between GF1 and GF2 cross sections depending on the kinematics and both results also deviate significantly from the other models. Particularly interesting is that the large asymmetry shown by the RMF prediction at $q = 1$ GeV/c is lost in the other approaches.

In the *spectral function* (SF) approach the inclusive scattering cross section is factorized as the product of the single-nucleon cross section and the nuclear spectral function that gives the probability of removing a nucleon with certain values of momentum and energy. Although factorization does not hold in general it works well in the QE regime. Contrary to the independent particle picture where the bound nucleon shells correspond to discrete energy eigenvalues, the formalism of the spectral function introduces dynamical correlations induced by nucleon-nucleon (NN) force. As a result, the spectral function acquires tails that extend to large energy and momentum. Note that the spectral function formalism is non-relativistic. This can introduce some doubts on its application to processes where the energy and momentum transfers can be very high.

The existence of final state interactions between the ejected nucleon and the residual nucleus has long been experimentally established. However, the factorization assumption, implicit in the spectral function formalism, is based on the Plane Wave Impulse Approximation (PWIA). Different approaches have been used in the past to incorporate FSI in the spectral function formalism. In most of the cases the cross section (response functions) is finally written in
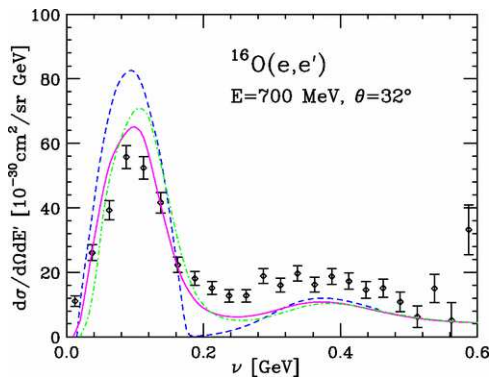
FIG. 12. Double differential cross section of the ^{16}O(e, e') reaction at electron beam energy 700 MeV and electron scattering angle 32°. The SF calculation including FSI (solid line) is compared with the IA (no FSI) calculation (dot-dashed line) and the Fermi Gas (FG) model with $k_F = 225$ MeV and a shift energy $\epsilon = 25$ MeV. Data from Ref. [61]. Figure taken from [62].
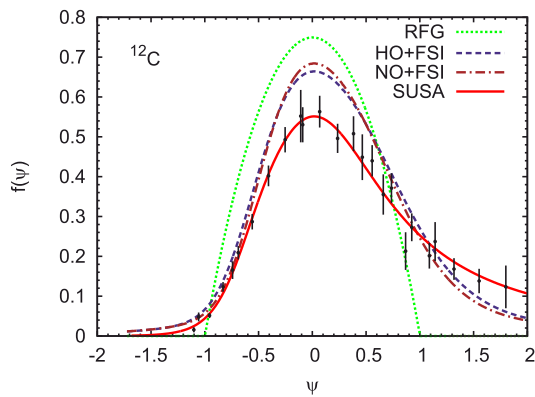

FIG. 13. Results for the superscaling function for ^{12}C obtained using harmonic oscillator (HO) and natural orbitals (NO) approaches with FSI (see text for details). Comparison with the RFG and Superscaling (SUSA) predictions, as well as with the longitudinal experimental data. Figure taken from [63].

terms of the impulse approximation (IA) cross section convoluted with a folding function that embodies FSI effects. A very detailed study on this topic can be found in [15, 62, 64–70]. We present in Fig.12 an illustrative example where it is clearly shown that FSI produce a shift and a redistribution of the strength leading to a quenching of the peak and to an enhancement of the tail.

In the studies presented in Refs. [63, 71, 72] the spectral function is constructed starting with the independent particle model and introducing a Lorentzian function to describe the energy dependence. FSI are incorporated through a time-independent optical potential [73, 74]. In Fig. 13 we present some illustrative results for the superscaling function evaluated from the double differential cross section. The bound nucleon wave functions are computed with the harmonic oscillator (HO) and natural orbitals (NO) models. These spectral function models also include FSI. As noticed, the role of FSI leads to a redistribution of the strength, with lower values of the scaling function at the maximum and an asymmetric shape around the peak position. The scaling properties of the SF approach have also been discussed in Ref. [75].

Other descriptions of the inclusive responses include the effects of random phase approximation (RPA) in the local Fermi Gas and Hartree-Fock (HF) models. In the former, RPA correlations are introduced through a Landau Migdal residual interaction with pion and rho exchange. This is the general strategy followed in a long series of works performed by Martini et al. and Nieves and collaborators [76, 77]. These calculations include contributions arising from many-particle, many-hole (np-nh) excitations. A fully relativistic model of meson exchange currents (MEC) in 2p2h contributions is discussed in sect. IV.

A shell-model approach to RPA correlations is developed by the Gent group. Bound and scattered nucleon wave functions are obtained with a self-consistent Hartree-Fock model using a Skyrme-type nucleon-nucleon interaction. The HF model is later extended with collective excitations described through a continuum random phase approximation
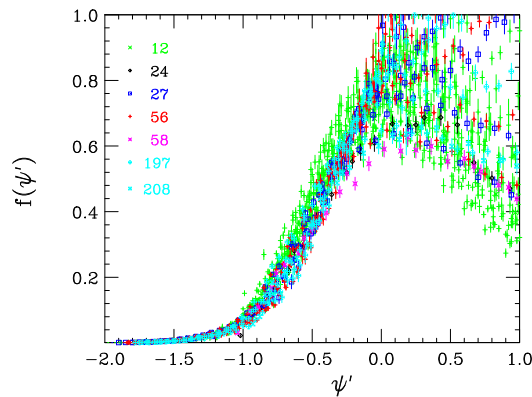
FIG. 14. Scaling function $f(\psi')$ as a function of ψ' for different nuclei ($A \geq 12$) and several kinematics covering from forward to very backward angles as well as from low to very high incident energies. The values of A corresponding to different symbols are shown in the figure. Data taken from [19].

(CRPA). Although inherently non-relativistic, the HF-CRPA model incorporates some relativistic corrections [78, 79], providing reliable results for the scattering observables from very low momentum transfers, where long-range correlations play an essential role, to moderate values of q [80–84].

Studies on the electromagnetic responses, as well as the extension to neutrino-nucleus scattering processes have also been performed with the Green's Function Monte Carlo (GFMC) model [66, 85–93]. This *ab initio* approach allows for a very accurate description of the dynamics of constituent nucleons in nuclei. In spite of some recent remarkable results concerning the electromagnetic responses in QE inclusive (e, e') reactions, the computational complexity of such an approach is currently limited to light nuclei (^{12}C). Not only the cost of calculation increases exponentially with the number of nucleons, but also the need to include relativistic kinematics and baryon resonance production involve non trivial difficulties.

E. Superscaling models: SuSA and SuSAv2

SuperScaling Approach: a semiphenomelogical model

In III A we have seen that in the RFG all the response functions of electron and neutrino scattering are proportional to the same scaling function of the RFG, Eqs. (45,48). This is in general not true in the real world as there are many mechanisms violating scaling. Starting with the experimental (e, e') cross section data one can compute the experimental superscaling function by dividing by the single nucleon cross section. In Fig. 14 data are plotted as a function of the shifted variable, ψ', defined with a shifted $\omega \to \omega - E_s$. As seen in the figure, scaling of the (e, e') cross section is approximately fulfilled in the region below the QE peak ($\psi' < 0$), with a narrow spread of data. The values of E_s and k_F were fitted to maximize scaling in this region. On the contrary, scaling is violated in the region above the QE peak, where contributions breaking factorization play an important role.

This is clarified by studying the experimental longitudinal and transverse response functions, that have been measured for several nuclei. The corresponding longitudinal, $f_L(\psi')$, and transverse, $f_T(\psi')$, experimental data, obtained dividing the responses by the single nucleon factors, Eq. (16), are shown in Fig. 15. We see that the longitudinal response approximately scales in the whole region of the QE peak, whereas the transverse data do not scale, being scaling violations more prominent in the region above the maximum of QE peak ($\psi' > 0$). Scaling violations at high ω are produced by meson production and resonance excitations, which are predominantly transverse. Also contributions beyond the impulse approximation such as two-particle two-hole excitations produced by MEC, come into play in the transverse channel (see Sect. IV).

In the SuperScaling Analysis (SuSA) one assumes that $f_L = f_T$ if one subtracts the contributions that violate scaling. This is usually known as scaling of the zeroth kind. Therefore the SuSA prescription is to identify the universal scaling function with the experimental longitudinal responses. This allows one to compute all the response functions, for both electron and neutrino scattering, by multiplying by the corresponding single nucleon factor of the RFG. The analysis of the longitudinal response functions data leads to the results already shown in Fig. 1 ,where the
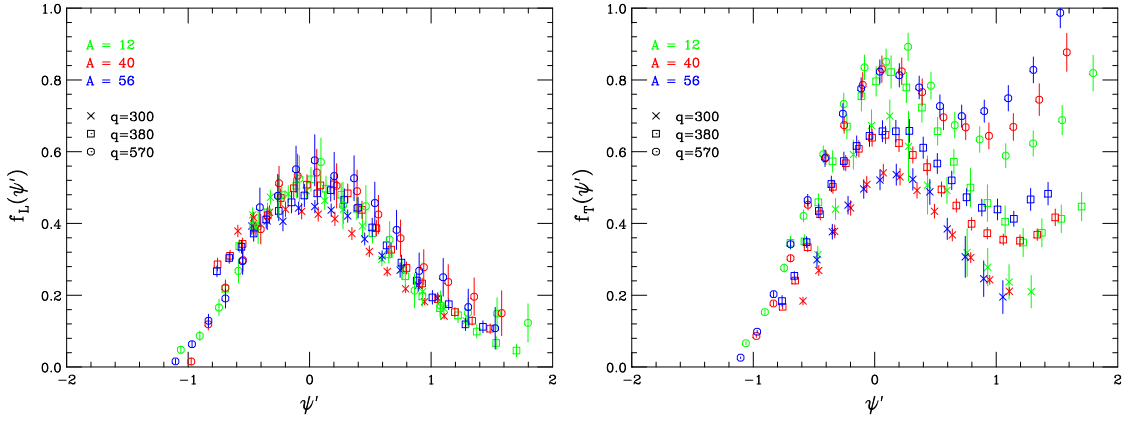
FIG. 15. Scaling function, $f_L(\psi')$ and $f_T(\psi')$, from the longitudinal and transverse response, respectively, as a function of ψ' for different nuclei ($A \geq 12$) and for different values of q (in MeV/c). Data taken from [23].

solid line corresponds to a fit of data given by the following parametrization of the SuSA scaling function

$$f_{SuSA}(\psi') \equiv f_L(\psi') = \frac{p_1}{[1 + p_2^2(\psi' - p_3)^2](1 + e^{p_4\psi'})} \tag{74}$$

with $p_1 = 2.9883$, $p_2 = 1.9438$, $p_3 = 0.67310$ and $p_4 = -3.8538$. As already shown in Fig. 1, the behavior of data leads to the striking difference between $f_{SuSA}(\psi')$ and the prediction provided by RFG, the former with a pronounced asymmetrical tail extended towards positive values of ψ', $i.e.$, $\omega > \omega_{QEP}$, and a maximum value $f_{SuSA}(0) \sim 0.6$. This behavior sets a strong constraint to any model aimed at describing lepton-nucleus scattering processes. In fact, we have seen in the previous sections that most of the nuclear models, even including FSI in different ways, fail to describe the experimental scaling function, especially the asymmetry, while the RMF is in accord with data reasonably well in a wide kinematical region [51]).

Extension of the Superscaling Approach from Relativistic Mean Field Theory: the SuSAv2 Model

The motivation of the SuSAv2 model is based on the RMF finding that 0th-kind scaling is broken even in the impulse approximation, and generally $f_T(\psi') > f_L(\psi')$. This enhancement of the transverse response is an expected property in order to reproduce the (e, e') cross section after adding the contributions of pion emission and MEC. The SuSAv2 model extends the original SuSA by incorporating the transverse scaling function from the RMF theory [51]. The SuSAv2 model is based on the following four assumptions:

1. f_L superscales, $i.e$, it is independent of the momentum transfer and of the nuclear species. This is supported by experimental data.

2. f_T superscales. Experimentally this is approximately true in the region $\psi < 0$ for a wide range of q ($400 < q < 4000$ MeV/c) [45]. We assume that superscaling can be extended to the whole range of ψ once the contributions from non-QE processes are removed.

3. The RMF model reproduces quite well the relationships between all scaling functions. This assumption is supported by the fact that the RMF model is able to reproduce the longitudinal scaling function, and the fact that it naturally yields the enhancement of the transverse response, $f_T^{ee'} > f_L^{ee'}$.

4. At very high q the effects of FSI disappear and all scaling functions must approach the RPWIA results.

Contrary to what is assumed in the SuSA model, where there is only one universal scaling function used to build all nuclear responses, within SuSAv2 we use three RMF-based *reference* scaling functions (which will be indicated with the symbol $\widetilde{f}$): one for the transverse response, one for the longitudinal isovector responses and another one to describe the longitudinal isoscalar response in electron scattering.

We employ the experimental scaling function $f_{L,\exp}^{ee'}$ as guide in our choices for the *reference* ones. In Fig. 16 we display the RMF longitudinal scaling function, f_L, for several values of q. The functions have been relocated by introducing an energy shift [51] so that the maximum is at $\psi' = 0$. It appears that scaling of first kind is not perfect

and some q-dependence is observed. Although all the curves are roughly compatible with the experimental error bars, the scaling function that produces the best fit to the data corresponds to $q \approx 650$ MeV/c. This is the result of a χ^2-fit to the experimental data of $f_{L,exp}^{ee'}$, as illustrated in the inner plot in Fig. 16.
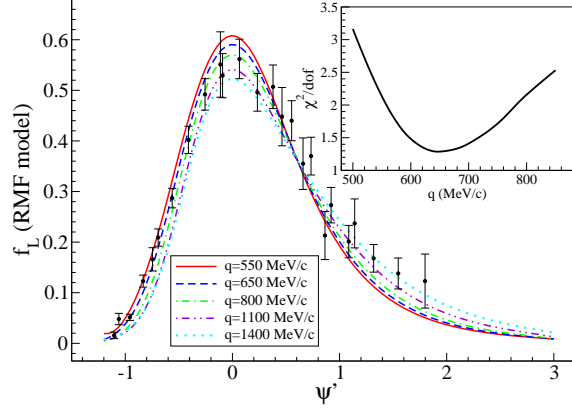

FIG. 16. Longitudinal scaling function for (e, e') computed within RMF. The scaling functions have been shifted to place the maximum at $\psi' = 0$. In the inner smaller plot the reduced-χ^2, taking into account the experimental errors, is presented versus q. The minimum χ^2 is around $q = 650$ MeV/c. Data from Ref. [19].

According to this result, we identify the reference scaling functions with $f_L^{T=1,ee'}$, $f_L^{T=0,ee'}$ and $f_T^{T=1,ee'}$ evaluated within the RMF model at $q = 650$ MeV/c and relocated so that the maximum is at $\psi' = 0$:

$$\widetilde{f}_T \equiv f_T^{T=1,ee'}|_{q=650}^{RMF} \tag{75}$$

$$\widetilde{f}_L^{T=1} \equiv f_L^{T=1,ee'}|_{q=650}^{RMF} \tag{76}$$

$$\widetilde{f}_L^{T=0} \equiv f_L^{T=0,ee'}|_{q=650}^{RMF}, \tag{77}$$

where the isospin scaling functions, for $T = 0, 1$, are defined by dividing the isospin response functions by the corresponding single nucleon contribution from the RFG

$$f_K^{T,ee'} = k_F \frac{R_K^{T e.m.}}{G_K^{T e,e'}}. \tag{78}$$

Thus, by construction, the (e, e') longitudinal scaling function built within SuSAv2 is $f_L|^{SuSAv2} = f_L|_{q=650}^{RMF} \approx f_{L,exp}^{ee'}$. We have parametrized these reference scaling functions by using a skewed-Gumbel function [51].

The neutrino scaling functions necessary to compute the nuclear neutrino responses (see also Section II) are defined from the reference ones as follows:

$$f_L^{VV,\nu(\overline{\nu})}(q) \equiv \widetilde{f}_L^{T=1} \tag{79}$$

$$f_T^{VV,\nu(\overline{\nu})}(q) = f_T^{AA,\nu(\overline{\nu})}(q) = f_{T'}^{VA,\nu(\overline{\nu})}(q) = \widetilde{f}_T, \tag{80}$$

$$f_{CC}^{AA,\nu(\overline{\nu})}(q) = f_{CL}^{AA,\nu(\overline{\nu})}(q) = f_{LL}^{AA,\nu(\overline{\nu})}(q) = \widetilde{f}_L^{T=1}. \tag{81}$$

Finally, in order to implement the approaching of the RMF results to the RPWIA ones at high kinematics, that is, the disappearance of FSI at high q, we build the SuSAv2 L and T scaling functions as linear combinations of the RMF-based and RPWIA reference scaling functions:

$$\mathcal{F}_L^{T=0,1} \equiv \cos^2 \chi(q) \widetilde{f}_L^{T=0,1} + \sin^2 \chi(q) \widetilde{f}_L^{RPWIA} \tag{82}$$

$$\mathcal{F}_T \equiv \cos^2 \chi(q) \widetilde{f}_T + \sin^2 \chi(q) \widetilde{f}_T^{RPWIA}, \tag{83}$$

where the "blending function" $\chi(q)$ is a q-dependent angle given by

$$\chi(q) \equiv \frac{\pi}{2} \left(1 - \left[1 + e^{\left(\frac{q-q_0}{\omega_0}\right)} \right]^{-1} \right) \tag{84}$$

with q_0 and w_0 the transition parameters between RMF and RPWIA prescriptions which are given in Refs. [51, 94]. The reference RPWIA scaling functions, $\widetilde{f}_K^{RPWIA}$, are evaluated at $q = 1100$ MeV/c, where FSI effects are assumed to be negligible, while the reference RMF scaling functions, $\widetilde{f}_K$, are evaluated at $q = 650$ MeV/c and are shown in Fig. 17. The explicit expressions of the RMF ($\widetilde{f}_K$) and RPWIA ($\widetilde{f}_K^{RPWIA}$) scaling functions are given in [51]. With this procedure we get a description of the responses based on RMF behavior at low-intermediate q values, while for higher momentum transfers the RPWIA trend is mimicked. The transition between RMF and RPWIA behaviors occurs at intermediate q-values, namely $\sim q_0$, in a region of width $\sim w_0$.
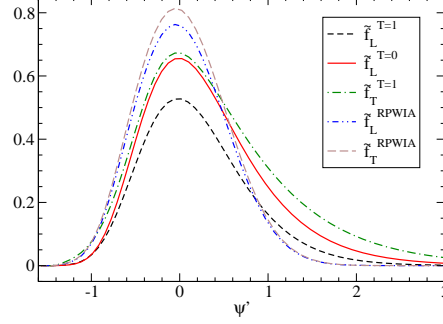

FIG. 17. Reference scaling functions for (e, e') and CC neutrino induced reactions in the SuSAv2 model.

The response functions are simply built as:

$$R_L^{ee'}(q,\omega) = \frac{1}{k_F}\left[\mathcal{F}_L^{T=1}(\psi')G_L^{T=1}(q,\omega) + \mathcal{F}_L^{T=0}(\psi')G_L^{T=0}(q,\omega)\right] \tag{85}$$

$$R_T^{ee'}(q,\omega) = \frac{1}{k_F}\mathcal{F}_T(\psi')\left[G_T^{T=1}(q,\omega) + G_T^{T=0}(q,\omega)\right] \tag{86}$$

$$R_L^{VV,\nu(\overline{\nu})}(q,\omega) = \frac{1}{k_F}\mathcal{F}_L^{T=1}(\psi')G_L^{VV}(q,\omega) \tag{87}$$

$$R_{CC}^{AA,\nu(\overline{\nu})}(q,\omega) = \frac{1}{k_F}\mathcal{F}_L^{T=1}(\psi')G_{CC}^{AA}(q,\omega) \tag{88}$$

$$R_{CL}^{AA,\nu(\overline{\nu})}(q,\omega) = \frac{1}{k_F}\mathcal{F}_L^{T=1}(\psi')G_{CL}^{AA}(q,\omega) \tag{89}$$

$$R_{LL}^{AA,\nu(\overline{\nu})}(q,\omega) = \frac{1}{k_F}\mathcal{F}_L^{T=1}(\psi')G_{LL}^{AA}(q,\omega) \tag{90}$$

$$R_T^{\nu(\overline{\nu})}(q,\omega) = \frac{1}{k_F}\mathcal{F}_T(\psi')\left[G_T^{VV}(q,\omega) + G_T^{AA}(q,\omega)\right] \tag{91}$$

$$R_{T'}^{\nu(\overline{\nu})}(q,\omega) = \frac{1}{k_F}\mathcal{F}_T(\psi')G_{T'}^{VA}(q,\omega). \tag{92}$$

Furthermore, in order to reproduce the peak position of RMF and RPWIA scaling functions within SuSAv2 we consider a q-dependent energy shift, namely, $E_{shift}(q)$. This quantity modifies the scaling variable $\psi(q,\omega) \longrightarrow \psi' = \psi(q, \omega - E_{shift})$. In particular, we build this function $E_{shift}(q)$ from the results of the RMF and RPWIA models presented in [51]. The choice of $E_{shift}(q)$ depending on the particular q-domain region considered is solely based on the behavior of the experimental cross sections and their comparison with our theoretical predictions (see results in Section VII).

In Section VII we will show that the SuSAv2 model describes more accurately the neutrino induced reactions than the semiphenomenological SuSA approach. This result mainly comes from the q-dependence on the energy shift, the enhancement on the transverse response via RMF prescriptions as well as the possibility of separating scaling functions into isoscalar and isovector contributions.

IV. Relativistic model for CC MEC and 2p2h responses

In this section we present a fully relativistic model of meson exchange currents (MEC) to describe the inclusive neutrino scattering in the two-nucleon emission channel (2p-2h). The present approach was developed in the RFG model of Ref. [95], where the difficulties of the relativistic reaction are overcome thanks to the plane waves used for the single-nucleon states. However this channel is cumbersome on the computational side, if compared to the analytical simplicity of the 1p-1h responses.

The 2p-2h hadronic tensor is given by summation (integration) over all the 2p-2h excitations of the RFG with two holes $\mathbf{h}_1$, $\mathbf{h}_2$, and two particles $\mathbf{p}'_1$, $\mathbf{p}'_2$, in the final state, with $h_i < k_F$ and $p'_i > k_F$

$$W^{\mu\nu}_{2\text{p}2\text{h}} = \frac{V}{(2\pi)^9} \int d^3p'_1 d^3p'_2 d^3h_1 d^3h_2 \frac{m_N^4}{E_1 E_2 E'_1 E'_2} w^{\mu\nu}(\mathbf{p}'_1, \mathbf{p}'_2, \mathbf{h}_1, \mathbf{h}_2)\, \delta(E'_1 + E'_2 - E_1 - E_2 - \omega)$$
$$\times \Theta(p'_1, h_1)\Theta(p'_2, h_2)\delta(\mathbf{p}'_1 + \mathbf{p}'_2 - \mathbf{q} - \mathbf{h}_1 - \mathbf{h}_2)\,, \tag{93}$$

where the Pauli blocking function Θ is defined as the product of step-functions

$$\Theta(p', h) \equiv \theta(p' - k_F)\theta(k_F - h). \tag{94}$$

The 2p-2h equivalent to the single-nucleon hadronic tensor inside the integral is called $w^{\mu\nu}(\mathbf{p}'_1, \mathbf{p}'_2, \mathbf{h}_1, \mathbf{h}_2)$, and describes two-nucleon transitions with given initial and final momenta, summed up over spin and isospin,

$$w^{\mu\nu}(\mathbf{p}'_1, \mathbf{p}'_2, \mathbf{h}_1, \mathbf{h}_2) = \frac{1}{4} \sum_{s_1 s_2 s'_1 s'_2} \sum_{t_1 t_2 t'_1 t'_2} j^\mu(1', 2', 1, 2)^*_A j^\nu(1', 2', 1, 2)_A\,. \tag{95}$$

Here the 2p-2h current function, in short-hand notation for the full spin-isospin-momentum dependence, is

$$j^\mu(1', 2', 1, 2) \equiv j^\mu(\mathbf{p}'_1 s'_1 t'_1, \mathbf{p}'_2 s'_2 t'_2, \mathbf{h}_1 s_1 t_1, \mathbf{h}_2 s_2 t_2) \tag{96}$$

and $j^\mu(1', 2', 1, 2)_A$ refers to the direct minus exchange matrix elements

$$j^\mu(1', 2', 1, 2)_A \equiv j^\mu(1', 2', 1, 2) - j^\mu(1', 2', 2, 1)\,. \tag{97}$$

The factor $1/4$ in Eq. (95) accounts for the antisymmetry of the two-body wave function, to avoid double counting in the number of final 2p-2h states. The exchange $1 \leftrightarrow 2$ in the second term implies implicitly the exchange of momenta, spin and isospin quantum numbers.

Momentum conservation allows to integrate over $\mathbf{p}'_2$ to compute the 2p-2h response functions as a 9-dimensional integral

$$R^K_{2\text{p}2\text{h}} = \frac{V}{(2\pi)^9} \int d^3p'_1 d^3h_1 d^3h_2 \frac{m_N^4}{E_1 E_2 E'_1 E'_2} \Theta(p'_1, h_1)\Theta(p'_2, h_2) r^K(\mathbf{p}'_1, \mathbf{p}'_2, \mathbf{h}_1, \mathbf{h}_2)\, \delta(E'_1 + E'_2 - E_1 - E_2 - \omega), \tag{98}$$

where $\mathbf{p}'_2 = \mathbf{h}_1 + \mathbf{h}_2 + \mathbf{q} - \mathbf{p}'_1$. The five elementary response functions for a 2p2h excitation, r^K, are defined in terms of the elementary hadronic tensor $w^{\mu\nu}$, for the five indices $K = CC, CL, LL, T, T'$.

Due to azimuthal symmetry of nucleon emission around the z axis, defined by $\mathbf{q}$, we can fix the azimuthal angle of particle 1', by setting $\phi'_1 = 0$, and multiplying by a factor 2π. Finally, the Dirac delta-function enables us to integrate over p'_1, and so the integral in Eq. (98) can be reduced to seven dimensions. The details of the integration method can be found in Ref. [96].

To specify a model for the two-body current matrix elements $j^\mu(1', 2', 1, 2)$, we consider MEC containing the Feynman diagrams depicted in Fig. 18. The different contributions have been taken from the pion production model of [97].

Our MEC are given as the sum of four two-body currents:

$$j^\mu(1', 2, 1, 2) = j^\mu_\text{sea} + j^\mu_\pi + j^\mu_\text{pole} + j^\mu_\Delta, \tag{99}$$

corresponding in Fig. 18 to the seagull (diagrams a,b), pion in flight (c), pion-pole (d,e) and $\Delta(1232)$ excitation
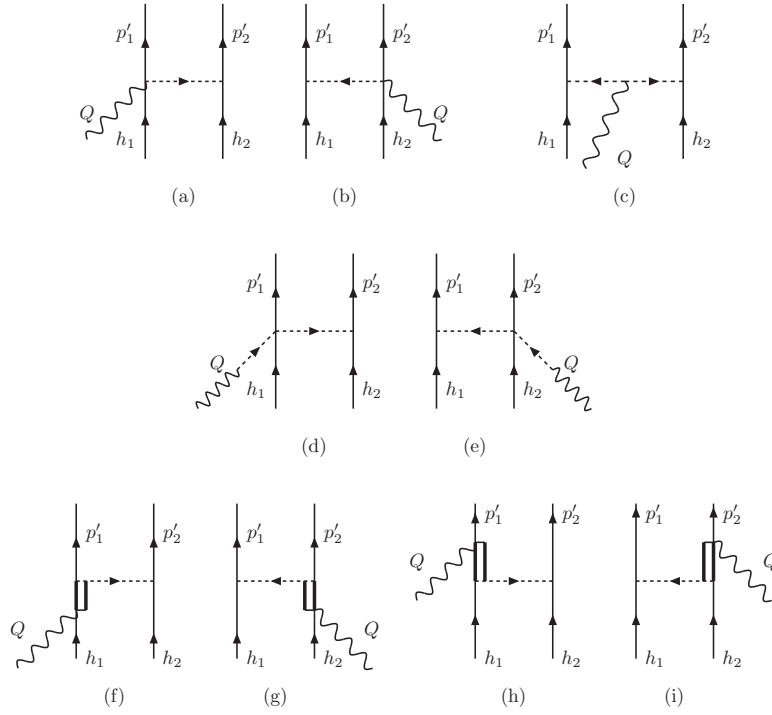
FIG. 18. Feynman diagrams for the electroweak MEC model discussed in this review [95].

(f,g,h,i). Their expressions are given by

$$j_{\text{sea}}^{\mu} = \left[I_V^{\pm}\right]_{1'2',12} \frac{f^2}{m_\pi^2} V_{\pi NN}^{s_1' s_1}(\mathbf{p}_1', \mathbf{h}_1)$$

$$\times \bar{u}_{s_2'}(\mathbf{p}_2') \left[F_1^V(Q^2)\gamma_5\gamma^\mu + \frac{F_\rho\left(k_2^2\right)}{g_A}\gamma^\mu\right] u_{s_2}(\mathbf{h}_2) + (1 \leftrightarrow 2) \tag{100}$$

$$j_\pi^\mu = \left[I_V^{\pm}\right]_{1'2',12} \frac{f^2}{m_\pi^2} F_1^V(Q^2) V_{\pi NN}^{s_1' s_1}(\mathbf{p}_1', \mathbf{h}_1) V_{\pi NN}^{s_2' s_2}(\mathbf{p}_2', \mathbf{h}_2)\left(k_1^\mu - k_2^\mu\right) \tag{101}$$

$$j_{\text{pole}}^\mu = \left[I_V^{\pm}\right]_{1'2',12} \frac{f^2}{m_\pi^2} \frac{F_\rho\left(k_1^2\right)}{g_A} \frac{Q^\mu \bar{u}_{s_1'}(\mathbf{p}_1') \displaystyle{\not{Q}} u_{s_1}(\mathbf{h}_1)}{Q^2 - m_\pi^2} V_{\pi NN}^{s_2' s_2}(\mathbf{p}_2', \mathbf{h}_2)$$

$$+(1 \leftrightarrow 2) \tag{102}$$

$$j_\Delta^\mu = \frac{f^* f}{m_\pi^2} V_{\pi NN}^{s_2' s_2}(\mathbf{p}_2', \mathbf{h}_2) \bar{u}_{s_1'}(\mathbf{p}_1') \left\{\left[U_F^{\pm}\right]_{1'2',12} k_2^\alpha G_{\alpha\beta}(h_1 + Q)\Gamma^{\beta\mu}(h_1, Q)\right.$$

$$\left.+ \left[U_B^{\pm}\right]_{1'2',12} k_2^\beta \hat{\Gamma}^{\mu\alpha}(p_1', Q) G_{\alpha\beta}(p_1' - Q)\right\} u_{s_1}(\mathbf{h}_1) + (1 \leftrightarrow 2). \tag{103}$$

In these equations we use the following notation. The momentum transfer to ith nucleon is $k_i^\mu = p_i'^\mu - h_i^\mu$. The πNN interaction and the pion propagator are contained in the following spin-dependent function:

$$V_{\pi NN}^{s_1' s_1}(\mathbf{p}_1', \mathbf{h}_1) \equiv \frac{\bar{u}_{s_1'}(\mathbf{p}_1')\gamma_5 \displaystyle{\not{k}_1} u_{s_1}(\mathbf{h}_1)}{k_1^2 - m_\pi^2}. \tag{104}$$

We have also defined the isospin operators

$$I_V^{\pm} = (I_V)_x \pm i(I_V)_y \tag{105}$$

$$\boldsymbol{I}_V = i\boldsymbol{\tau}(1) \times \boldsymbol{\tau}(2), \tag{106}$$

where the $+(-)$ sign refers to neutrino (antineutrino) scattering. In the Δ current, the forward, $U_F^{\pm} = U_{Fx} \pm iU_{Fy}$, and backward, $U_B^{\pm} = U_{Bx} \pm iU_{By}$, isospin transition operators are obtained from the cartesian components of the

operators

$$U_{\mathrm{Fj}} = \sqrt{\frac{3}{2}} \sum_i \left(T_i T_j^\dagger \right) \otimes \tau_i, \quad U_{\mathrm{Bj}} = \sqrt{\frac{3}{2}} \sum_i \left(T_j T_i^\dagger \right) \otimes \tau_i, \tag{107}$$

where $\vec{T}$ is an isovector transition operator from isospin $\frac{3}{2}$ to $\frac{1}{2}$, normalized as

$$T_i T_j^\dagger = \frac{2}{3}\delta_{ij} - \frac{i}{3}\epsilon_{ijk}\tau_k. \tag{108}$$

The coupling constants in the MEC are $f = 1$, $g_A = 1.26$, and $f^* = 2.13$. The electroweak form factors F_1^V and F_ρ in the seagull and pionic currents are taken from Ref. [97]. To take into account the finite size of the hadrons, we apply phenomenological strong form factors (not written explicitly in the MEC) in all the $NN\pi$ and $N\Delta\pi$ vertices

$$F_{\pi NN}(k) = \frac{\Lambda_\pi^2 - m_\pi^2}{\Lambda_\pi^2 - k^2}, \quad F_{\pi N\Delta}(k) = \frac{\Lambda_\Delta^2}{\Lambda_\Delta^2 - k^2}, \tag{109}$$

where the cutoff constants are $\Lambda_\pi = 1.3$ GeV and $\Lambda_\Delta = 1.15$ GeV. These values of the strong form factors in the MEC are similar to past works on the two nucleon emission responses for electron scattering both in the non-relativistic [98], and relativistic Fermi gas model [99]. In the formalism presented here, which is an extension of the Torino model [100], we use still the same strong form factors for consistency with previous modelling.

In our approach the weak $N \to \Delta$ transition vertex tensor in the forward current, $\Gamma^{\beta\mu}(P,Q)$ is given by

$$\Gamma^{\beta\mu}(P,Q) = \frac{C_3^V}{m_N} \left(g^{\beta\mu}\, \slashed{Q} - Q^\beta\gamma^\mu \right)\gamma_5 + C_5^A g^{\beta\mu}. \tag{110}$$

We have kept only the C_3^V and C_5^A form factors and neglected the smaller contributions of the others. They are taken from [97]. The additional terms have been neglected because they are of order $1/m_N^2$ or negligible for the intermediate energy kinematics of interest for the quasielastic regime. Moreover the vector part of the vertex (110) is equivalent to the Δ operator used in ref [100] for electron scattering.

The corresponding vertex tensor entering in the backward current is defined by

$$\hat{\Gamma}^{\mu\alpha}(P',Q) = \gamma^0 \left[\Gamma^{\alpha\mu}(P',-Q) \right]^\dagger \gamma^0. \tag{111}$$

The Δ-propagator takes into account the finite decay width of the $\Delta(1232)$ by the prescription

$$G_{\alpha\beta}(P) = \frac{\mathcal{P}_{\alpha\beta}(P)}{P^2 - M_\Delta^2 + iM_\Delta\Gamma_\Delta + \frac{\Gamma_\Delta^2}{4}}, \tag{112}$$

where the width $\Gamma_\Delta(P^2)$ depends only on the Δ invariant mass. The explicit dependence is taken from [99].

The projector $\mathcal{P}_{\alpha\beta}(P)$ over spin-$\frac{3}{2}$ particles is given by

$$\mathcal{P}_{\alpha\beta}(P) = -(\slashed{P} + M_\Delta) \left[g_{\alpha\beta} - \frac{1}{3}\gamma_\alpha\gamma_\beta - \frac{2}{3}\frac{P_\alpha P_\beta}{M_\Delta^2} + \frac{1}{3}\frac{P_\alpha\gamma_\beta - P_\beta\gamma_\alpha}{M_\Delta} \right]. \tag{113}$$

In the present approach of MEC we do not consider the nucleon pole (NP) terms, also called nucleon correlation current, with an intermediate nucleon propagation. These contributions have been evaluated in some works for electron scattering [98, 101] and for neutrino scattering [76, 102, 103]. But these approaches are problematic from the theoretical point of view due to the presence of double poles in the hadronic tensor, that need to be regularized in some way not free from ambiguities. Alternative approaches (for instance [104]) include these contributions in the nuclear wave function, in form of Jastrow correlations. A third possibility is to include the nuclear correlation effects, at least partially, by using a phenomenological scaling function extracted from (e,e') data, as discussed in Sect. III.

Note also that our MEC do not include heavier mesons such as ρ-exchange, which is expected to provide a smaller contribution than the leading pion-exchange for the energies of interest.

The computation of the 2p-2h responses in the RFG model presents two main difficulties: the evaluation of the 2p-2h hadronic tensor by performing the spin and isospin traces, and the evaluation of the 7D integral over the phase space. The first problem in fact can be faced with analytical results for the 2p-2h tensor $w^{\mu,\nu}(\mathbf{p}_1', \mathbf{p}_2', \mathbf{h}_1, \mathbf{h}_2)$, but hundreds of thousands terms arise already in the electron scattering case [100] and many more are present for neutrino scattering. We then follow the alternative and easier approach of computing numerically the Dirac matrix elements of the currents and then summing over spins.
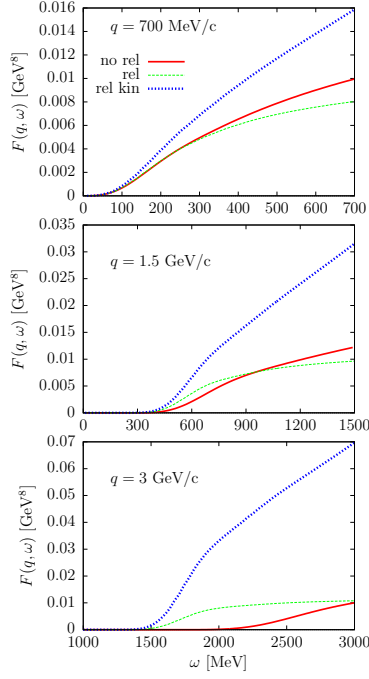
FIG. 19. Effect of implementing relativistic kinematics in a non-relativistic calculation of $F(q,\omega)$. No rel: non-relativistic result. Rel kin: relativistic kinematics only without the relativistic factors m_N/E. Rel: fully relativistic result. [96].

The second problem consists on computing efficiently the 7D integral of the MEC. This can be done in several ways. The integration in the Laboratory system was studied in Ref. [96] in the context of the phase space integral

$$
F(q,\omega) \equiv \int d^3p_1' d^3h_1 d^3h_2 \frac{m_N^4}{E_1 E_2 E_1' E_2'} \Theta(p_1', h_1)\Theta(p_2', h_2)\,\delta(E_1' + E_2' - E_1 - E_2 - \omega). \tag{114}
$$

The study of this universal function of the RFG was done in detail in Ref. [96] for relativistic and non relativistic kinematics.

One important conclusion of that study is presented in Fig. 19, where we compare the relativistic and non relativistic phase space functions. The latter uses non-relativistic kinematics in the delta of energies and has no boost factors m_N/E inside the integral. As expected the relativistic effect increases with the momentum transfer. We also show that using relativistic kinematics without the boost factors worsens the results. This shows that this procedure of "relativizing" a non-relativistic MEC model using relativistic kinematics is not advisable.

In Ref. [105] we followed the alternative approach of computing the 7D integral going to the center of mass frame of the final two-nucleon system. There analytical results were found for the phase space function in the non-Pauli blocking regime. The angular distribution of the final particles in the phase space integral in the CM system was found to be isotropic (independent on the emission angle), as it is assumed in the Monte Carlo analyses of two nucleon emission for neutrino scattering [106]. However, these distributions are going to change after including the effects of the MEC, because the angular distribution for fixed momenta, $\mathbf{h}_1$ and $\mathbf{h}_2$, is multiplied by the 2p-2h hadronic tensor. Further studies are needed to correct the angular distribution from the isotropic assumption, to reduce the systematic uncertainties of neutrino event generators in the 2p-2h channel.

The 2p-2h inclusive cross section requires to compute two electromagnetic response functions, $R^{T,L}$, for (e,e') reactions and five weak response functions, $R^{CC,CL,LL,T,T'}$, for (ν_μ,μ^-). All these responses were computed and analyzed in Ref. [95].

The numerical results of our model are in agreement with the calculations of [100] and with the much more recent calculation of [70], which uses the same theoretical MEC model. These results for the response functions have been parametrized in the kinematic range relevant for electron scattering [94], and for the current neutrino quasielastic scattering experiments [107]. The parametrization is convenient because in neutrino scattering there is an additional integration over the incident neutrino flux to obtain the cross section. The parametrization is available from the authors; it has been already used in other analyses [108] and has been implemented in Monte Carlo event generator GENIE [109].
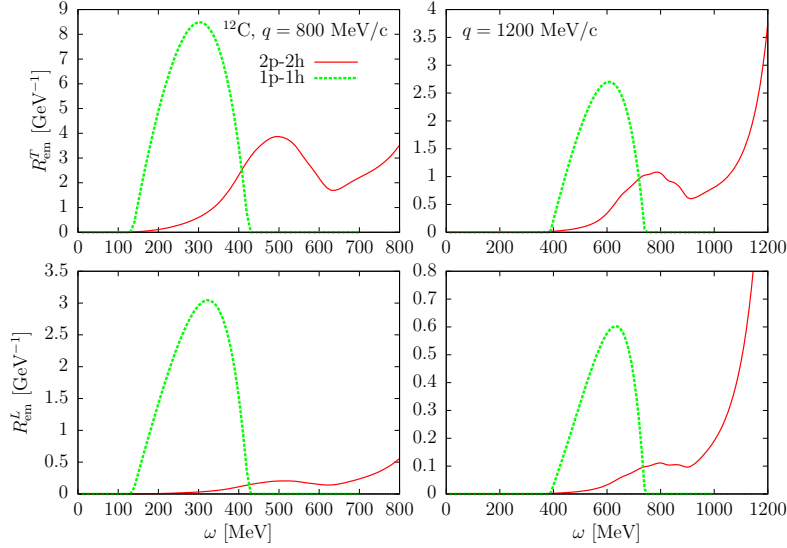
FIG. 20. Comparison between 1p-1h and 2p-2h response functions for electron scattering off ^{12}C for two values of the momentum transfer. The Fermi momentum of the RFG is $k_F = 228$ MeV/c [95].

To illustrate the qualitative predictions of the RFG model, in Figs. 20 and 21 we compare the 1p-1h and 2p-2h neutrino responses for two values of the momentum transfer for electron and neutrino scattering, respectively. The 1p-1h responses only contain the one-body (OB) current. For these values of q large MEC effects are found. The 2p-2h responses present a maximum due to the presence of the Δ propagator in the Δ current. The MEC effects are similar in the T and T' responses. The 2p-2h contribution to (e, e') is predominantly transverse, due to dominance of the Δ excitation in the transverse vector current. The MEC effects in the CC response are relatively much larger than in the transverse ones. This comes from a large longitudinal contribution of the axial MEC. However, each response function appears in the cross section multiplied by a kinematic factor, which slightly alters the relative contribution to the cross section. In particular, the three responses R^{CC}, R^{CL} and R^{LL} largely cancel each other, yielding a small charge/longitudinal cross section. In figs. 20 and 21 only the real part of the denominator of the Δ propagator has been considered in the calculation of the MEC, a prescription taken also in Refs. [95, 100].

In our model the elementary 2p-2h response functions contain direct-direct, exchange-exchange and direct-exchange contributions due to the antisymmetry of the 2p-2h states. The exchange-exchange term is identical to the direct-direct for the inclusive reactions considered here. Therefore one can write the elementary response functions as direct minus direct-exchange contribution. For instance for the T responses of neutrino scattering in the pp emission channel we have

$$r_{pp}^T = 4 \sum_{\mu=1}^{2} \sum_{s_1 s_2 s_1' s_2'} \left\{ \left| J_{pp}^\mu(1'2'; 12) \right|^2 - \text{Re } J_{pp}^\mu(1'2'; 12)^* J_{pp}^\mu(2'1'; 12) \right\}, \tag{115}$$

where $J_{pp}^\mu(1'2'; 12)$ is the matrix element for pp emission with neutrinos. The first term in Eq. (115) is the "direct" contribution, and the second one is the "exchange" contribution, actually being the interference between the direct and exchange matrix elements. There are similar expressions for the remaining response functions (see Ref. [95] for details).

In other models of 2p-2h based on the Fermi gas, the exchange interference contributions are disregarded. Specifically they are neglected in the models of Lyon [76, 102] and Valencia [103, 111], because they involve higher dimensional integrals than the direct terms, which can be reduced to low dimensions within some assumptions.

To quantify the importance of the exchange, this contribution was separated in our model in Ref. [95]. It was found to be typically about 25% of the 2p-2h inclusive cross section. Later, it was separated in the individual channels of neutron-proton (np) and proton-proton (pp) emission in Refs. [110, 112]. An example is given in Fig. 22, where we see the transverse, T and T', response functions for np and pp emission with neutrinos. In the np case the exchange interference reduces the strength by 50%. This example shows that the ratio pp/np critically depends on the treatment of the exchange interference.

In other works [113, 114] we have developed some assumptions which simplify and reduce the number of nested integrations to calculate the inclusive 2p-2h responses. In the first of them, Ref. [113], we used the "frozen nucleon
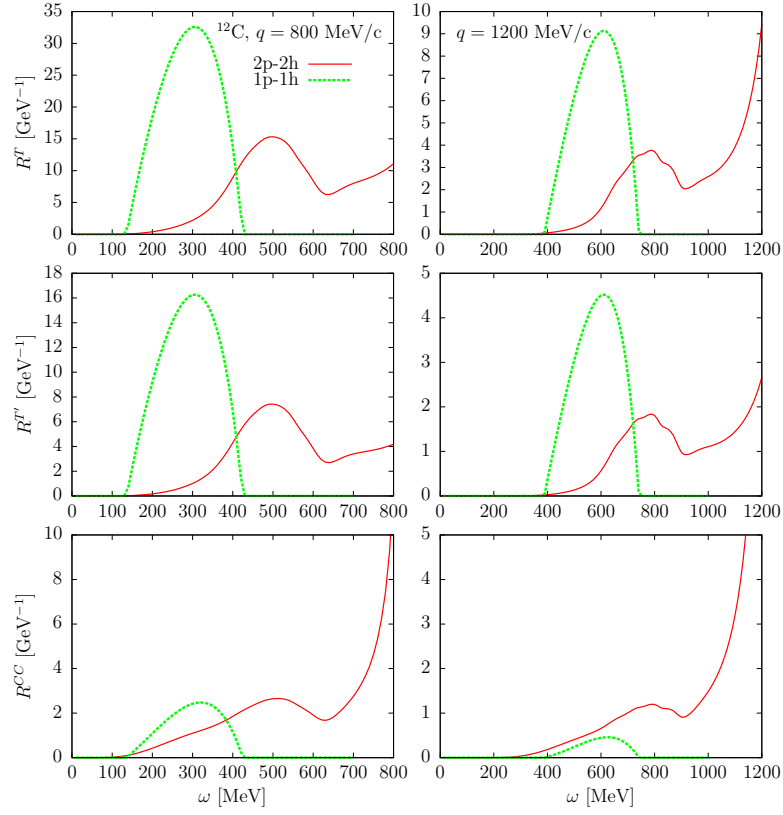
FIG. 21. Comparison between 1p-1h and 2p-2h response functions for CC neutrino scattering off ^{12}C for two values of the momentum transfer. The Fermi momentum of the RFG is $k_F = 228$ MeV/c [95].
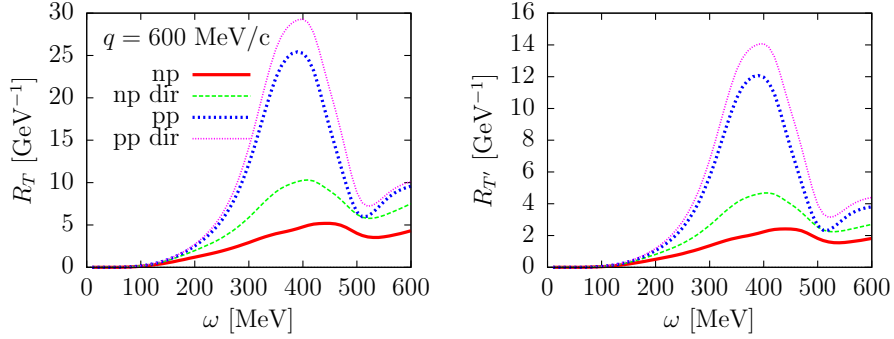

FIG. 22. Separate pp and np contributions to the neutrino T and T' 2p-2h response functions of ^{12}C, for $q = 600$ MeV/c, compared to the direct contributions obtained by neglecting the direct-exchange interference. The value of the Fermi momentum $k_F = 228$ MeV/c [110].

approximation" to reduce the 7-dimensional integral to just a single integration, by assuming the initial nucleons to be at rest. The strong dependence on the kinematics near the Δ peak arising in the frozen approximation was avoided by using a smeared Δ propagator that was parametrized for the relevant values of the momentum transfer, in order to make these approximate results consistent with those calculated with the full integration procedure. In the second work, Ref. [114], we took an approach similar to that of the IFIC-Valencia model [103, 111]: we developed a convolution model of the elementary 2p-2h responses, given in Eq. (95), with two 1p-1h responses (Lindhard functions) sharing the energy and momentum transfer from the electroweak probe. The importance of these works is two-fold: from the computational point of view, reducing the time to evaluate the inclusive 2p-2h responses makes these models suitable to be incorporated in the Monte Carlo event generators; additionally, with the second work

[114], we also can incorporate the direct-exchange terms, that appear in Eq. (95), in the calculation of the inclusive 2p-2h response functions in the same or similar fashion as it is done in the Valencia model [103]. But this is even more than what is included in the original Valencia model [103] in this respect, because in this last model those terms were not considered because their calculation was extremely difficult with the technique of the Cutkosky rules.

V. Pion production in the resonance region

There are several reasons that make pion production relevant for present and future accelerator-based neutrino oscillation experiments. Neutral current π^0 production is an important background in the electron neutrino and antineutrino appearance analyses due to the misidentification of the photons from the π^0 decay with the electron or positron signal. Also, the final state for events with a pion produced in the primary vertex may mimic that of a QE one i) if the pion is not detected, and ii) if due to FSI the pion is absorbed. Finally, in the few-GeV energy region, the number of events observed in the far and near detectors arising from neutrino-induced pion production competes with those from the quasielastic process. Since pions can be detected, for example, in coincidence with the final lepton and possibly other hadrons, a good understanding of the pion production mechanisms could help to increase the statistics of events that are selected for the reconstruction of the neutrino energy.

To illustrate the relative magnitude of QE and non-QE processes, in Fig. 23(a) we show the ν_e-^{12}C inclusive Q_{QE}^2[3] differential cross section averaged with the T2K flux, and in Fig. 23(b) the ν_μ total cross section on C_8H_8 target. Three different contributions are shown: i) QE scattering computed within the SuSAv2 model (Sect. III E), ii) the 2p2h MEC (Sect. IV), and iii) an inelastic contribution containing mainly one-pion production (labelled as 1π), that will be described below [4]. One observes that for the ν_e T2K flux the QE and 1π contributions are similar in magnitude. This should not be surprising since, even though the T2K flux peaks at around $E_\nu = 0.5$ GeV, it has a long tail extending up to 10 GeV [116]. For the total cross section, Fig. 23(b), the QE contribution dominates up to $E_\nu \approx 1$ GeV. For higher neutrino energies the QE and 1π contributions are comparable.
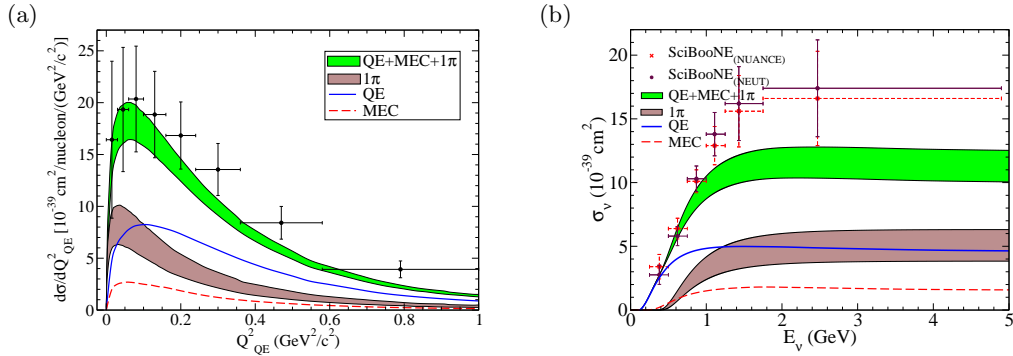

FIG. 23. (a) We show the CC-inclusive T2K flux-folded ν_e-^{12}C Q_{QE}^2 differential cross section per nucleon. (b) The CC ν_μ total cross section on C_8H_8 is presented. Experimental data are from [116] (a) and [117] (b). Theoretical predictions for QE, non-QE (1π) and the 2p2h MEC are shown separately. Plots updated from Ref. [115].

The motivation of the non-QE SuSAv2 model used in Fig. 23 is to extend the superscaling arguments, previously applied in the QE domain, to the Δ resonance region [53, 118]. Hence, the underlying idea is that pion production in the Δ region is indeed strongly dominated by the excitation of the Δ resonance. The first step is to define an experimental scaling function in this inelastic region, f^{non-QE}. For that we subtract the QE and 2p2h MEC contributions to the inclusive electron scattering experimental cross section:

$$\left(\frac{d^2\sigma}{d\Omega d\omega}\right)_{non-QE} \equiv \left(\frac{d^2\sigma}{d\Omega d\omega}\right)_{exp} - \left(\frac{d^2\sigma}{d\Omega d\omega}\right)_{QE,SuSAv2}^{1p1h} - \left(\frac{d^2\sigma}{d\Omega d\omega}\right)_{MEC}^{2p2h}. \tag{116}$$

The result is called non-QE cross section. Then the superscaling function is constructed as

$$f^{non-QE}(\psi_\Delta) = k_F \frac{\left(\frac{d^2\sigma}{d\Omega d\omega}\right)_{non-QE}}{\sigma_M(v_L G_L^\Delta + v_T G_T^\Delta)} \tag{117}$$

---

[3] Q_{QE}^2 is the reconstructed four-momentum transfer, obtained assuming an initial state nucleon at rest with a constant binding energy.

[4] Notice that Figs. 23(a) and (b) are updated versions of those originally shown in Ref. [115]. Here the 2p2h MEC contains the vector-vector, vector-axial and axial-axial contributions while in Ref. [115] only its vector-vector contribution was available.

where $G_{L,T}^{\Delta}$ are the single-nucleon functions for the $\gamma N\Delta$ vertex and ψ_Δ is the Δ scaling function (the explicit expressions can be found in Refs. [53, 118, 119]).

The function $f^{non-QE}(\psi_\Delta)$ is represented in Fig. 24(a) for a large set of inclusive electron-^{12}C scattering data. One observes that in the region $\psi_\Delta < 0$ scaling occurs but it is not as good as in the QE case. For that reason, the scaling function is parametrized as a broad band that accounts for the spread of the data. This band can be understood as the systematic error attached to the model. Notice that in the region $\psi_\Delta > 0$, as expected, scaling breaks because contributions from processes beyond the Delta production start to be important. Thus, the predictions of this model beyond the Delta peak should be taken with caution. In Fig. 24(b) we show that the model works well for inclusive electron scattering (see more in [115]).
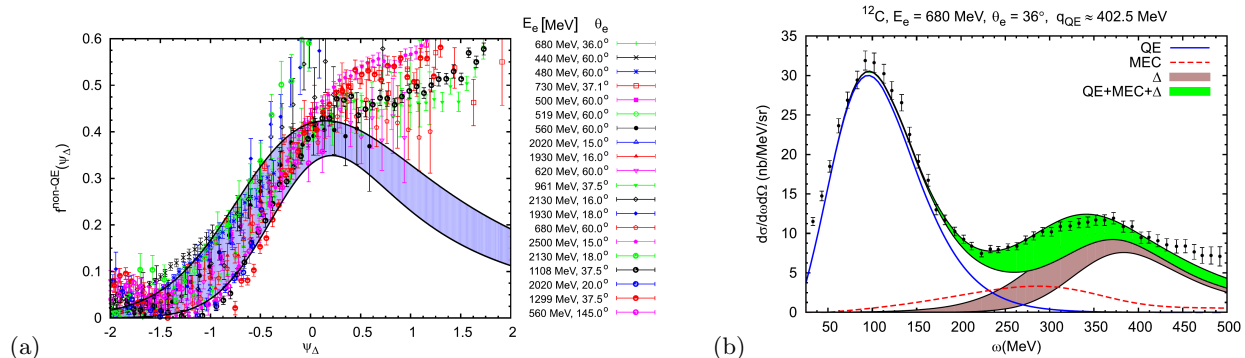

FIG. 24. (a) We show the $f^{non-QE}(\psi_\Delta)$, the experimental data can be found in [120]. (b) We compare inclusive electron-^{12}C data [121] with the predictions of the QE and non-QE SuSAv2, and the 2p2h MEC contribution. These plots are taken from Ref. [115].

Inclusive models like superscaling-based approaches, or the model of Ref. [76], do not provide any information about the final state hadrons. For that, one normally uses theoretical approaches that focus on one particular reaction channel. The inclusive signal should be recovered by adding all channels allowed for the given energy and momentum transferred and integrating over the hadronic variables. This implies, therefore, the non-trivial task of modelling all those possible reaction channels.

In an effort to improve our current knowledge on the neutrino-induced pion production, in recent years the Mini-BooNE [122–124], MINERvA [125–129] and T2K [130] collaborations have reported (pion detected) differential cross sections for NC and, mainly, CC neutrino-induced pion production on different nuclear targets. It is important to stress that up to date, no model is able to simultaneously reproduce and explain the MiniBooNE, MINERvA and T2K data sets [131–134]. This problem is sometimes referred as the "pion puzzle", and its solution is crucial for future oscillation experiments like DUNE, in which pion production plays a major role. From the theoretical side, we aim at providing support to improve our understanding of these and forthcoming data in a more consistent way. Accordingly, in this section we focus on the single-pion production (SPP) process, which is the dominant one in the resonance region and is typically characterized by invariant masses [5] going from the pion threshold to $W < 1.8 - 2$ GeV. The strategy shared by most approaches is based on the idea that the lepton interacts with only one nucleon in the nucleus. This allows one to decompose this complex problem into different pieces: 1) the elementary vertex, 2) the nuclear framework, including the description of the initial and final nuclear states, and 3) the final-state interactions. In what follows we review some of the features of this complex problem. For further reading we refer to the recent review articles [3, 4, 135, 136].

A. Elementary vertex

One finds the following reaction channels for SPP off a free nucleon induced by neutral current interactions (EM or WNC):

$$\begin{aligned}
\gamma + p \to \pi^+ + n\,, \quad \gamma + n \to \pi^- + p\,, \\
\gamma + p \to \pi^0 + p\,, \quad \gamma + n \to \pi^0 + n\,.
\end{aligned} \tag{118}$$

---

[5] The invariant mass W is defined as $W^2 = s = (Q + P_i)^2 = (K_\pi + P_f)^2$, with the four vectors defined in Fig. 25(a).

γ represents a real (photoproduction) or virtual (electroproduction) photon. For WNC interaction, the virtual photon is replaced by a Z^0 boson. In the case of neutrino (W^+ exchanged) and antineutrino (W^-) CC interactions, one has:

$$\begin{aligned}
W^+ + p &\rightarrow \pi^+ + p\,, & W^- + n &\rightarrow \pi^- + n\,, \\
W^+ + n &\rightarrow \pi^0 + p\,, & W^- + p &\rightarrow \pi^0 + n\,, \\
W^+ + n &\rightarrow \pi^+ + n\,, & W^- + p &\rightarrow \pi^- + p\,.
\end{aligned} \tag{119}$$

The process is depicted in Fig. 25(a), and it will be discussed in what follows.

a.   Cross Section

The differential cross section for SPP off the nucleon in a reference frame of collinear incident particles is:

$$\frac{d\sigma}{d\mathbf{k}_f d\mathbf{k}_\pi} = \frac{K}{\phi} \frac{\mathcal{R}_X}{(2\pi)^5} \eta_{\mu\nu} h^{\mu\nu} \delta(\varepsilon_i + E_i - \varepsilon_f - E_\pi - E_f)\,, \tag{120}$$

with

$$K = \frac{1}{2\varepsilon_i \, \varepsilon_f} \frac{1}{2E_i \, E_f} \frac{1}{2E_\pi}\,, \quad \phi = \left| \frac{\mathbf{k}_i}{\varepsilon_i} - \frac{\mathbf{p}_i}{E_i} \right|\,. \tag{121}$$

This expression is valid for EM, CC and WNC interactions. The factor $\mathcal{R}_X$, where the subscript X refers to the type of interaction, include the boson propagator as well as the coupling constants at the leptonic and hadronic vertices:

$$\mathcal{R}_{EM} = \left(\frac{4\pi\alpha}{Q^2} \right)^2\,, \quad \mathcal{R}_{CC} = (G_F \cos\theta_c)^2\,, \quad \mathcal{R}_{WNC} = G_F^2\,. \tag{122}$$

$\eta_{\mu\nu}$ is the leptonic tensor discussed in Sect. II. We define the hadronic tensor as

$$h^{\mu\nu} = 2m_{N,i} m_{N,f} \overline{\sum}_{S_i S_f} (J^\mu)^* J^\nu. \tag{123}$$

with the hadronic current

$$J^\mu = \bar{u}(\mathbf{p}_f, S_f) \mathcal{O}_{1\pi}^\mu u(\mathbf{p}_i, S_i). \tag{124}$$

$u(\mathbf{p}_{i,f}, S_{i,f})$ represent the free Dirac spinors for the initial and final state nucleons with spin projection S_i and S_f. [6] $\mathcal{O}_{1\pi}^\mu$ is the transition operator between the initial one-nucleon state and the final one-nucleon one-pion ($N\pi$) state.

We can use the energy-conservation delta function to integrate over k_π. This leads to

$$\frac{d^5\sigma}{d\varepsilon_f d\Omega_f d\Omega_\pi} = \frac{K}{\phi} \frac{\varepsilon_f k_f E_\pi k_\pi}{f_{rec}^{(k_\pi)}} \frac{\mathcal{R}_X}{(2\pi)^5} \eta_{\mu\nu} h^{\mu\nu}\,, \tag{125}$$

where we have introduced the nucleon recoil function

$$f_{rec}^{(k_\pi)} = \left| 1 + \frac{E_\pi}{E_f} \left(1 - \frac{\mathbf{k}_\pi \cdot (\mathbf{q} + \mathbf{p}_i)}{k_\pi^2} \right) \right|\,. \tag{126}$$

Alternatively, if we want to study distributions as a function of the pion energy, we can integrate over k_f. In this case one obtains

$$\frac{d^5\sigma}{d\Omega_f dE_\pi d\Omega_\pi} = \frac{K}{\phi} \frac{\varepsilon_f k_f E_\pi k_\pi}{f_{rec}^{(k_f)}} \frac{\mathcal{R}_X}{(2\pi)^5} \eta_{\mu\nu} h^{\mu\nu}\,, \tag{127}$$

with

$$f_{rec}^{(k_f)} = \left| 1 + \frac{\varepsilon_f}{E_f} \left(1 - \frac{\mathbf{k}_f \cdot (\mathbf{k}_i + \mathbf{p}_i - \mathbf{k}_\pi)}{k_f^2} \right) \right|\,. \tag{128}$$

---

[6] The convention for the plane wave and Dirac spinor is $\psi(\mathbf{x}, \mathbf{p}) = \sqrt{\frac{m_N}{VE}} u(\mathbf{p}, s) e^{i\mathbf{x} \cdot \mathbf{p}}$, with $u(\mathbf{p}, s) = \sqrt{\frac{m_N + E}{2m_N}} \left(\frac{\chi_s}{\frac{\boldsymbol{\sigma} \cdot \mathbf{P}}{E + m_N} \chi_s} \right)$, and $\chi_{\frac{1}{2}} = \begin{pmatrix} 1 \\ 0 \end{pmatrix}$ and $\chi_{-\frac{1}{2}} = \begin{pmatrix} 0 \\ 1 \end{pmatrix}$.
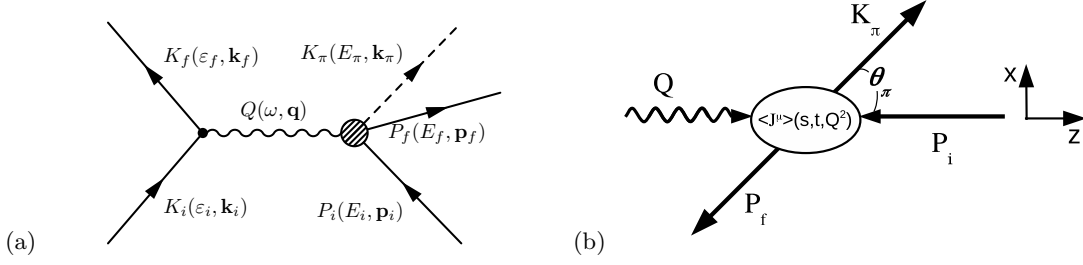
FIG. 25. (a) Feynman diagram representing the single-pion production off a free nucleon. (b) Representation of the hadronic subprocess in the center of momentum frame.

Notice that by choosing a reference frame in which $\mathbf{k}_f$ has no $\hat{\mathbf{y}}$ component, the cross sections in eqs. (125) and (127) will not depend on the azimuthal angle ϕ_f. Alternatively, if one chooses a reference frame in which $\mathbf{k}_\pi$ has no $\hat{\mathbf{y}}$ component, the cross sections will be independent on the azimuthal angle ϕ_π.

We will focus now on the description of the hadronic current. In the center of momentum system (CMS) of the hadronic subprocess, Fig. 25(b), the hadronic current depends on only three independent variables.

A usual choice for these are the Lorentz invariants Q^2, s and t, with

$$t = (Q - K_\pi)^2 = m_\pi^2 - |Q^2| - 2(\omega E_\pi - q k_\pi \cos\theta_\pi)\,, \tag{129}$$

where

$$\omega = \frac{s - m_N^2 - |Q^2|}{2W}\,, \quad E_\pi = \frac{s + m_\pi^2 - m_N^2}{2W}\,. \tag{130}$$

The maximum and minimum t values allowed by energy-momentum conservation correspond to the values $\cos\theta_\pi = -1$ and $\cos\theta_\pi = 1$. Thus, a possible strategy is to compute the hadronic current $J^\mu(Q^2, s, t)$ in the CMS and then bring it back to the lab frame where the experiments are performed. This would allow one to save important computational time when sophisticated models are employed in the calculation of the hadronic current.

b. Nucleon Resonances

SPP in the resonance region is dominated by the excitation and de-excitation of nucleon resonances. The properties of the resonances (spin, isospin, mass, decay width, branching ratios, etc.) lying in the region $W < 2$ GeV are, in general, known with great precision thanks to partial waves analyses of (mainly) elastic pion-nucleon scattering data [137]. Information on their electroweak properties, on the other hand, can be extracted from analysis of photon- and lepton-induced single-pion production data.

The Feynman diagram representing the electroweak resonant mechanism is illustrated in Fig. 26(a). The cross resonance term, which is sometimes considered to maintain crossing symmetry [138, 139], is shown in Fig. 26(b). In these diagrams we can identify three pieces: the electroweak vertex $\Gamma^{\mu\nu}_{QNR}$, the propagator of the resonance $S_{\mu\nu}$, and the hadronic vertex $\Gamma^{\mu}_{R\pi N}$. The amplitude for these diagrams is given by the contraction of them 'sandwiched' between the nucleon spinors. For example, for a spin-3/2 resonance, such as the Delta, one finds:

$$J^\mu_{(a)} \propto \bar{u}(\mathbf{p}_f, s_f)\, \Gamma^\alpha_{R\pi N}\, S_{\alpha\beta}\, \Gamma^{\beta\mu}_{QNR} u(\mathbf{p}_i, s_i)\,,$$
$$J^\mu_{(b)} \propto \bar{u}(\mathbf{p}_f, s_f)\, \bar{\Gamma}^{\alpha\mu}_{QNR}\, S_{\alpha\beta}\, \Gamma^\beta_{R\pi N} u(\mathbf{p}_i, s_i)\,, \tag{131}$$

with $\bar{\Gamma}^{\alpha\mu}_{QNR}(P_f, Q) \equiv \gamma^0 [\Gamma^{\alpha\mu}_{QNR}(P_f, -Q)]^\dagger \gamma^0$. The three pieces are described below for the case of a spin-3/2 resonance, and within a Rarita-Schwinger formalism [140].

1. *The electroweak vertex* is characterized by the properties of the resonance (spin, isospin, and parity) and the electroweak Q^2-dependent form factors. It is parametrized by [141]:

$$\Gamma^{\mu\nu}_{QNR} = \left(\Gamma^{\mu\nu}_{QNR,V} + \Gamma^{\mu\nu}_{QNR,A}\right)\widetilde{\gamma}^5\,, \tag{132}$$

with $\widetilde{\gamma}^5 = \mathbb{1}$ for even parity resonances, and $\widetilde{\gamma}^5 = \gamma^5$ for odd ones. The vector contribution is

$$\Gamma^{\mu\nu}_{QNR,V} = \left[\frac{C_3^V}{m_N}(g^{\mu\nu}\slashed{Q} - Q^\mu\gamma^\nu) + \frac{C_4^V}{m_N^2}(g^{\mu\nu}Q \cdot K_R - Q^\mu K_R^\nu) + \frac{C_5^V}{m_N^2}(g^{\mu\nu}Q \cdot P - Q^\mu P^\nu) + C_6^V\, g^{\mu\nu}\right]\gamma^5\,, \tag{133}$$

and the axial one is

$$\Gamma^{\mu\nu}_{QNR,A} = \frac{C_3^A}{m_N}(g^{\mu\nu}\not{Q} - Q^\mu\gamma^\nu) + \frac{C_4^A}{m_N^2}(g^{\mu\nu}Q\cdot K_R - Q^\mu K_R^\nu) + C_5^A g^{\mu\nu} + \frac{C_6^A}{m_N^2}Q^\mu Q^\nu \,. \tag{134}$$

K_R^μ stands for $K_s^\mu = P^\mu + Q^\mu$ and $K_u^\mu = P^\mu - K_\pi^\mu$ for the direct and cross channels respectively. The resonance form factors $C_i^{V,A}$ account for the internal structure, whose dynamics is explored with a resolution Q^2.

The vector form factors can be extracted from helicity amplitude analyses of single-pion electro-production data [137, 142–144]. In the axial sector, however, the situation is quite different. While the couplings may be guided by the PCAC hypothesis (see e.g. Appendix C in Ref. [144]), the rather scarce experimental data does not allow to constrain the Q^2 dependence, which is usually taken as dipole shapes with sets of parameters inspired by the vector and QE cases.

2. *The propagator* is

$$S_{\alpha\beta} = \frac{-(\not{K}_R + m_R)}{K_R^2 - m_R^2 + im_R\Gamma_{\mathrm{width}}(W)}\left(g_{\alpha\beta} - \frac{1}{3}\gamma_\alpha\gamma_\beta - \frac{2}{3m_R^2}K_{R,\alpha}K_{R,\beta} - \frac{2}{3m_R}(\gamma_\alpha K_{R,\beta} - K_{R,\alpha}\gamma_\beta)\right), \tag{135}$$

with $\Gamma_{\mathrm{width}}(W)$ the resonance decay width (see for instance Ref. [144]).

3. The *decay vertex* is

$$\Gamma^\alpha_{R\pi N} = \frac{\sqrt{2}f_{\pi NR}}{m_\pi}K_\pi^\alpha\widetilde{\gamma}^5 \,, \tag{136}$$

with $f_{\pi NR}$ the strong coupling constant [144, 145].

In Ref. [146], it is proposed an alternative description of the $\Delta\pi N$ vertex that remove the 'unwanted' coupling to the spin-1/2 component of the delta propagator in eq. (135), some results comparing the two vertices were shown in Ref. [147].
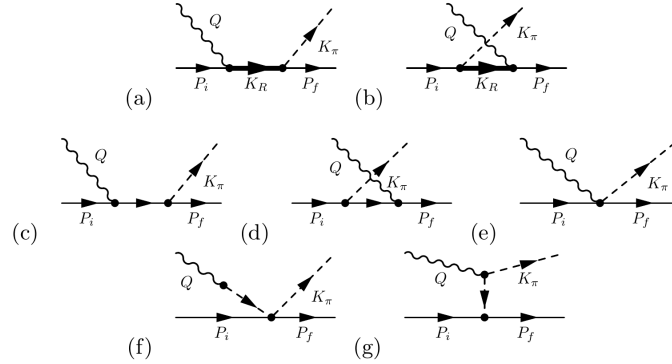

FIG. 26. Diagrams contributing to the SPP. Resonance contribution: Direct (a) and cross (b) channel terms. Background contributions: Direct (c) and cross (d) nucleon pole, contact term (e), pion pole (f), and pion-in-flight (g) term.

More details on nucleon resonances in neutrino-induced processes can be found in [97, 142, 143, 145, 148–150] and references therein.

c. Models

Resonance contributions alone are not sufficient to reproduce the experimentally observed photo-, electro- and neutrino-production data. Background contributions arising from different mechanisms are necessary, e.g. those in Fig. 26(c)-(g). This is especially evident at the pion threshold, far from the Delta peak, where this background is fully determined by chiral symmetry [151]. In Ref. [97], the leading order terms of a chiral perturbation theory Lagrangian (ChPT) for the π-nucleon system were computed [7], the diagrams contributing are shown in Fig. 26(c)-(g), while the expressions for their amplitudes can be found in [97, 145, 154, 155].

---

[7] Recently, in Refs. [152, 153] it has been presented a study on the weak pion production in ChPT up to next-to-next-to-leading order, using pions, nucleons, and Delta degrees of freedom.

Strictly speaking, the applicability of the background model [97] is limited to the pion production threshold, however, it has been shown that the incorporation of form factors and the Delta terms, Fig. 26(a) and (b), results in an effective model that provides a reasonably good agreement with photon-, electron-, and neutrino-induced SPP data in the region $W < 1.4$ GeV (see [97, 148, 154, 155] and references therein). This approach has been employed by different groups [145, 150, 154–157] in the description of neutrino-induced SPP. Its strength lies in its relative simplicity and that it is easily exportable to different nuclear frameworks.

To summarize the different models for SPP in the resonance region, that have been applied to electron and neutrino interactions, we use the classification given in Refs. [136, 158]. The first kind of models are those that include only resonance amplitudes, e.g. Ref. [142]. Models of the second kind combine resonances and background contributions [97, 144, 156, 159–161]. First and second kind, they both have in common that do not respect the unitarity condition of the amplitude. In the third kind we have the dynamical coupled-channels (DCC) model [158, 162–164], which in words of the authors [136] is an extension of the Sato and Lee (SL) model [165, 166]. The DCC model goes a few steps further than the first and second kind: i) it accounts for the re-scattering between the hadrons, ii) it includes coupled channels that open for increasing energy transfer, such as ηN, $K\Lambda$, $K\Sigma$ and $\pi\pi N$, and iii) the unitarity condition is fulfilled by construction. Similar degree of sophistication is achieved by the MAID unitary isobar model [167], but unfortunately, to our knowledge, this has not been consistently extended to neutrino-induced reactions yet.

It is worth mentioning that unitarity was partially restored in the model of Ref. [97] by incorporating the relative phases between the background diagrams and the dominant partial wave of the Delta pole [168]. On top of that, in Ref. [169] an additional contact term was added, aiming at improving the description of the $\nu_\mu n \to \mu^- n\pi$ channel and, at the same time, removing spurious spin-1/2 contributions in the Delta diagrams. Recently, in Ref. [170], this model, the DCC and the SL models were compared for a variety of reaction channels and kinematical scenarios. The authors concluded that, in the region $W < 1.4$ GeV, the simplest model [169] is able to reproduce the bulk results from the other more sophisticated ones.

It should be stressed that, for the axial sector, all models rely, in one way or another, on the neutrino-deuterium and neutrino-hydrogen pion-production data from the old bubble chamber BNL and ANL experiments [171–173]. On top of poor statistics and large systematic errors, the interpretation of these data has the additional challenge of describing the reaction on a deuterium target [174, 175]. Therefore, it is clear that new data on neutrino-hydrogen SPP would be of great value to move forward on a firmer basis.

d.   SPP in the high-W region

All the models mentioned describe the amplitude using lowest order interaction terms. For increasing W, higher-order contributions are needed, and hence, the predictions of these low-energy models (LEM) beyond $W = 1.4 - 1.5$ GeV should be taken with care. The DCC model can provide reliable predictions for somewhat larger invariant masses ($W \lesssim 2$ GeV) thanks to the incorporation of the relevant resonances up to $W \approx 2$ GeV along with the unitarization of the amplitude.

The procedure of adding higher order contributions soon becomes unfeasible. Regge phenomenology [176] is an alternative approach that provides the correct s-dependence of the hadronic amplitude in the high-s small-$|t|$ limit. The method, first proposed in [177] and further developed in [178], boils down to replacing the t-channels meson-exchange diagrams by the corresponding Regge amplitudes, which include an entire family of hadrons. In the context of [178], the s- and u-channel Born diagrams are kept in order to maintain CVC. As mentioned, Regge phenomenology only provides the s-dependence of the amplitude, but not the t- or Q^2-dependence. The t-dependence of the Regge amplitude is determined by the background terms of the LEM. The idea behind this is that the physical region of the reaction is not too far from the nearest pole of the Regge trajectory [176, 179]. This Regge-based t-channel approach [178] compares well to photoproduction and low-Q^2 electroproduction data, but it fails to reproduce the higher Q^2 data and the transverse component of the electroproduction cross section. To remedy this, in Ref. [180], this Regge-based model was supplemented with hadronic form factors, that are included in the s- and u-channel Born terms, and effectively account for the contributions of nucleon resonances in the high-Q^2 sector.

An extension to neutrino-induced reactions of the models of Refs. [178, 180] was recently developed in [145]. The model presented in Ref. [145] consists in a low-energy model (LEM) and a high-energy model (HEM) that are combined by a smooth W-dependent transition function. This results in a *hybrid model* that can be safely applied over a large W region. In particular, the LEM is built up from the coherent sum of background terms [97] and the s- and u-channel diagrams for the $P_{33}(1232)$ (Delta), D_{13} (1520), S_{11} (1535) and P_{11} (1440) resonances. The parametrization of the Olsson phases from Ref. [3], as well as the corresponding Delta form factors, were used. The HEM is obtained by Reggeizing the background terms [178] and introducing hadronic form factors [180, 181]. This HEM is compared with the LEM and with exclusive $p(e, e'\pi^+)n$ data in Fig. 27. The results show that the LEM clearly overshoots the data while the HEM provides a better description of them. Finally, the s- and u-channel resonance diagrams are regularized by using phenomenological cut-off form factors, whose role is just to eliminate their contributions far from the resonance peak $W \approx m_R$. More details can be found in [145].
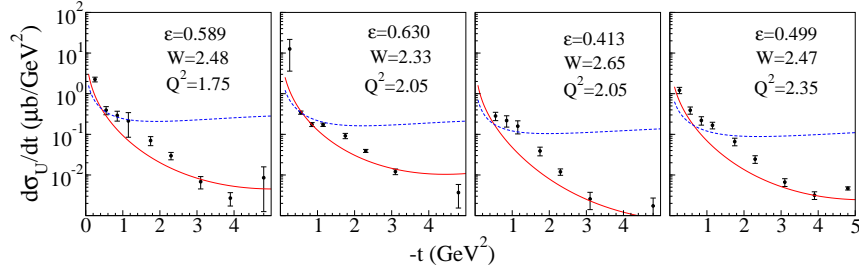
FIG. 27. Exclusive $p(e, e'\pi^+)n$ differential cross section ($d\sigma_U/dt = d\sigma_T/dt + \varepsilon d\sigma_L/dt$). The low-energy model (dashed line) overshoots the data, the high-energy model (solid line) reproduces its trend better. Data are from [182]. Figure is adapted from Ref. [145].

Event generators, such as NuWro [183] and GiBUU [184, 185], use DIS-based formalisms [186, 187] and PYTHIA hadronization routines [188] to describe neutrino-induced SPP in the high energy region ($W > 1.5 - 2$ GeV). The transition from the resonance region to the high-W regime is done by a transition function that smoothly, for increasing W values, switches on (off) the high-(low-)energy components of the model[8]. The validity of these DIS-based approaches is not clear at small Q^2, where it concentrates most of the strength of SPP [180]. This could be tested with the wide collection of electron-nucleon exclusive SPP data in the high-W region [182, 189–198].

e. Some results

In Fig. 28 we show inclusive electron-proton scattering cross sections for three different energies and scattering angles. The curves labelled as "LEM w/o ff" and "LEM w/ ff" correspond to the LEM without and with these resonance form factors, respectively. In both cases the LEM background [97] is used. The model labelled as "Hybrid" includes the resonance form factors and the transition to the Regge-based model [145]. The theoretical predictions include only the single-pion production channel, therefore, they should underestimate the inclusive data. By construction, the three models provide essentially the same results for $W < 1.3$ GeV. The need of cut-off resonance form factors and a high-energy model becomes evident if one moves towards higher W.
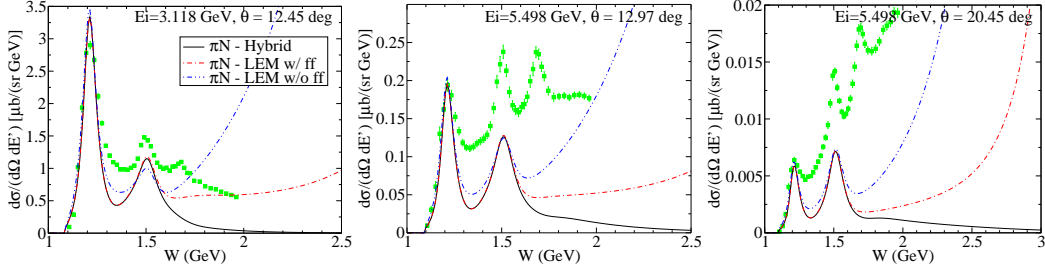

FIG. 28. Inclusive electron-proton scattering cross sections data [199] are compared with the SPP results of the low-energy (LEM) model (with and without resonance form factors) and the hybrid model of Ref. [145].

The predictions of the hybrid and DCC model [158] for SPP are shown in Fig. 29, for the same process and kinematics as in Fig. 28. The inclusive DCC predictions, which include other reaction channels such as two-pion production, is also shown. Up to the Delta peak, the DCC and hybrid models, and the data are comparable. Above the Delta peak, it is evident that the basic ingredients in the hybrid model are not enough to reproduce the strength of the SPP channel predicted by the DCC model. In particular, the hybrid model underpredicts the 'dip' between the Delta peak and the second resonance region. This may be related with the lack of other processes, such as ρ- and ω-exchanged contributions, the lack of pion-nucleon re-scattering, and the use of too strong cut-off resonance form factors. The third resonance region (third peak in the spectra) is also underpredicted by the hybrid model. This could be improved by including the relevant resonances in that region.

Finally, in Fig. 30 we compare the ANL and BNL data for CC neutrino-induced SPP with the low energy and hybrid models. In the region $E_\nu > 2$ GeV the differences between the three models are important. Since the predictions of

---

[8] The results of the hybrid model and NuWro for neutrino-induced SPP on the nucleon were compared in Ref. [145].
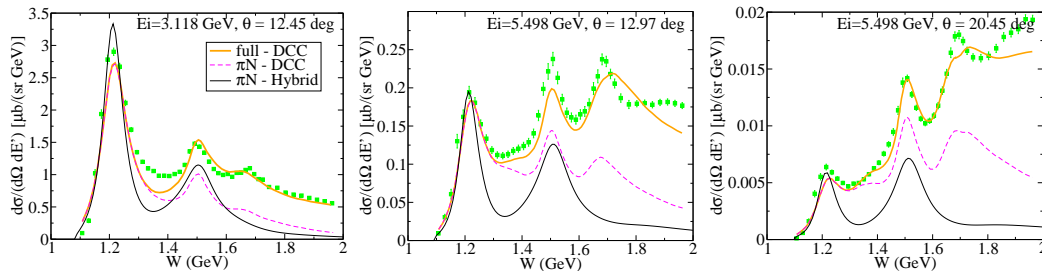
FIG. 29. Inclusive electron-proton scattering cross sections data [199] are compared with the SPP results from the DCC and Hybrid models. The inclusive DCC results (full-DCC) are also shown. The results of the DCC model have been taken from Ref. [158].

the LEMs cannot be considered realistic in this region, these results point to the need of a HEM. Also, the apparent agreement of the LEMs with data in the region $E_\nu > 1 - 1.5$ GeV should be interpreted with care.
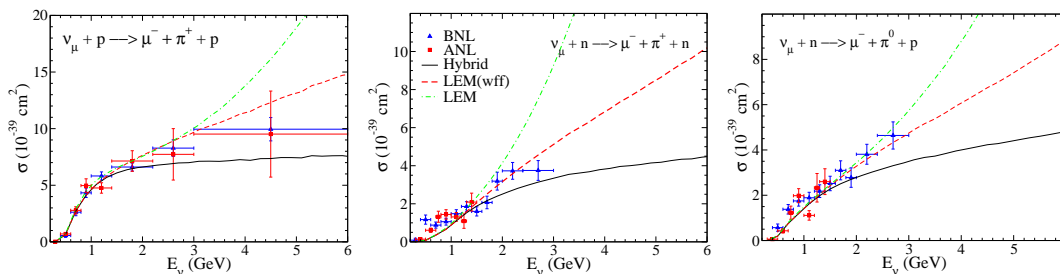

FIG. 30. Total cross sections for CC neutrino-induced SPP. The recent analysis [200] of the ANL and BNL data [171, 173] is compared with the low-energy and hybrid models (data without cuts in the invariant mass). Deuteron effects are not considered. The figure was adapted from [145].

B. Nuclear framework

The elementary reaction described above for SPP can be incorporated in a nuclear framework using the impulse approximation, i.e., considering that the electroweak boson interacts with only one nucleon in the nucleus. The simplest choice is the global relativistic Fermi gas model which, in spite of its simplicity, is still employed by MC generators in the analyses of data [122–124, 126, 127, 130]. The global RFG is a fully relativistic model, it respects the fundamental symmetries of a relativistic quantum field theory and it is able to capture the gross features of the nuclear response. Though, it is quite far from the level of precision required in the new era of the neutrino-oscillation programme [3]. The local Fermi gas (lFG) or its relativistic version (lRFG) are also widespread [148, 154, 201–204]. To achieve a more realistic description of the nuclear dynamics, different groups add different ingredients on top of the 'bare' local Fermi gas (see [4, 135] for a review). The factorization approach has also been used for neutrino-induced pion production [62, 205]. This factorization of the elementary vertex and the nuclear dynamics, the latter contained in the nuclear spectral function, makes it very appealing to be used in MC event generators. Finally, mean-field based models are the state of the art regarding the description of the nuclear dynamics within a quantum mechanical framework that allows for the treatment of inclusive and exclusive processes. In what follows we review the lepton-induced SPP on the nucleus in the context of a the relativistic mean-field model [133, 134, 147, 206, 207].

a. What Mean-Field models can offer to the neutrino interaction community

Mean-field models are able to capture a good part of the nuclear dynamics by describing the ground state nucleus as a set of independent-particle nucleon wave functions that are solutions of the mean-field equations. In previous sections we already discussed these models applied to electron and neutrino scattering reactions. Here we simply summarize the basic points of interest for the discussion that follows.

As known, the case of inclusive processes can be efficiently modelled by describing the final states as scattering solutions of the corresponding wave equation: the Dirac or Schrödinger equation for the nucleons and the Klein-

Gordon equation for the pions. Since the flux has to be conserved, one can use mean-field potentials with only real part [33, 34, 207–211] or full complex optical potentials, in which the flux lost (transferred to inelastic channels) due to the imaginary term is recovered by a summation over those channels, as done in the Relativistic Green Function (RGF) model [58, 209, 212]. On the contrary, in the exclusive case one needs to account for the flux moved to the inelastic channels (absorption, multi-particle emission, charge exchange, etc.). This can be accounted for by using phenomenological complex optical potentials [36, 37] (see discussion in Sect.III C) fitted to elastic nucleon-nucleus scattering [213, 214] or elastic pion-nucleus scattering [215] data, and correcting the results with spectroscopic factors.

In neutrino experiments, however, fully exclusive conditions are never satisfied: the neutrino energy is unknown and the limited acceptances of the detectors make it impossible to detect the complete final state. Therefore, Monte Carlo (MC) neutrino event generators have to deal with inclusive and semi-inclusive events and, by combining the available experimental information with the nuclear theory, reconstruct the neutrino energy for every selected event. Modelling all possible semi-inclusive scenarios in a consistent way means to solve an extremely complicated many-body coupled-channel problem. A situation still far from being resolved. In spite of that, one can try to minimize the systematic errors that propagate to oscillation analyses by improving the theoretical nuclear models implemented in the MC's.

In MC event generators there are two clearly separated steps: i) the elementary vertex, and ii) the propagation in the nuclear medium of the created hadrons, using a classical cascade model that generates the complete final state. Due to this factorization, 'elementary vertex × hadron propagation', the inclusive cross section will not be affected by the cascade process. Therefore, the primary model (the one that describes the elementary vertex) should be able to provide a good inclusive response. In summary, the primary model puts 100% of the strength in the elastic channel, then the cascade takes care of splitting the flux into the different inelastic channels. It is, therefore, preferable to use primary models that provide information not only on the final lepton (inclusive models) but also on the hadrons, so that they can be used as the 'seed' for the cascade in a more consistent way. The mean-field models discussed here can satisfy those requirement: full hadronic information and good inclusive results.

b. Cross section

Given the momenta $\mathbf{k}_i$ and $\mathbf{p}_A$ of the incoming lepton and target nucleus, the SPP scattering process is completely determined by 9 independent variables [216]. The nucleon wave functions are computed in the center of mass of the target nucleus, therefore, it is natural to work in the laboratory reference frame where the target nucleus is at rest ($\mathbf{p}_A = 0$). Hence, we use the laboratory variables ε_f, θ_f, ϕ_f, E_π, θ_π, ϕ_π, θ_N, ϕ_N, and the missing energy E_m, as independent variables (see Fig. 31). In terms of these, the differential cross section for the process in Fig. 31 reads [216]

$$\frac{d^9\sigma}{d\varepsilon_f \Omega_f dE_\pi d\Omega_\pi d\Omega_N dE_m} = \frac{\mathcal{R}_X}{(2\pi)^8} \frac{k_f p_N E_N E_\pi k_\pi}{2\varepsilon_i f_{rec}} \eta_{\mu\nu} h_{(\kappa)}^{\mu\nu} \rho_B(E_m). \tag{137}$$

The function f_{rec} accounts for the recoil of the residual nucleus and is given by [9]

$$f_{rec} = \left| 1 + \frac{E_N}{E_B} \left(1 + \frac{\mathbf{p}_N \cdot (\mathbf{k}_\pi - \mathbf{q})}{p_N^2} \right) \right|. \tag{138}$$

The energy of the outgoing nucleon E_N and the residual nucleus E_B are obtained from the independent variables [216]. The factor $\mathcal{R}_X$ was defined in Eq. 122 and the leptonic tensor $\eta_{\mu\nu}$ in Sect. II. The hadronic tensor for one nucleon knock out from a κ shell is given by

$$h_{(\kappa)}^{\mu\nu} = \frac{1}{2j+1} \sum_{m_j} \sum_{s_N} (J^\mu)^\dagger J^\nu, \tag{139}$$

where $\sum_{s_N=\pm1/2}$ is the sum over the spin projections of the knockout nucleon and $\frac{1}{2j+1}\sum_{m_j}$ is the average over the bound nucleons of a κ shell, being j the total angular momentum and m_j its third component.

The fact that the residual nucleus may be in an excited state is introduced by the function $\rho_B(E_m)$, that represents the density of final states for the residual nucleus. Its mass, M_B, is determined from the energy-conservation relation $M_B = M_A + E_m - m_N$. Within a pure shell model

$$\rho_B(E_m) = \sum_\kappa \delta(E_m - E_m^\kappa), \tag{140}$$

where E_m^κ is a fixed value for each shell.

---

[9] We note that there is a typo in the expression of f_{rec} given in Ref. [134].

c. Hadron current

In this framework, the most general hadronic current (for given κ, m_j and s_N) in momentum space reads

$$J^\mu = \frac{1}{(2\pi)^{3/2}} \int d\mathbf{p}'_N \int d\mathbf{p}\, \overline{\psi}^{s_N}(\mathbf{p}'_N, \mathbf{p}_N)\phi^*(\mathbf{k}'_\pi, \mathbf{k}_\pi)\, \mathcal{O}^\mu_{1\pi}(Q, P, K'_\pi, P'_N)\psi^{m_j}_\kappa(\mathbf{p}), \tag{141}$$

where $K'_\pi = Q + P - P'_N$. $\psi^{m_j}_\kappa(\mathbf{p})$ is the Dirac spinor of the bound nucleon (see Ref. [42] for details) and P represents its four momentum. $\psi^{s_N}(\mathbf{p}'_N, \mathbf{p}_N)$ and $\phi(\mathbf{k}'_\pi, \mathbf{k}_\pi)$ represent the wave functions of the final nucleon and pion (see Fig. 31). [10] In deriving Eqs. (137) and (141), it has been considered that all the particles have well defined energy in all steps of the process, so that the energy of the bound nucleon E, which is needed to build the operator $\mathcal{O}^\mu_{1\pi}$, can be determined by energy conservation $\omega + E = E_N + E_\pi$. Note that the transition operator $\mathcal{O}^\mu_{1\pi}(Q, P, K'_\pi, P'_N)$ has to be evaluated for every $\mathbf{p}$ and $\mathbf{p}'_N$. All this, together with the large phase space for this process (4 particles in the final state), represents a non trivial problem from the computational point of view.
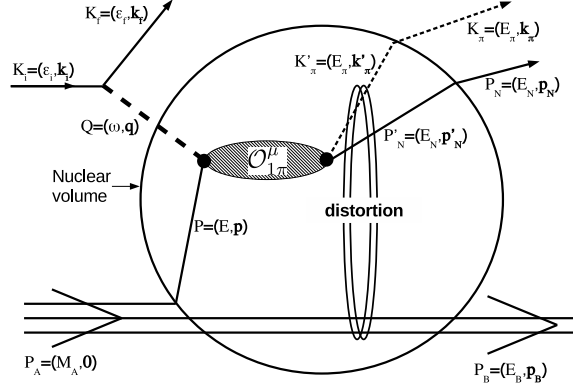

FIG. 31. Representation of the electroweak SPP on a nucleus within the impulse approximation. An incoming lepton K_i scatters on a nucleus P_A. A single boson Q is exchanged. The final state consists in a scattered lepton K_f, the residual system P_B, and a knockout nucleon and pion with asymptotic four momentum P_N and K_π, respectively. Inside the nucleus the momenta of the initial and final nucleons ($\mathbf{p}$ and $\mathbf{p}'_N$) and the pion ($\mathbf{k}'_\pi$) are given by probability distributions. See text for details.

In what follows we describe some approximations that simplify the problem and have allowed us to obtain numerical results that can be compared with cross section data:

1. Using the asymptotic values for the four momenta of the final nucleon and pion in the operator $\mathcal{O}^\mu_{1\pi}$, i.e.:

$$\mathcal{O}^\mu_{1\pi}(Q, P, K'_\pi, P'_N) \longrightarrow \mathcal{O}^\mu_{1\pi}(Q, P, K_\pi, P_N) \text{ with } P = P_N + K_\pi - Q. \tag{142}$$

In this way, $\mathcal{O}^\mu_{1\pi}$ can be evaluated out of the integrals in Eq. (141).

2. Describing the pion as a plane wave. In this case, Eq. (141) reduces to:

$$J^\mu = \frac{1}{\sqrt{2E_\pi}} \int d\mathbf{p}\, \overline{\psi}^{s_N}(\mathbf{p}'_N, \mathbf{p}_N)\mathcal{O}^\mu_{1\pi}(Q, P, K_\pi, P'_N)\psi^{m_j}_\kappa(\mathbf{p}), \tag{143}$$

with $P'_N = Q + P - K_\pi$. Notice that if the approximation (142) is not employed, the operator should be calculated for every $\mathbf{p}$ value.

3. Describing the pion and the outgoing nucleon as plane waves. Thus, Eq. (143) reads:

$$J^\mu = (2\pi)^{\frac{3}{2}} \sqrt{\frac{m_N}{2E_\pi E_N}}\, \overline{u}(\mathbf{p}_N, s_N)\mathcal{O}^\mu_{1\pi}(Q, P, K_\pi, P_N)\,\psi^{m_j}_\kappa(\mathbf{p}), \tag{144}$$

with $P = P_N + K_\pi - Q$. In this case, the momenta of all particles are well defined, so that the approximation (142) does not apply.

---

[10] The definition of the wave function including distortion effects can be found, for example, in Refs. [36, 40, 217] for the nucleon, and in Ref. [215] for the pion.

4. Describing the initial and final nucleon, and the pion as plane waves. The hadronic current (144) results

$$J^\mu = (2\pi)^3 \delta^3(\mathbf{p}_N + \mathbf{k}_\pi - \mathbf{q} - \mathbf{p}) \sqrt{\frac{m_N^2}{2E_\pi E_N E}} \, \overline{u}(\mathbf{p}_N, s_N) \mathcal{O}_{1\pi}^\mu(Q, P, K_\pi, P_N) \, u(\mathbf{p}, s) \,, \tag{145}$$

the replacement $\frac{1}{2j+1} \sum_{m_j} \to \frac{1}{2} \sum_s$ in Eq. (139) is assumed. This is the hadronic current in the RFG model. From Eqs. (137) and (145), it is straightforward to obtain numerical results within the RFG; additionally, the free nucleon case can be recovered as the limit $p_F \to 0$, with p_F the Fermi momentum.

The impact of the approximations described above will depend on the particular case under study, but in general we can say that the more exclusive conditions (smaller phase space) and the further we are from the maximum of the distributions, the greater the dependence on these nuclear effects. In Fig. 32(a), we show the Q^2 differential cross section (per nucleon) for the process $\nu_\mu + {}^{12}C \to \mu^- + {}^{11}B + p + \pi^+$ computed with three different approaches: i) considering a free proton target, ii) the RFG, and iii) the RPWIA. This comparison allows us to estimate the effect of Fermi motion and binding energy as well as the impact of using a distribution instead of a Dirac delta in the initial state (compare Eqs. (144) and (145)). One observes that the free-nucleon model clearly departs from the RPWIA and RFG results, while the latter are almost indistinguishable. As explained in the original paper [147], this is the case for sufficiently high energy and momentum transfer and for a RFG model with an appropriate binding-energy correction.
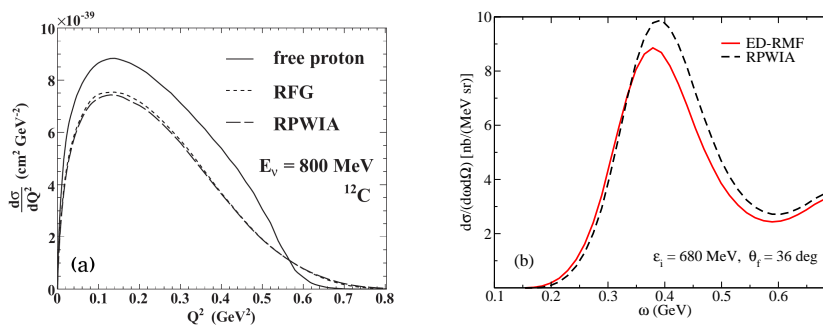

FIG. 32. (a) Q^2 differential cross section for the process $\nu_\mu + {}^{12}C \to \mu^- + {}^{11}B + p + \pi^+$ computed with RPWIA, RFG and considering a free proton target; figure taken from Ref. [147]. (b) Electron-induced SPP double differential cross section evaluated under the approximations described in Eqs. 143 (ED-RMF) and 144 (RPWIA).

In Fig. 32(b) we show the inclusive ${}^{12}C(e,e')$ electron scattering cross section computed with two approaches based on Eqs. (143) and (144), i.e.: the pion is described as a plane wave and the initial nucleon is computed within the RMF model, the final nucleon is i) a plane wave (Eq. (144), labelled as RPWIA), or ii) it is a continuum relativistic distorted wave (Eq. (143), labelled as ED-RMF). The results show that in spite of the large phase space that contribute (integrals over the nucleon and pion variables have been performed), the nuclear effects, such as Pauli blocking and distortion, that are incorporated in the ED-RMF model and not in the RPWIA, remain quite important (see Ref. [207] for further details).

The approximation defined in Eq. (142) was considered in the ED-RMF calculations shown in Fig. 32(b), and in those of Ref. [207]. The impact of this approximation has been studied in the past for different reactions, in Ref. [218] for pion photoproduction and in Ref. [219] for coherent pion production. Its effect in lepton-induced SPP within the RMF framework will be the subject of future work.

Finally, describing the pion as a plane wave (Eq. 143) is clearly an oversimplification of the problem, especially if we aim at describing semi-inclusive results in which the pion is detected. This is further discussed in Sect. V C.

d. In-medium modification of the Delta resonance

The properties of the resonances are modified in the nuclear medium. Due to the dominant role of the Delta resonance, the in-medium modification of its decay width is one of the main nuclear effects in neutrino-induced SPP [220, 221].

The procedure developed in Refs. [222–224] consists in modifying the Delta decay width by the complex part of the Delta self-energy calculated in the nuclear medium, as well as accounting for Pauli blocking that reduces the phase space available for the Delta to decay. It has been discussed in many references [148, 154, 204, 225, 226], so we do not repeat it here. The uncertainties and inconsistencies of using this method, which was developed within a Fermi gas

model, in the framework of our relativistic mean-field model were discussed in Ref. [133, 134]. Its effect in the cross section is shown in Fig. 33 as a red band, that represents the uncertainty attached to this nuclear effect.

Other studies on the medium modification of the Delta width have been presented in Refs. [227–231].

C.   Pion final-state interactions

In Refs. [133, 134] theoretical SPP cross sections were compared with different sets of 1π-detected data reported by the MiniBooNE [122–124], MINERvA [125–128] and T2K [130] experiments. Due to the semi-inclusive nature of these experiments, a meaningful comparison with these data requires to account for the pion final-state interactions. The pions produced in the primary vertex may suffer elastic rescattering, charge exchange, be absorbed, create new pions, etc. Indeed, the pion that reaches the detector may not be the one produced in the primary vertex but another one originated in a secondary interaction.

In Fig. 33, we present a selection of the results presented in Refs. [133, 134]. On the one hand, we show the predictions of the hybrid-RPWIA model. In this approach, the hybrid model described in Sect. V A 0 d was used for the current operator, and the RPWIA was used for the nuclear part (Eq. 143). Thus, final-state interactions (FSI) are neglected. On the other hand, we show the results of the MC neutrino event generator NuWro [232]. In NuWro the elementary vertex is described in a somewhat simpler way: the Delta resonance and a background, which is an extrapolation of the DIS contribution to the low-W region [183]. On the contrary, NuWro accounts for FSI using a sophisticated cascade model [232, 233] (see Ref. [234] for a recent study in which the model is updated and benchmarked), so it gives us a quantitative estimate of the effect of FSI on the pion distributions. In the calculations shown in Fig. 33, red bands correspond to the Hybrid-RPWIA with (lower line) and without (upper line) medium modification of the Delta width. The blue-solid lines are NuWro results using the same definition of the signal as in the experiment. The blue-dashed lines are NuWro but without FSI. The orange dash-dotted lines are NuWro results without FSI and selecting those events in which only one pion and one nucleon exit the nucleus. These latter results correspond to the elementary SPP process as predicted by NuWro, and they could be compared with the hybrid-RPWIA results.
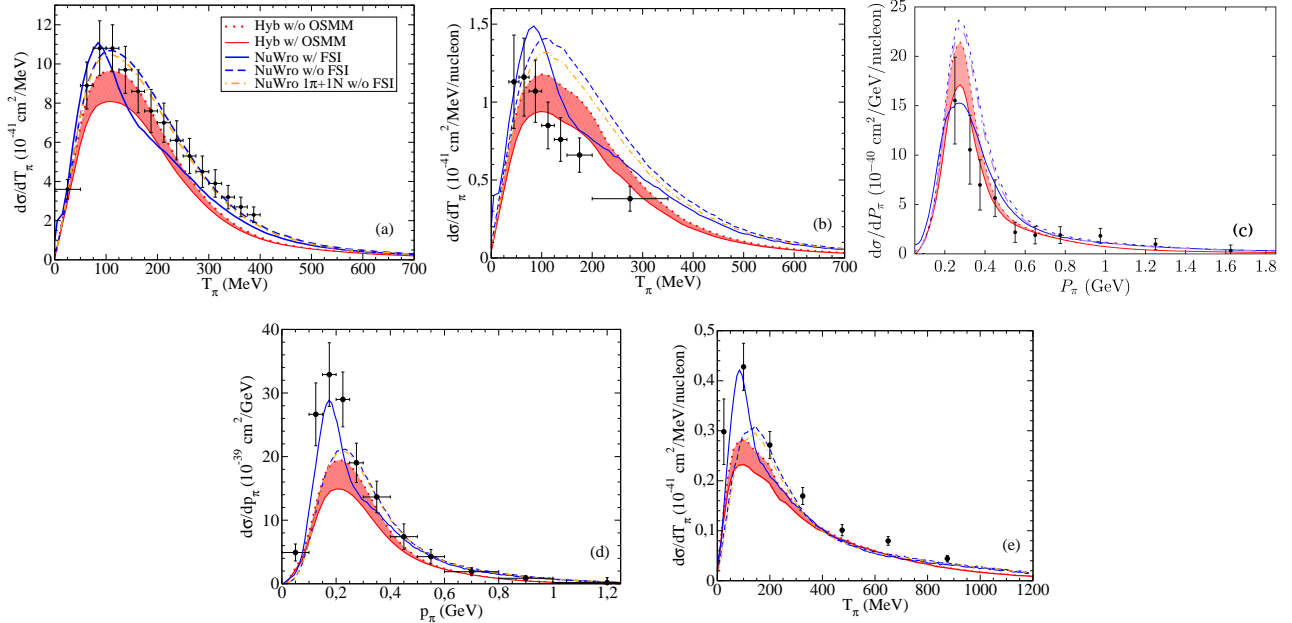

FIG. 33. CC ν_μ-induced one pion production on the nucleus. Single differential cross sections are represented as a function of the kinetic energy T_π or the momentum p_π of the pion. Panels (a), (b) and (c): MiniBooNE [123], MINERvA [126, 127] and T2K [130] $1\pi^+$ production on CH_2, CH and H_2O, respectively. Panels (d) and (e): MiniBooNE [124] and MINERvA [125] $1\pi^0$ production on CH_2 and CH, respectively. Figures adapted from Refs. [133, 134].

Finally, the effect of the pion FSI in Fig. 33 can be understood attending to the mechanisms that are implemented in the cascade, i.e.: secondary interactions slow down the pions, which shift the strength towards lower T_π regions; pion absorption reduces the total strength; charge-exchange reactions moves flux from one channel to another, but since the $1\pi^+$ channel is dominant in CC ν_μ-induced pion production, the net effect is to reduce (increase) the magnitude

of the $1\pi^+$ ($1\pi^0$) distributions.

In Refs. [131, 132, 148] other theoretical predictions were compared with MiniBooNE, MINERvA and/or T2K pion-detected data.

VI. Higher Inelastic, DIS and its implementation in the scaling formalism

A. Higher lying resonance contributions and general models

Beyond the excitation of $\Delta(1232)$ resonance, other higher lying resonances ($W > 1.4$ GeV) have to be taken into account in a description based on resonance production followed by their subsequent decays, either on specific channels (πN, $\pi\pi N$, ηN, KY...), or summing over all of them for inclusive (e, e') or (ν_l, l) reactions at higher energy transfers. This region of invariant masses $W > 1.4$ GeV is usually called the second resonance region [235]. The most relevant and theoretically studied resonances in this region are the three isospin $1/2$ (N^*) states known as $P_{11}(1440)$, $D_{13}(1520)$ and $S_{11}(1535)$, where the nomenclature $L_{2I\,2J}$ is used to classify them, with I, J and L being the isospin, spin and partial wave of the resonances, respectively.

Most of the information about the electromagnetic and weak resonance transition vector form factors comes from the studies of pion electro and photo-production data off nucleons by including these resonances in the analyses [236–239]. The electromagnetic nucleon-to-resonance form factors can be usually obtained from the helicity amplitudes, in the same fashion as the MAID model [240]. The corresponding weak vector transition form factors can then be related to the electromagnetic ones by assuming that the weak vector charged current belongs to the same triplet of current operators as the isovector component of the electromagnetic current (for a very detailed description on how to work out this, please see the appendices of Ref. [144]). Normally, the transition axial form factors are much more difficult to determine because of the lack of guidance from the electromagnetic interactions. The usual trick is to use PCAC to relate two of the axial form factors, and the coupling of one of them at $q^2 = 0$ can be determined from the partial decay width of the particular resonance into the πN channel [235, 241]. This is done in the same fashion as when we relate the nucleon pseudo-scalar and axial form factors, while the axial coupling is obtained by assuming pion-pole dominance and by relating it to the strong πNN coupling through the Goldberger-Treiman relation.

The aforementioned procedure is general and can be applied to the neutrino-production of many resonances in the range of invariant masses between 1 and 2 GeV. It has been applied, for instance, in Refs. [144, 235, 242, 243] to the study of electron and neutrino-nucleus scattering in the resonance region, including the Δ region as well. For more recent works where the inclusion of higher lying baryon resonances is taken into account for the study of single pion production driven by weak and neutral currents, the reader is referred to Ref. [244]. Other works where the excitation of the $N^*(1535)$ and $N^*(1650)$ resonances is taken into account for the calculation of η-meson production cross sections off nucleons can be found in [245, 246].

One of the most relevant works in the analysis of single pion neutrino-production is that of Rein and Sehgal [160]. They included all the relevant resonances below 2 GeV for the analysis of both charged and neutral current single pion production data by then. In this latter work, however, the helicity amplitudes are not phenomenologically obtained, but theoretically calculated within the relativistic harmonic oscillator quark model of Feynman, Kislinger and Ravndal [247]. The Rein-Sehgal model is widely used in some of the Monte Carlo event generators used for the analyses and simulations of single pion production events, namely GENIE, Neut and Nuance [248–252]. This model has been also extended to account for the final lepton mass and spin in lepton polarization studies in neutrino-nucleon scattering [253, 254].

It is also worth mentioning that some specific channels, such as the two pion production $\pi\pi N$ one, have been very scarcely studied from the experimental and theoretical side. In Ref. [143] it is shown that the inclusion of the Roper resonance, $N^*(1440)$, is relevant for this reaction channel near its production threshold.

Up to now we have only mentioned the excitation of non-strange resonances. However the weak charged current can induce strangeness-changing transitions $|\Delta S| = 1$ as well, although these are highly suppressed with respect to their strangeness-preserving $|\Delta S| = 0$ counterparts because the amplitudes for the latter are proportional to the cosine of the Cabibbo angle, $\cos\theta_c \sim 0.974$, while those for strangeness-changing are proportional to the sine of the same angle, which is much smaller, $\sin\theta_c \sim 0.226$. This kind of processes normally requires the inclusion of strange baryon resonance degrees of freedom, normally the $\Sigma^*(1385)$, which belongs to the same SU(3) multiplet as the $\Delta(1232)$. Some relevant and quite recent works studying the production of strange particles induced by electrons, neutrinos and anti-neutrinos, either through the strangeness-preserving or the strangeness-changing part of the weak charged current, some of them studying polarization observables and second-class currents effects, can be found in Refs. [255–263].

B. Inelastic contribution within the scaling formalism and the SuSAv2 approach

Within the scaling formalism, in Ref. [264], an extension of the RFG model to the inelastic region was carried out by allowing the reached final invariant masses W_X to be larger than in the QE case ($m_N + m_\pi \leq W_X \leq m_N + \omega - E_s$, with E_s the nucleon separation energy), and then performing an integration over all the allowed invariant masses with a "spectral function" (the inelastic RFG scaling function in terms of the inelastic scaling variable ψ_X - see Appendix A) accounting for the energy-momentum distribution of nucleons in the RFG description of the initial nuclear state. To apply this formalism it is necessary to resort to phenomenological parameterizations of the inelastic single-nucleon structure functions, extracted mainly from DIS $e - N$ scattering, but also incorporating resonances in the $W < 2$ GeV region [186, 265–267]. More recent and complete parameterizations of these inelastic single-nucleon structure functions extracted from inelastic electron-proton and electron-deuteron scattering experiments can be found in Refs. [268, 269].

This formalism has been also applied to the SuSAv2 approach to extend the description to the full inelastic regime, just replacing the RFG scaling functions by the QE SuSAv2 ones and considering the corresponding inelastic scaling variable (ψ_X) aforementioned. The inelastic nuclear response functions are thus defined as:

$$R_{inel}^K(\kappa, \tau) = \frac{\mathcal{N}}{\eta_F^3 \kappa} \xi_F \int_{\mu_X^{min}}^{\mu_X^{max}} d\mu_X \mu_X f^{model}(\psi_X') U^K .$$ (146)

Then, we can identify the inelastic scaling function which englobes all the nuclear dependence of the interaction, f^{model}, and employ the one arising from the specific model considered (RFG, SuSAv2, etc), in a similar way as done for the QE regime. The previous formalism allows for a complete description of the inelastic cross sections on lepton-nucleus interactions where the nuclear effects can be included by means of the inelastic RFG or SuSAv2 scaling functions (f^{model}). The procedure in the SuSAv2-inelastic approach is similar to that applied for the QE regime before, keeping the same functional form for the RMF and RPWIA scaling functions but using a different scaling variable (ψ_X') and a different q_0 transition parameter for the blending function introduced in Eq. (84). We make use of the Bosted and Christy parametrization for the single-nucleon inelastic structure functions [268, 269] which describes DIS, resonant and non-resonant regions, providing a good description of the resonant structures in (e, e') cross sections and covering a wide kinematic region. As shown in Fig. 34 and in [270], the use of other choices such as the Bodek-Ritchie [186, 265] parametrization and models based on Parton Distribution Functions (PDF)[11], such as GRV98 [272], leads to large discrepancies with (e, e') data. Although the phenomenological structure functions (F_1, F_2) employed in the SuSAv2-inelastic model were obtained via electromagnetic interactions, the extension to the weak sector is also possible under some assumptions. The description of the inelastic regime for weak interactions implies an additional structure function, F_3, related to the parity violating contribution associated to the $V - A$ interference. An accurate determination of this weak function is hard to achieve from neutrino experiments as well as from parity-violating electron scattering [273, 274] due to the large uncertainties associated to the cross section measurements. Nevertheless, as mentioned before, within the quark-parton model, it can be established a relationship among the electromagnetic and weak structure functions and between F_2 and F_3 [186, 265, 275]. This is based on the assumption that the corresponding structure functions W_i can be written in terms of quark $\mathcal{Q}$ and antiquark $\overline{\mathcal{Q}}$ distributions [276, 277]

$$F_2 = \nu W_2 = \mathcal{Q} + \overline{\mathcal{Q}} \quad ; \quad F_3 = x \nu W_3 = \mathcal{Q} - \overline{\mathcal{Q}} \quad \rightarrow \quad x \nu W_3 = \nu W_2 - 2\overline{\mathcal{Q}} .$$ (147)

For electron scattering, the isoscalar F_2 structure function of the nucleon, defined as the average of the proton and neutron structure functions, is given (at leading order in α_s and for three flavors) by

$$F_2^{eN} = \frac{1}{2} \left(F_2^{ep} + F_2^{en} \right) = \frac{5x}{18} \left(u + \overline{u} + d + \overline{d} \right) + \frac{x}{9} \left(s + \overline{s} \right) .$$ (148)

The quark distributions are defined to be those in the proton and the factors 5/18 and 1/9 arise from the squares of the quark charges. For neutrino scattering, the corresponding F_2 structure function is given by

$$F_2^{\nu N} = x(u + \overline{u} + d + \overline{d} + s + \overline{s}) ,$$ (149)

where quark charges are not considered. In the moderate and large-x region, where strange quarks are suppressed, the weak and electromagnetic F_2 structure functions approximately satisfy

$$F_2^{eN} \approx \frac{5x}{18} \left(u + \overline{u} + d + \overline{d} \right) \approx \frac{5}{18} F_2^{\nu N} .$$ (150)

---

[11] For a general discussion on electron and charged current or neutral current neutrino/antineutrino DIS off nucleons, the reader is referred to Ref [271].

Under this assumption, which has been analyzed in connection with experimental results [276, 278–280], one can readily obtain the weak structure functions from the existing parametrization of the electromagnetic structure functions and the antiquark distribution[12] . More specific details about the SuSAv2-inelastic model can be found in [270].
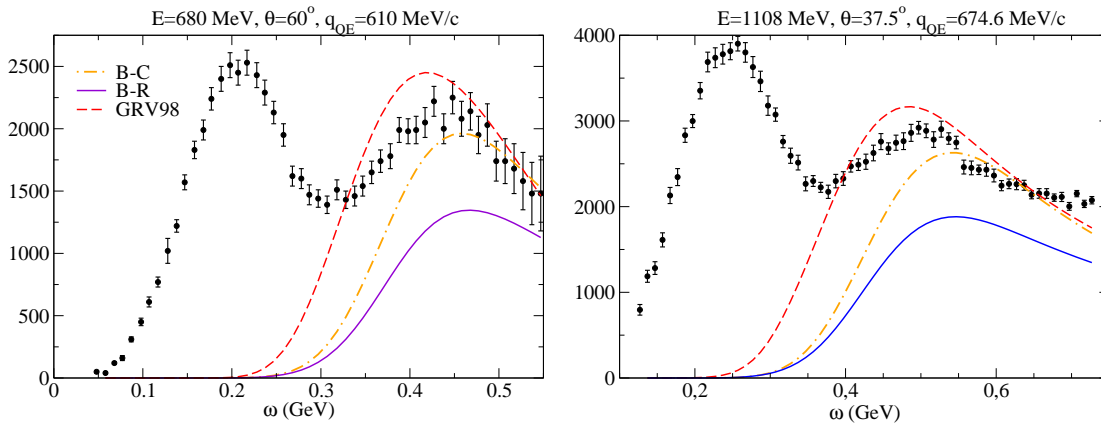

FIG. 34. Comparison of inclusive $^{12}C(e, e')$ double differential cross sections and predictions for the inelastic regime of the Bodek-Ritchie parametrization (solid lines), Bosted-Christy parametrization (dot-dashed lines) and GRV98 PDFs (dashed lines) at different kinematics (incident electron beam and scattering angle) in terms of the energy transferred to the nucleus (ω). Experimental data taken from [120, 281]. The y-axis represents $d^2\sigma/d\Omega/d\omega$ in nb/GeV/sr. The value of q at the QE peak (q_{QE}) is shown as reference.

In a different approach [118], the scaling and super-scaling properties of the non-QE experimental data have been analysed within the framework of several theoretical models. To this end, the QE contribution was subtracted from the inclusive (e, e') experimental data to obtain a non-QE cross section. The QE contribution was calculated by assuming a universal phenomenological longitudinal scaling function fitted in Refs. [18, 19] and assuming the QE transverse and longitudinal scaling functions to be equal ($f_L^{QE}(\psi_{QE}) = f_T^{QE}(\psi_{QE})$). The non-QE cross section so obtained was then translated into a non-QE scaling function, $f^{non-QE}(\psi_\Delta)$, by dividing by the single-hadron $N \to \Delta$ cross section, whose explicit expressions can be found in Refs. [21, 119]. The residual pseudo-data were mainly compared with two theoretical models: the first one was basically that of Ref. [264], already discussed in the previous paragraph, but with updated inelastic single-nucleon structure functions taken from [268, 269]; the other model used to analyze the data was that of Ref. [119], which is based on the assumption of the Δ dominance in the inelastic region, but taking into account the finite Δ width. One of the main conclusions of this work [118] is that, besides the importance of non-impulsive mechanisms (2p-2h, correlations...) to be incorporated consistently in any model, there were kinematics much better described by the inelastic model of Ref. [264] than by the Δ-dominance model of [119], thus indicating the importance of higher inelastic contributions beyond the Δ at those kinematics (mainly corresponding to larger incident electron energies and medium/large scattering angles, thus linked to higher momentum transfers as well).

VII.   The SuSAv2-MEC model

In Section III E a detailed description of the SuSAv2 model was given, that, as known, incorporates the predictions from the RMF theory and a transition to the RPWIA model at high values of the momentum transfer. This transition between the RMF and RPWIA regimes is governed by a blending function whose explicit expression was described in Secion III E (see also [51, 94] for details). In order to apply the SuSAv2 model not only to the QE regime but also to the full inelastic spectrum, it is required a good control of the transition parameters (q_0, ω_0) that determine the relative strength of the RMF and RPWIA responses, and how the transition between them evolves as the transfer momentum varies. Accordingly, the transition parameter, q_0, is expected to increase with q in such a way that the RMF contribution will be dominant at low kinematics whereas the RPWIA one starts to be relevant at higher energies. The particular procedure to determine the q_0-behavior with q is in accordance to the best fit to a large amount of (e, e') measurements on ^{12}C in a wide kinematical region, covering from low to high q-values (q: $239 - 3432$ MeV/c). For this analysis, ^{12}C is employed as reference target due to the ample variety of existing data for electron scattering

---

[12] The extension of the SuSAv2-inelastic model to the weak sector is under way.

as well as its relevance for neutrino oscillation experiments. The method applied to determine the RMF/RPWIA transition in the SuSAv2 model in both QE and inelastic regimes is based on a reduced-χ^2 analysis of the data sets (see [107] for details).

In this section, the so-called SuSAv2-MEC model, which adds the 2p2h-MEC contributions described in Section IV to the SuSAv2 approach, is used to describe the CC0π channel in neutrino interactions and the full regime in (e, e') reactions due to the extension of the RMF-based SuSAv2 approach to the inelastic regime. Work is in progress to apply this extension to the weak sector.

A.   Comparison with electron scattering data on ^{12}C

In this Section, we compare the SuSAv2-MEC predictions with inclusive ^{12}C (e, e') experimental data in a wide kinematical region. The QE regime is described in terms of the SuSAv2 model described in Section III E, which has been extended to include the complete inelastic spectrum — resonant, nonresonant and deep inelastic scattering — as described in [45, 94, 270]. We also discuss the impact of 2p-2h meson-exchange currents following the fully relativistic procedure described in Section IV. Our predictions are also compared with Rosenbluth separated cross section data in terms of longitudinal and transverse contributions. Finally, the extension of the SuSAv2-MEC formalism to other nuclei is also addressed. The capability of the model to describe electron scattering data with accuracy gives us confidence in the validity of its subsequent extension and application to recent neutrino oscillation experiments.

In what follows we present the double differential inclusive ^{12}C(e, e') cross section versus the energy transferred to the nucleus (ω), confronting our SuSAv2-MEC predictions with the available experimental data [15, 120]. Results are shown in Fig. 35: in each panel we show the three separate contributions to the inclusive cross section, namely, quasielastic, 2p-2h MEC and inelastic. We adopt the Bosted and Christy parametrization for the single-nucleon inelastic structure functions [268, 269] which describes DIS, resonant and non-resonant regions, providing a good description of the resonant structures in (e, e') cross sections and covering a wide kinematic region. For the QE regime, we employ the electromagnetic form factors of the extended Gari-Krumpelmann (GKex) model [282–284] which improves the commonly used Galster parametrization for $|Q^2| > 1$ GeV^2 (see [270] for details). The sensitivity of the QE results to the different parametrizations of the nucleon form factors has been discussed in [285] and it will be addressed in Section VII F. Additionally, for the Fermi momentum we employ the values given in [34], namely $k_F = 228$ MeV/c for ^{12}C.

The comparisons are carried out for kinematics ranging from low-intermediate energies to the highly-inelastic regime. Each panel corresponds to fixed values of the incident electron energy (E) and the scattering angle (θ). To ease the discussion, the panels have been ordered according to the corresponding value for the momentum transfer at the quasielastic peak, denoted as q_{QE}. This gives us the value of q where the maximum in the QE peak appears. However, it is important to point out that as ω varies, q also varies. For completeness, we also include in each panel a curve that shows how the momentum transfer changes with ω. Results illustrate that at very forward angles the value of q increases with the energy transfer, whereas this trend tends to reverse at backward angles. Thus for electrons scattered backwards, the q-values corresponding to the inelastic process are smaller than those ascribed to the QE regime. However, in this situation the cross section is clearly dominated by the QE peak. On the contrary, at very forward kinematics the inelastic process takes place at larger values of q. Thus, the two regimes, QE and inelastic, overlap strongly, the inelastic processes being the main ones responsible for the large cross sections observed at increasing values of ω. Finally, for intermediate scattering angles the behavior of q exhibits a region where it decreases (QE-dominated process), whereas for higher ω (inelastic regime) the behavior of q reverses and starts to go up. In these situations the QE peak, although significantly overlapped with the inelastic contributions, is clearly visible even for very high electron energies.

The systematic analysis presented in Fig. 35 demonstrates that the present SuSAv2-MEC model provides a very successful description of the whole set of (e, e') data, validating the reliability of our predictions. The positions, widths and heights of the QE peak are nicely reproduced by the model taking into account not only the QE domain but also the contributions given by the 2p-2h MEC terms (around $\sim 10 - 15\%$). Notice also that the "dip" region (between the QE and Δ peaks) is successfully reproduced by the theory. A more detailed analysis of the SuSAv2-MEC model with regard to (e, e') data can be found on [94, 270].

Some comments concerning the "dip" region are in order. This is the region where the QE and the inelastic contributions overlap the most and where FSI effects that modify in a significant way the tail of the QE curve at large ω-values can introduce an important impact. Moreover, the role of the 2p-2h MEC effects is essential because its maximum contribution occurs in this region. Thus, only a realistic calculation of these ingredients beyond the IA can describe successfully the behavior of the cross section.

To conclude, the accordance between theory and data in the inelastic regime, where a wide variety of effects are taken into account, also gives us a great confidence in the reliability of the calculations. The inelastic part of the cross section
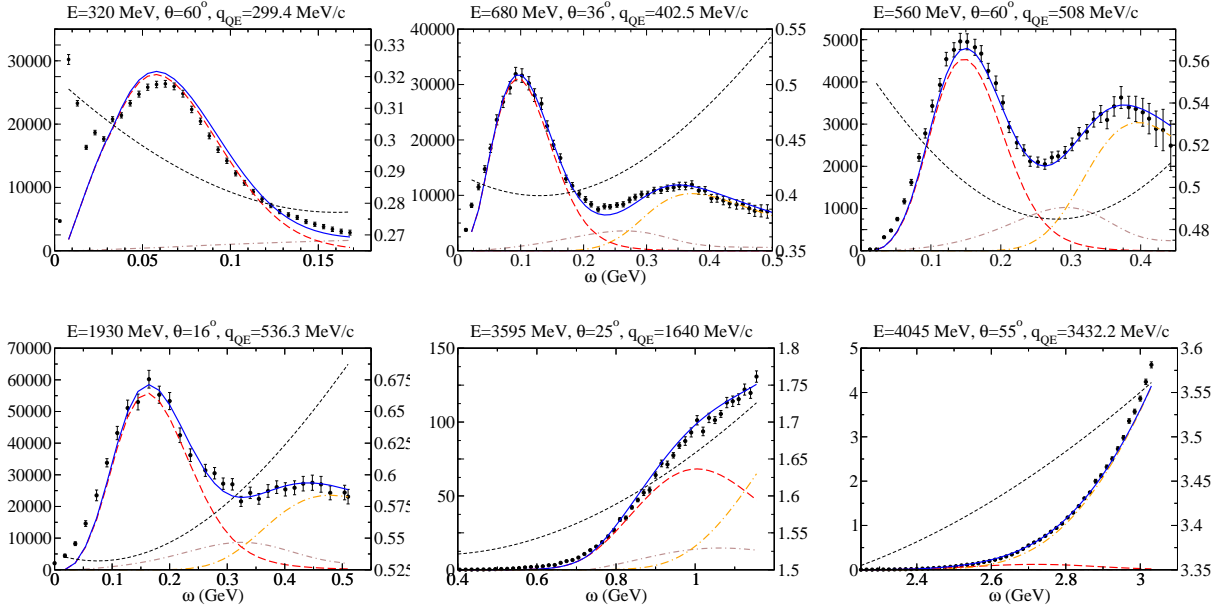
FIG. 35.   Comparison of inclusive ^{12}C(e,e') cross sections and predictions of the QE-SuSAv2 model (long-dashed red line), 2p-2h MEC model (dot-dashed brown line) and inelastic-SuSAv2 model (long dot-dashed orange line). The sum of the three contributions is represented with a solid blue line. The q-dependence with ω is also shown (short-dashed black line). The y-axis on the left represents $d^2\sigma/d\Omega/d\omega$ in nb/GeV/sr, whereas the one on the right represents the q value in GeV/c. Experimental data taken from [120, 281].

is dominated by the Δ-peak that mainly contributes to the transverse response function. At low electron scattering angles the longitudinal QE response function dominates the cross section and the inelastic contribution is smaller (as will be shown in Section VII B). The opposite holds at large scattering angles, where the Δ-peak contribution is important. On the other hand, for increasing values of the transferred momentum the peaks corresponding to the Δ and QE domains become closer, and their overlap increases significantly. This general behaviour is clearly shown by our predictions compared with data. In those kinematical situations where inelastic processes are expected to be important, our results for the QE peak are clearly below the data which is compensated by the larger inelastic contribution. On the contrary, when the inelastic contributions are expected to be small, the QE theoretical predictions get closer to data. Note also the excellent agreement in some very high energy situations (bottom panels in Fig. 35), even being aware of the limitations and particular difficulties in order to obtain phenomenological fits of the inelastic structure functions, and the reduced cross sections at these kinematics.

B.   Separate L/T analysis

The separate analysis of the longitudinal and transverse response functions of ^{12}C is presented in Fig. 36. The SuSAv2-MEC predictions are compared with data taken from Jourdan [23] based on a Rosenbluth separation of the (e, e') world data[13]. In each case we isolate the contributions corresponding to the QE, inelastic and 2p-2h MEC sectors. Three kinematical situations corresponding to fixed values of the momentum transfer have been considered in Fig. 36: $q = 300$ MeV/c, 380 MeV/c and 570 MeV/c. As observed, the longitudinal channel is totally dominated by the QE contribution. Only at very large values of ω does the inelastic process enter giving rise to a minor response, whereas the effects due to 2p-2h MEC are negligible. This result is in accordance with previous work [23, 60, 81, 287], and it clearly shows that the longitudinal response is basically due to one-nucleon knockout. On the contrary, the transverse sector shows an important sensitivity to MEC and inelastic processes. Note that the inelastic transverse response gives rise to the high tail shown by data at large ω-values, whereas the 2p-2h MEC can modify significantly the transverse response in the dip region as well as in the maximum of the QE peak. It is also worth mentioning that the natural enhancement in the transverse response arising from the RMF model included in the SuSAv2 approach is necessary in order to reproduce the separate L/T data, rejecting the idea of 0-th kind scaling.

From results in Fig. 36 we observe that the model leads to a reasonable agreement with data in both channels, although some discrepancies also emerge. In particular, the longitudinal prediction at $q = 300$ MeV/c ($q = 380$

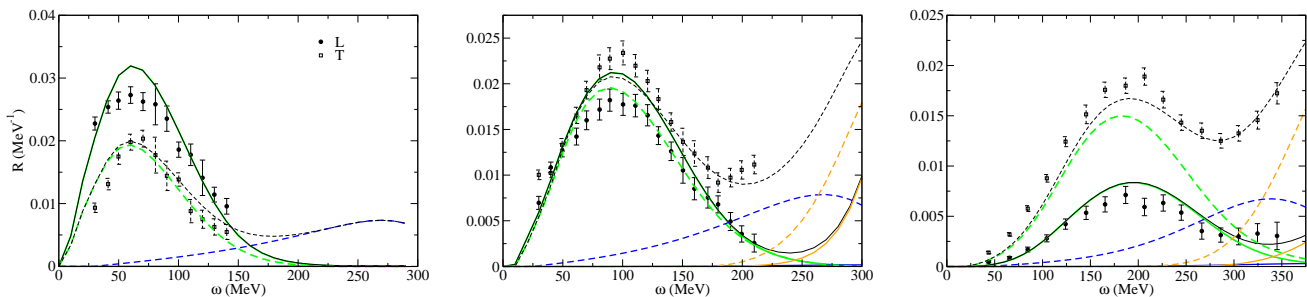[13] Notice that there still exist some debate on this L/T separation. See for instance [286].

FIG. 36. Analysis of the longitudinal (solid lines) and transverse responses (dashed lines) in (e, e') scattering at $q = 300$ MeV/c (left panel), $q = 380$ MeV/c (middle panel) and $q = 570$ MeV/c (right panel). QE, MEC and inelastic contributions are shown, respectively, as green, blue and orange lines. The total response is shown by the black lines. Data taken from [23].

MeV/c) overestimates the data by $\sim 12\%$ ($\sim 15\%$). It is important to point out that SuSAv2 is based on the existence of the scaling phenomenon for (e, e') data, and this is completely fulfilled when the value of q is large enough ($q \geq 400$ MeV/c). Therefore, the extension of the superscaling approach to low q-values is not well established even though a good agreement at low kinematics has been achieved in the previous section. Furthermore, the minor discrepancies observed may also be due to the specific Rosenbluth separation method used in [23], which introduces some level of model dependence through y-scaling assumptions and the treatment of radiative corrections.

C. Extension of the SuSAv2-MEC model to other nuclei

Once analyzed the capability of the SuSAv2 model to reproduce the ^{12}C(e, e') measurements, we extend the previous formalism to the analysis of electron scattering data on other nuclei. For this purpose, no differences in the scaling functions are assumed for the different nuclei except for the values used for the Fermi momentum and energy shift (see [45] for details). The use of the same scaling functions for different nuclear systems is consistent with the property of scaling of second type, *i.e*, independence of the scaling function from the nucleus, and it also follows from the theoretical predictions provided by the RMF and RPWIA models on which SuSAv2 relies. This has been studied in detail in previous works (see [33, 35, 46, 50, 52]) where the electromagnetic and weak scaling functions evaluated with the RMF and RPWIA approaches have been compared for ^{12}C, ^{16}O and ^{40}Ca. Other theoretical analyses for these nuclei can also be found in [81] and [288] in the framework of the RGF and CRPA models, respectively. In Figure 9 we compared the general RMF scaling functions for these nuclei, which exhibit no remarkable differences in terms of the nuclear species. Therefore, we apply the reference scaling functions for ^{12}C to the analysis of QE and inelastic regimes in other nuclei.

In the case of ^{16}O, the k_F-value selected ($k_F = 230$ MeV/c) is consistent with the general trend observed in [45], *i.e.*, an increase of the Fermi momentum with the nuclear density. Additionally, an offset of -4 MeV is applied with regard to the ^{12}C E_{shift}-values. The choice of the k_F- and E_{shift}-values provides a consistent analysis of the superscaling behavior in the deep scaling region below the QE peak, as shown in [270], and more importantly, it also provides a good agreement with electron scattering data.

Thus, in accordance with the previous analysis, we show in Fig. 37 (top panels) the predictions of the SuSAv2-MEC model for three different kinematical situations, corresponding to the available (e, e') data on ^{16}O. In all the cases we present the separate contributions for the QE, 2p-2h MEC and inelastic regimes. The 2p-2h MEC responses are extrapolated from the exact calculation performed for ^{12}C assuming the scaling law $R_{2p2h} \sim A k_F^2$ deduced in Ref. [289]. The inclusive cross sections are given versus the transferred energy (ω), and each panel corresponds to fixed values of the incident electron energy (E_i) and the scattering angle (θ).

As observed, the SuSAv2-MEC predictions are in very good accordance with data for all kinematical situations.

For completeness, we also present in the bottom panels of Figure 37 the calculations for the heavier target ^{40}Ca ($k_F = 241$ MeV/c, $E_{shift} = 28$ MeV within the RFG formalism [45]) where the comparison with data is again very precise from forward to very backward angles. The analysis of these results is relevant because of the similarity with ^{40}Ar, a target of interest for recent and forthcoming neutrino oscillation experiments. Note also that the 2p-2h MEC contributions are more prominent for ^{40}Ca than for ^{12}C and ^{16}O with respect to the QE regime due to the different k_F dependence of the QE and 2p-2h MEC contributions, A/k_F and $A k_F^2$, respectively [293].
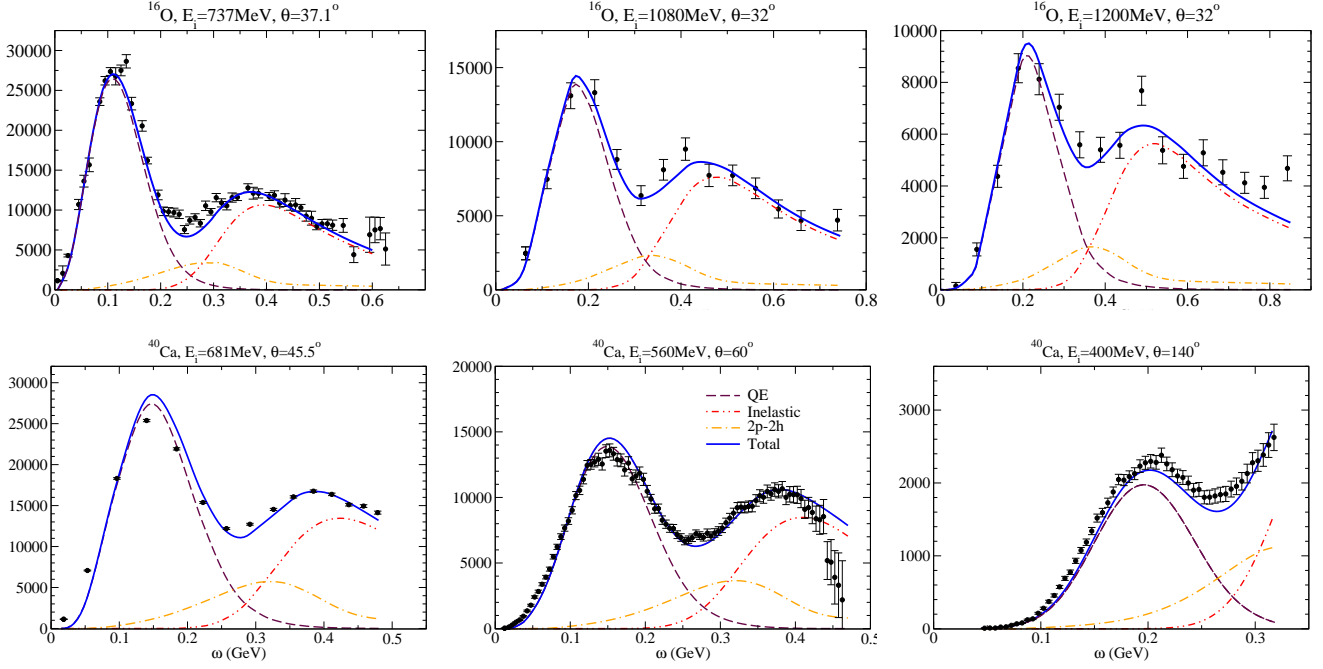
FIG. 37. Comparison of inclusive $^{16}\text{O}(e,e')$ (top panels) and $^{40}\text{Ca}(e,e')$ (bottom panels) cross sections and predictions of the SuSAv2-MEC model. The separate contributions of the pure QE response (dashed line), the 2p-2h MEC (dot-dashed), inelastic (double-dot dashed) are displayed. The sum of the three contributions is represented with a solid blue line. The y axis represents $d^2\sigma/d\Omega/d\omega$ in nb/GeV/sr. Data from Refs. [61, 290–292].

D.   Comparison with recent JLab data

In addition to the previous analyses, we have also tested the validity of the SuSAv2-MEC model and the scaling rules applied when extrapolating to different nuclei through the analysis of the recent inclusive electron scattering JLab data [17] on three different targets (C, Ar and Ti) [294]. As observed in Fig. 38, the agreement is very good over the full energy spectrum, with some discrepancy seen only in the deep inelastic region. The 2p2h response, peaked in the dip region between the QE and Δ-resonance peak, is essential to reproduce the data. We also analyze in Fig. 39 the general behavior of the data in terms of scaling of second kind: if this kind of scaling was perfectly fulfilled the superscaling function extracted from the data should be independent of k_F. Deviations from this behaviour indicate a violation on second kind scaling. In Fig. 39 we show that the 2p2h response scales very differently from the quasielastic one, in full accord with what was predicted by the model. As observed, scaling of second kind only works in the QE peak, then it breaks down because non-impulsive contributions (2p2h) and inelastic channels come into play, consistently with previous analyses [18, 19]. We also present (bottom panel) the superscaling function $f(\psi')$ but divided by η_F^3, where $\eta_F \equiv k_F/m_N$. As shown, scaling is highly broken in the QE peak (results for carbon are significantly higher), however, results collapse into a single curve within the dip region. This result confirms our previous study in [289], where we predicted that 2p2h response scales as k_F^3. It is important to point out that the minimum in the cross section shown in Fig. 39 corresponds to the maximum in the 2p2h contribution (see Fig. 38). Although contributions from the QE and inelastic domains also enter in the dip region, and this may at some level break the scaling behavior, the results in the bottom panel of Fig. 39 strongly reinforce our confidence in the validity of our 2p2h-MEC model. It is also interesting to note that the same type of scaling, i.e, $f(\psi') \sim \eta_F^3$, seems to work reasonably well not only in the dip region but also in the resonance and DIS domains. Further studies on the origin of this behavior are underway. Overall, these results represent a valuable test of the applicability of the model to neutrino scattering processes on different nuclei. A more detailed analysis of these results can be found in [294].
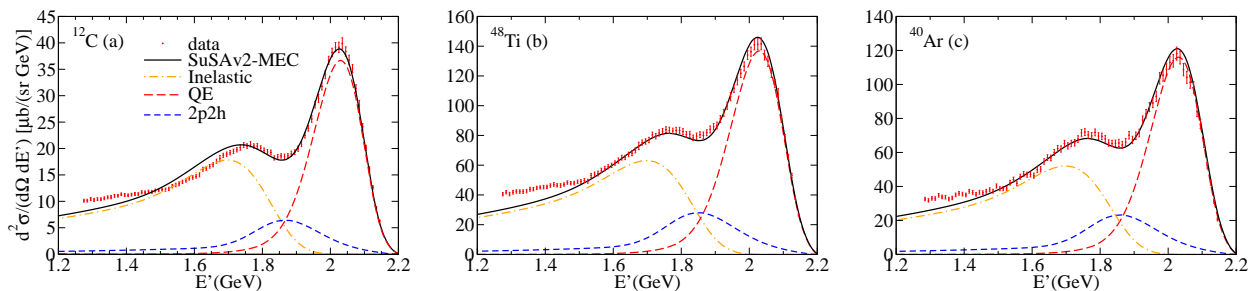
FIG. 38. The (e, e') double differential cross section of carbon, titanium and argon from [16, 17], compared with the SuSAv2-MEC prediction. For completeness, the separate QE, 2p2h and inelastic contributions are also shown. The beam energy is $E=2.222$ GeV and the scattering angle $\theta=15.541$ deg.
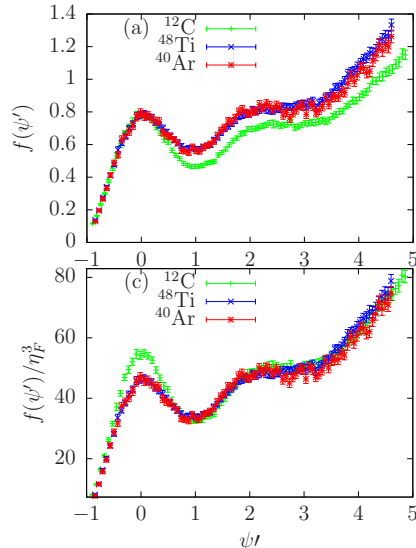

FIG. 39. The superscaling function f (top) and f divided by η_F^3 (bottom) extracted from the JLab data [16, 17].

E. Comparison with neutrino scattering data

In this Section we present our theoretical predictions compared with charged-current neutrino scattering data from different collaborations, mainly T2K [295, 296] and MINERvA [297, 298], but we will also analyze MiniBooNE kinematics [299, 300]. The SuSAv2-MEC model, that has already proven to describe accurately (e, e') data (see previous section), is here applied to the analysis of recent neutrino data with the aim of showing its capability to describe successfully a large variety of experimental measurements covering a wide range of kinematics. Our study is mainly restricted to the "quasielastic-like" regime where the impulse approximation used to describe the one-nucleon knockout process in addition to the effects linked to the 2p-2h meson-exchange currents play a major role.

Other models [67, 70, 71, 77, 80, 86, 102, 103, 108, 232, 301–313] have been developed to describe such 1p1h and 2p2h processes for CC neutrino reactions, also providing appropriate descriptions of the experimental measurements. It is important to note that although a similar comparison with inclusive neutrino measurements can be reached, these models rely on different assumptions and descriptions of the nuclear dynamics. Further comparisons of these models with more exclusive measurements could help to determine the goodness of the different approaches.

In Fig. 40 we show the T2K CC0π (anti)neutrino data on ^{12}C and ^{16}O in comparison with the SuSAv2-MEC model. The CC0π scattering is defined, equivalently to the CCQE-like one, as the process where no pions are detected in the final state. As already explained in previous sections, quasielastic (QE) scattering and multi-nucleon excitations dominated by 2p-2h MEC contributions should be included in the analysis together with other minor effects such as pion-absorption processes in the nucleus that can mimic a CCQE-like event. However, as will be shown in Section VII H, the pion-absorption effects are not particularly relevant at T2K kinematics. Note also that these two main mechanisms, QE and 2p2h, have in general a different dependence upon the nuclear species, namely they scale differently with the nuclear density[289], as previously analyzed. As observed in Fig. 40, the SuSAv2-MEC model is capable of reproducing the T2K data for both nuclei [314], which can help to disentangle how nuclear effects enter in the analysis of the T2K experiment as well as to reduce nuclear-medium uncertainties. It is interesting to point out the results for the most forward angles, *i.e.,* the panel on the right-bottom corner. Notice that the QE and 2p-2h
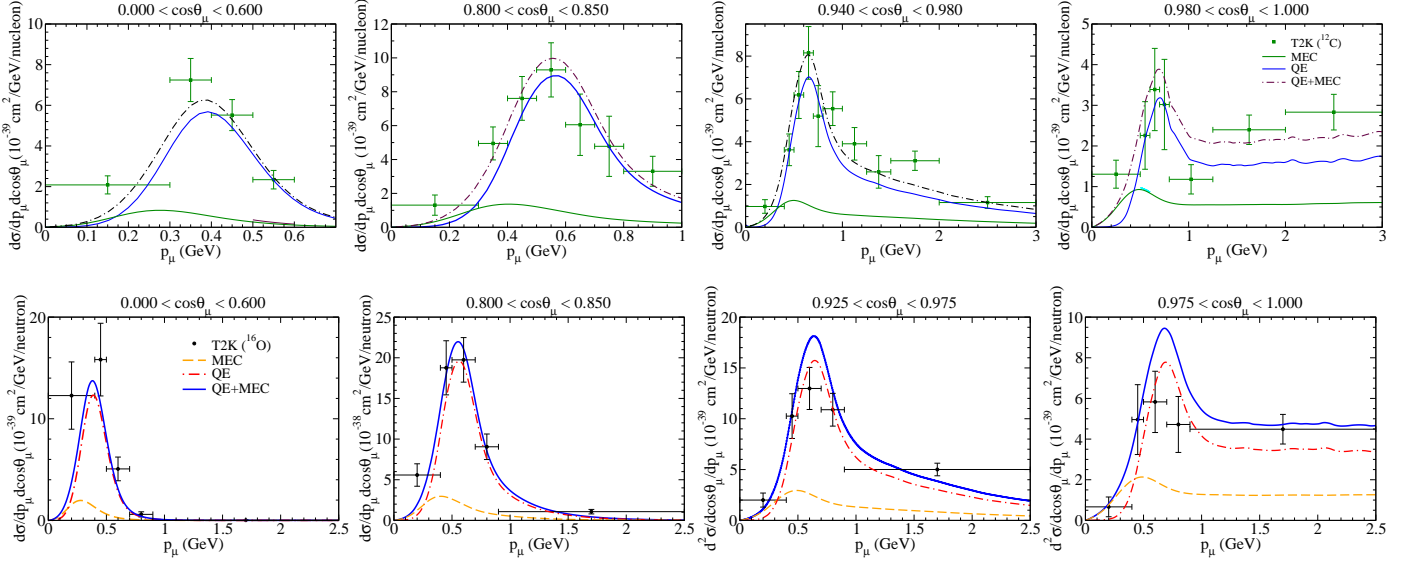
FIG. 40. The T2K flux-integrated CCQE and 2p2h double-differential cross-section for neutrino for scattering on ^{12}C (top panels) and ^{16}O (bottom panels), within the SuSAv2-MEC model at T2K kinematics in units of 10^{-39} cm^2/GeV per nucleon (for carbon) and per nucleon target (for oxygen). The CC0π T2K data are from Ref. [295] and [296].
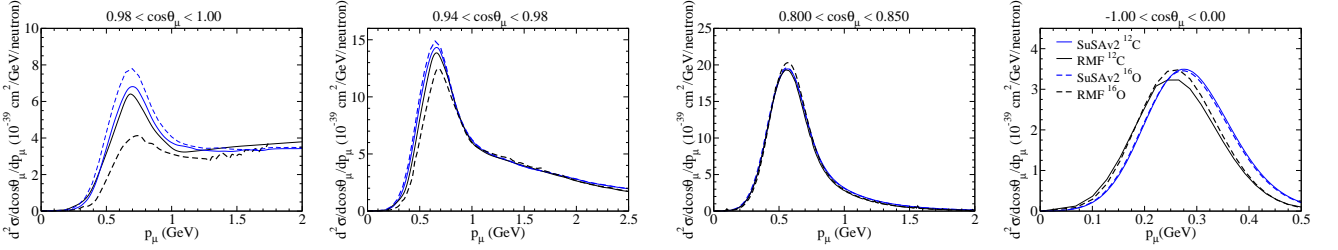

FIG. 41. Comparison of double differential cross sections on ^{12}C (solid lines) and ^{16}O (dashed lines) at T2K kinematics within the SuSAv2 and RMF models. Results are displayed from forward to backward angles.

MEC contributions are stabilized to values different from zero for increasing muon momenta as a consequence of the high energy tail of the T2K neutrino flux. This is at variance with all remaining situations where the cross sections decrease significantly as the muon momentum p_μ goes up. It is also important to notice that the slight overestimation of the SuSAv2 predictions in the peaked region at very forward angles is clearly related to the limitations of the model at very low q and ω values where RMF scaling violations due to nuclear-medium effects are not properly included in the SuSAv2 approach. This drawback of the model will be solved in the forthcoming ED-RMF approach [207, 315]. This point is also stressed in Fig. 41 where large differences between RMF predictions for ^{12}C and ^{16}O are observed due to different nuclear-medium effects and binding energies, while these effects are not properly accounted for in the current SuSAv2 approach where the results for ^{12}C and ^{16}O are pretty similar. In this sense, it is important to mention the recent exploration of the C/O differences carried out by the T2K Collaboration [316], that has allowed to analyze the validity of various models to extrapolate between carbon and oxygen nuclear targets, as is required in T2K oscillation analyses, showing particular model separation for very forward-going muons. As also observed in [316], the SuSAv2 approach overestimates these new data at very forward angles while the RMF model corrects this drawback, yielding a good agreement at low kinematics.

Next, in Fig. 42 we compare the SuSAv2-MEC predictions with the recent MINERvA QE-like double differential (anti)neutrino cross sections on hydrocarbon (CH), as a function of the transverse (with respect to the antineutrino beam) momentum of the outgoing muon, in bins of the muon longitudinal momentum. The relativistic nature of the model makes it suitable to describe these data [297, 317], which correspond to a mean beam energy of 3.5 GeV. The standard SuSAv2 model predictions agree well with the data without needing any additional or tuned parameter. For

the data comparison we use the same nomenclature employed in the experimental paper [297, 298]. The "QE-like" experimental points include, besides pure quasielastic contributions, events that have post-FSI final states without mesons, prompt photons above nuclear de-excitation energies, heavy baryons, or protons above the proton tracking kinetic energy threshold of 120 MeV, thus including zero-meson final states arising from resonant pion production followed by pion absorption in the nucleus and from interactions on multinucleon states. This is similar to the so-called CC0π definitions used in T2K. On the contrary, the "CCQE" signal (also defined in other experiments as "CCQE-like") corresponds to events initially generated in the GENIE neutrino interaction event generator [249] as quasi-elastic (that is, no resonant or deep inelastic scatters, but including scatters from nucleons in correlated pairs with zero-meson final states), regardless of the final-state particles produced, thus including CCQE and 2p2h interactions. The difference between the two data sets, mainly due to pion production plus re-absorption, varies between ∼ 15% and ∼ 5% depending on the kinematics. According to MINERvA's acceptance, the muon scattering angle is limited to $\theta_\mu < 20°$ as well as the muon kinematics (1.5 GeV < $p_{||}$ < 15 GeV, p_T < 1.5 GeV) in both experimental and theoretical results, leading to a significant phase-space restriction for large energy and momentum transfer to the nuclear target.

The antineutrino-H contribution in the cross sections only enters through the 1p1h channel and has been evaluated by computing the elastic antineutrino-proton cross section. The present calculation does not include processes corresponding to pion emission followed by re-absorption inside the nucleus. Therefore the curves are meant to be compared with the "CCQE" data rather than with the "QE-like" ones. However, we also display the QE-like cross sections, to illustrate MINERvA's estimation of the magnitude of the QE-like resonance component among other minor effects. A more detailed analysis of these results together with a χ^2 test can be found in [317], where the SuSAv2 χ^2 seems to be very similar to the MINERvA/GENIE ones and compatible with data.
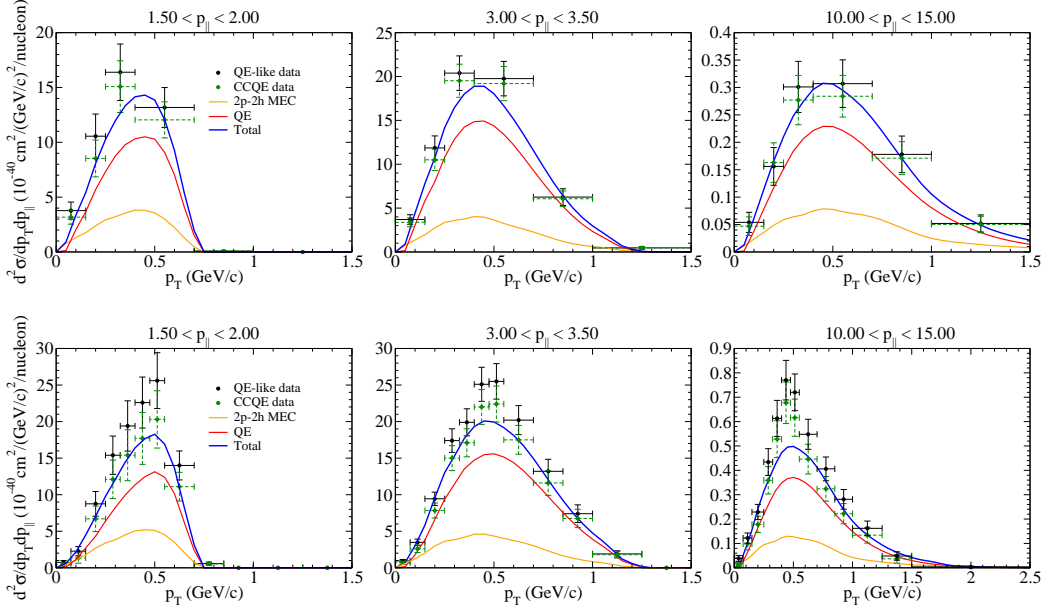

FIG. 42. (Color online) The MINERvA "QE-like" and "CCQE" double differential cross sections for $\bar{\nu}_\mu$ (top panels) and ν_μ (bottom panels) scattering on hydrocarbon versus the muon transverse momentum, in bins of the muon longitudinal momentum (in GeV/c). The curves represent the prediction of the SuSAv2+2p2h-MEC (blue) as well as the separate quasielastic (red) and 2p2h-MEC (orange) contributions. The data and the experimental fluxes are from Refs. [297] and [298] .

For completeness, it is worth mentioning that in the specific kinematic conditions of MINERvA, it clearly appears that, even if the neutrino energy is as large as 3 GeV, the process is largely dominated by relatively small energy and momentum transfer, namely, $\omega < 500$ MeV, $q < 1000$ MeV, whereas contributions below $\omega < 50$ MeV, $q < 200$ MeV govern the lowest Q^2_{QE} region. More specific details can be found in Refs. [107, 318].

F. Form Factors analysis

As already considered in the analysis of (e, e') reactions, here we also adopt the electromagnetic nucleon form factors of the extended Gari-Krumpelmann (GKeX) model [282–284] for the vector CC current entering into neutrino cross

sections. As described in [270], this prescription improves the commonly used Galster parametrization at $Q^2 > 1$ GeV^2. For completeness, we show in Figure 43 the sensitivity of the total CCQE neutrino cross section within the SuSA approach for the different up-to-date parametrizations of the nucleon form factors (see Refs. [9, 285] for details): all of them are essentially equivalent for the MiniBooNE kinematics, while some difference emerges at the energies of the NOMAD experiment, which implies larger Q^2 values. Similar comments also apply to the SuSAv2 model.
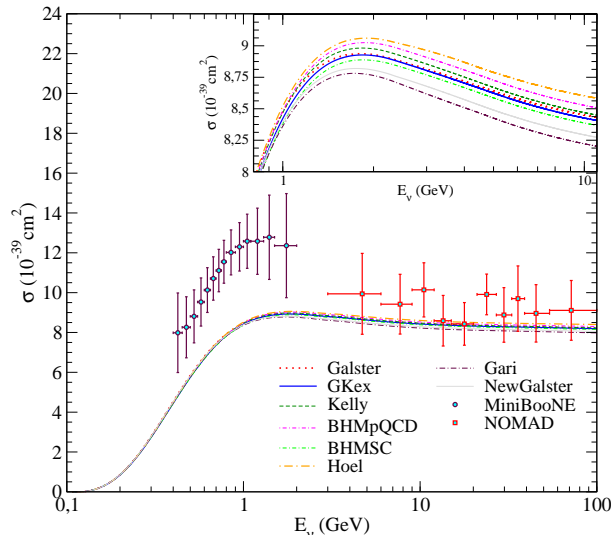
FIG. 43. CCQE $\nu_\mu - {}^{12}$C cross section per nucleon evaluated in the SuSA model for various parametrizations of the nucleon electromagnetic form factors [285]. A sub-panel zooming in the region near the maximum is inserted on the top. The MiniBooNE [299] and NOMAD [319] data are also shown for reference.

Regarding the axial contributions, we employ the commonly used dipole axial nucleon form factor described in [270] where a comparison between dipole and monopole axial form factor is shown together with a discussion on the axial coupling g_A parameter. More recently, we have also compared the dipole axial form factor with other choices based on the so-called two-component model [320, 321], consisting of a three-quark intrinsic structure surrounded by a meson cloud. In [270] a joint fit to neutrino-nucleon scattering and pion electroproduction data has been performed to evaluate the nucleon axial form factor in the two-component model. Further constrains on the model are obtained by re-evaluating the electromagnetic form factor using electron scattering data. The results for this new fit of the axial form factor show sizable differences at some kinematics with respect to the dipole model. The impact of such changes on the CCQE neutrino-nucleus cross-section is evaluated in the SuSAv2 nuclear model in comparison with recent T2K and MINERvA measurements in Figs. 44 and 45, respectively. The two-nucleon component approach was successful in describing the EM form factors [321–323], the strange form factors of the proton [324] and was applied to the deuteron as well [325]. Advantages of this model are that it contains a limited number of parameters and can be applied both in the space- and time-like regions. The extension to axial form factors has been done in [326].

Following Ref. [320], the axial nucleon form factor is parametrized in the two-component approach as:

$$
G_A(Q^2) = G_A(0)\, g(Q^2) \left[1 - \alpha + \alpha \frac{m_A^2}{m_A^2 + Q^2} \right] \,,
$$
$$
g(Q^2) = \left(1 + \gamma Q^2 \right)^{-2} \,, \tag{151}
$$

where $Q^2 > 0$ in the space-like region and α is a fitting parameter which corresponds to the coupling of the photon with an axial meson. One can fix $m_A = 1.230$ GeV, corresponding to the mass of the axial meson $a_1(1260)$ with $I^G(J^{PC}) = 1^-(1^{++})$. The form factor $g(Q^2)$ describes the coupling to the intrinsic structure (three valence quarks) of the nucleon. Note that setting $\alpha = 1$ and $\gamma = 0$, the usual dipole axial functional form is recovered.

The results of fit to pion electroproduction data and neutrino scattering data for different extractions of the pion data can be seen in [327]. Here we will focus on the two most extreme cases, the Soft Pion dataset and the PCAC (Partially Conserved Axial Current) one, also detailed in [327]. The impact of the axial form factor choice on the CCQE-like cross section is illustrated in Figs. 44 and 45 for T2K and MINERvA kinematics, respectively.

The largest differences between neutrino cross-sections evaluated with different form factors is about 5%. By mapping the muon kinematics (p_μ, θ_μ) into Q^2 on the basis of [327], the largest difference with respect to the cross-section with dipole form factor appears always in correspondence of $Q^2 \sim 0.5$ GeV^2 for Soft Pion. For forward
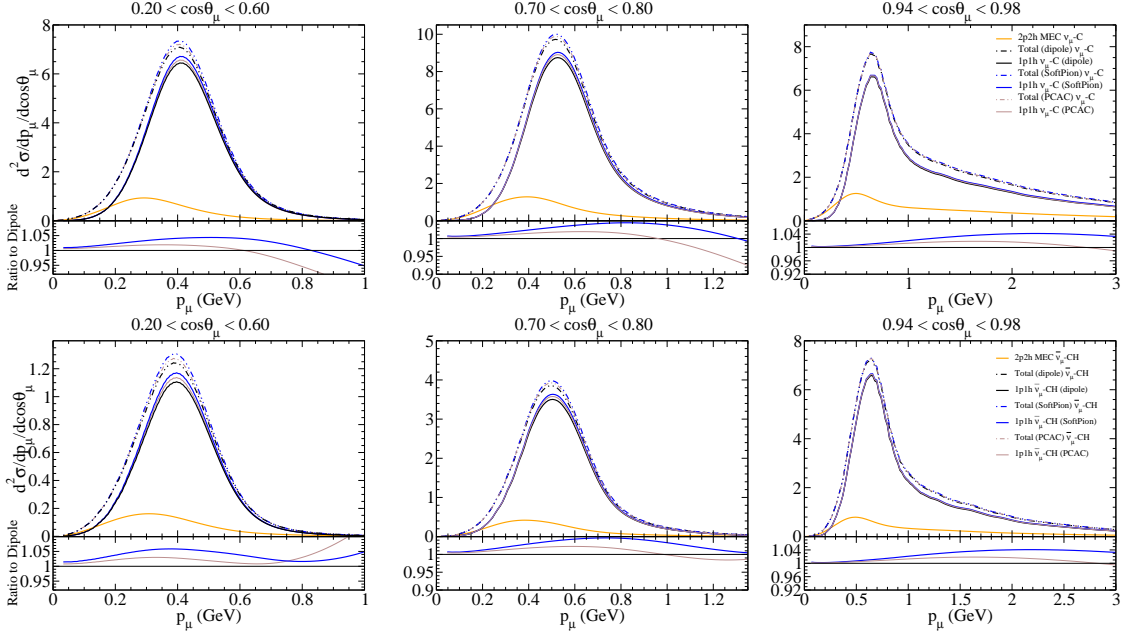
FIG. 44. The T2K flux-integrated CCQE and 2p2h double-differential cross-section for neutrino (first row) and antineutrino (second row) within the SuSAv2-MEC model, using different form factors. Results are displayed for different bins of the muon scattering angle as functions of the muon momentum. Double differential cross sections are shown in units of 10^{-39} cm^2/GeV per nucleon.

angles, the relevant kinematic region is $Q^2 \sim 0.5$ GeV^2 where the cross-section is mostly unaffected by form factor differences. For backward angles, the $Q^2 \sim 0.5$ GeV^2 region corresponds instead exactly to the region of larger cross-section with intermediate muon momentum, thus the impact of form factors difference is larger, as detailed on [327]. In the backward region, the form factor differences can reach 5%. In such region the effect in the antineutrino case is even larger, up to 10%. Still, in the neutrino-antineutrino asymmetry the effect is at % level (see [327] for a detailed analysis of the $\nu - \bar{\nu}$ asymmetry). The region $Q^2 > 1$ GeV, where the different axial form factors depart from each other sizeably, is negligible in T2K data.

The effects of axial form factors at MINERvA kinematics are shown via the analysis of the double differential cross-section as a function of p_T, p_L in Fig 45. The region of $Q^2 \simeq 0.5$ GeV^2 shows differences of the order of 5%, similarly to T2K, while in the region of high p_T and lower cross-section effects up to 10% and above can be observed.

Overall the agreement of the SuSAv2-MEC model with data, using the different axial form factors, is positive but the experimental uncertainties on T2K and MINERvA measurements do not allow yet to clearly discriminate between the various evaluations. It is interesting to note that, in the model considered here, the form factor effects have a different Q^2 dependence than the one of 2p2h, as well as a different neutrino/antineutrino dependence, making the disentagling of nucleon and nuclear effects feasible in future with higher statistics measurements. The feasibility of this approach relies on the capability of exploiting external data to drive the Q^2 dependence of the form factor. For this reason, the investigation of the earlier data of pion electro-production, as shown in [327], is of primary importance.

G. Relevance of L/T channels for neutrino reactions

In this section we study in detail the relevance of the different longitudinal and transverse channels that contribute to the QE and 2p-2h MEC at MiniBooNE kinematics, also accounting for the corresponding axial and vector contributions which arise from the hadronic currents. The conclusions extracted from this analysis are roughly extensible to the ones from the T2K and MINERvA experiments, whose relevant kinematic regions are not significantly different.

An analysis on the different channels for the 2p-2h MEC nuclear responses and the total cross section was addressed in [107, 270], showing a predominance of the transverse responses over the longitudinal ones. In the latter the pure
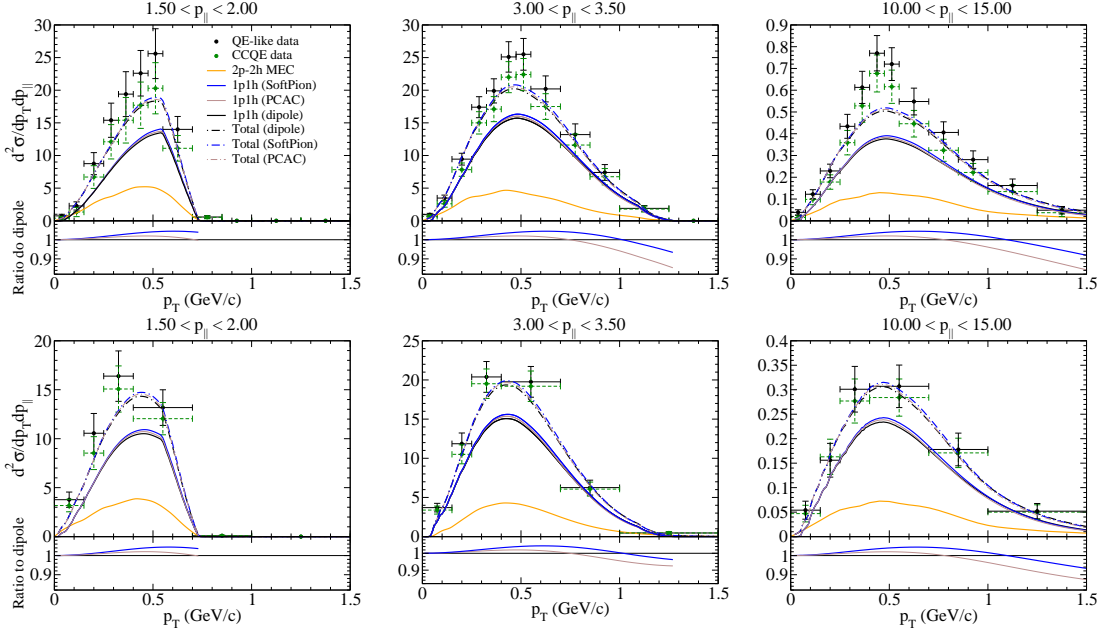
FIG. 45. MINERvA flux-integrated double-differential cross-section for different axial form factors, as a function of the muon transverse and longitudinal momentum, for neutrino (first row) and antineutrino (second row) double differential cross sections $(10^{-39}$ cm^2/GeV^2 per nucleon).

vector contributions were negligible in comparison with the axial ones. Moreover, the separate transverse channels, T_{VV}, T_{AA} and T'_{VA}, while showing some remarkable differences for different q values, contribute in a similar way to the total cross section. This is due to the relevant kinematic regions explored which goes from 0.3 GeV/c up to 1 GeV/c in q and from 0.3 GeV to 0.8 GeV in ω [107, 270]. Here we investigate the relevance of the different channels at kinematics relevant for MiniBooNE, T2K and MINERvA experiments. In Fig. 46 the separate 2p-2h MEC contributions to the different channels $(L, T_{VV}, T_{AA}$ and $T'_{VA})$ corresponding to the MiniBooNE double differential cross section at different bins of the muon scattering angle are presented.

Results in Fig. 46 show the differences between the T_{AA} and T_{VV} contributions, the latter being shifted to higher T_μ values by about 50 MeV for all angular bins. At very forward angles, *i.e.*, lower q-values, the global magnitude of the AA channel is greater than the VV one, in accordance with the results observed in [270], where the T_{VV} and T_{AA} responses differ roughly by a factor 2 at the maximum at q of the order of 400 MeV/c. Concerning the interference T'_{VA} component, its magnitude is not particularly different from the VV and AA ones at very forward angles, being on the contrary the most relevant term at larger angles. Finally, although the longitudinal channel gives the smallest global contribution, its role is essential in order to interpret antineutrino scattering at backward angles. This is a consequence of the negative T'_{VA} term for antineutrino reactions that almost cancels out the $T_{VV} + T_{AA}$ contribution. The conclusions that can be extracted from these results launch a warning to those 2p2h models which neglect the longitudinal contributions in their analysis as well as to those ones who extrapolate the results from electrons (purely vector responses) to the weak ones (vector+axial), making those approaches rather questionable in some cases. The same conclusions apply to the recent MINERvA results shown in Fig. 47.

The conclusions extracted from the previous analysis on the 2p-2h MEC cross section also apply for the separate QE contributions to neutrino and antineutrino cross sections. The different QE channels are analyzed for the MiniBooNE double differential cross sections in Fig. 48, where the transverse contribution predominates at all kinematics whilst the net longitudinal channel, even not being a relevant contribution, is essential to describe antineutrino data at backward kinematics together with the 2p-2h longitudinal one.

In Fig. 49 we show the breakdown of the total integrated neutrino cross sections into $L(= L_{VV} + L_{AA})$, $T(= T_{VV} + T_{AA})$, T_{VV}, T_{AA} and T'_{VA} contributions, with the last occurring as a positive (constructive) term in the neutrino cross section and a negative (destructive) term in the antineutrino one. The sign of the T'_{VA} channel represents the main difference between the total neutrino and antineutrino cross sections. In addition to the opposite sign in the VA response, some minor differences between neutrino and antineutrino cross sections arise from the Coulomb distortion of
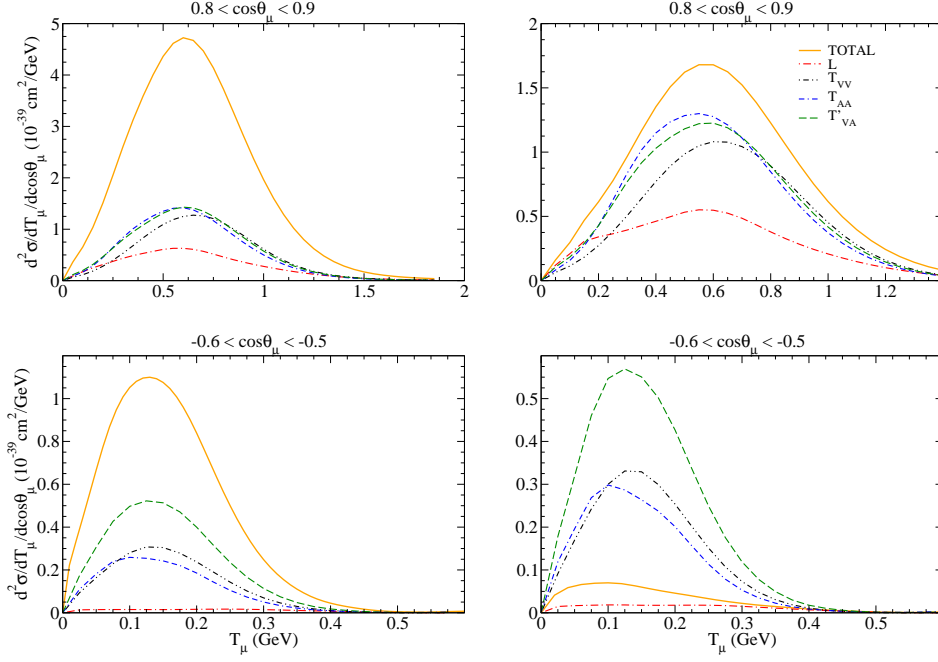
FIG. 46. Comparison of the different 2p-2h MEC channels for the ν_μ (left panels) and $\overline{\nu}_\mu$ (right panels) MiniBooNE double differential cross section.
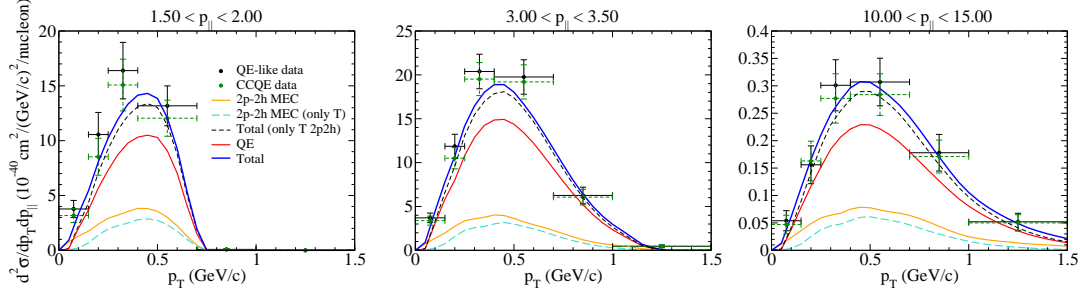

FIG. 47. (Color online) As Fig. 42, but showing the separate contribution of the pure transverse MEC (dashed curves) to also stress the relevance of the longitudinal MEC channel.

the emitted lepton and the different nuclei involved in the CC neutrino (nitrogen) and antineutrino (boron) scattering processes on carbon. We also notice that below 1 GeV the T'_{VA} response is higher than the T_{VV} one but of the same order as the T_{AA} one. Note that the maximum of the VA channel is around the peak of the MiniBooNE neutrino flux. On the contrary, the VA contribution to the cross section is negligible at energies above 10 GeV as a consequence of the small values of the axial form factor G_A and the lepton factor $V_{T'}$ at high E_ν and $|Q^2|$ (see [270] for details). This is also in agreement with some previous QE results [285]. As a consequence, for very high ν_μ ($\overline{\nu}_\mu$) energies (above ~ 10 GeV) the total cross section for neutrinos and antineutrinos is very similar. Only the L and T channels contribute for the higher values explored by NOMAD experiment. On the contrary, in the region explored by the MiniBooNE collaboration, the main contributions come from the two transverse T and T' channels.
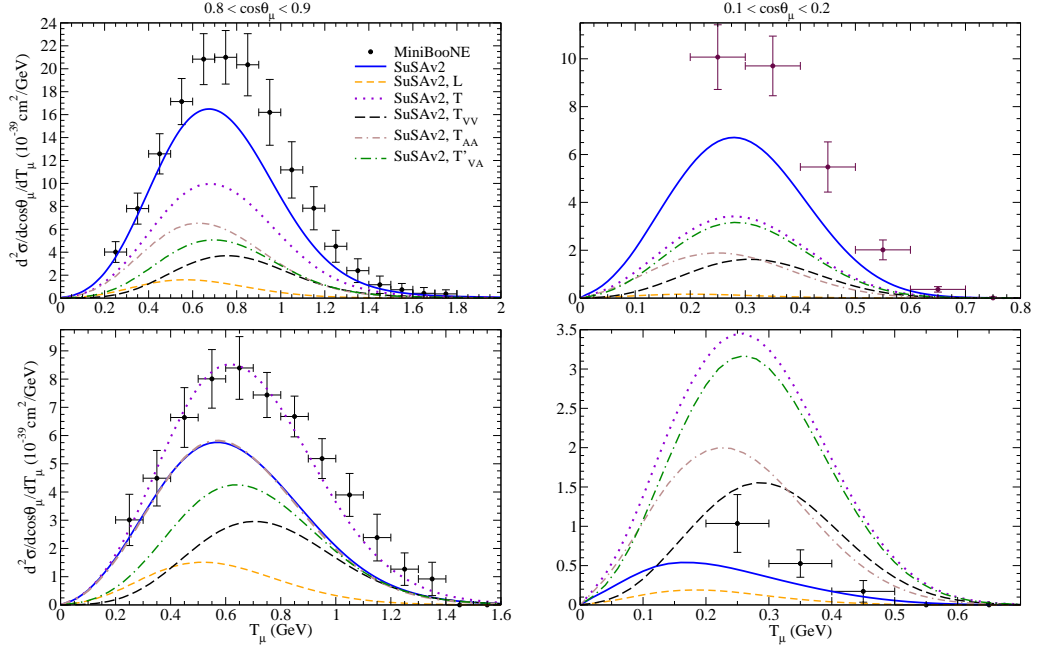
FIG. 48. Separation into components of the MiniBooNE CCQE ν_μ (top panel) and $\overline{\nu}_\mu$ (bottom panel) double-differential cross section per nucleon displayed versus T_μ for various bins of $\cos\theta_\mu$ within the SuSAv2 approach. The MiniBooNE data [299, 300] are also shown for reference.
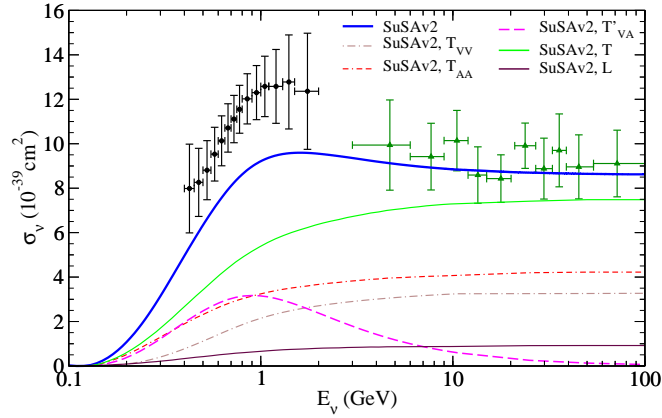

FIG. 49. Separation into components of the CCQE ν_μ cross section per nucleon on ^{12}C displayed versus neutrino energy E_ν within the SuSAv2 approach. The MiniBooNE [299] and NOMAD [319] data are also shown for reference.

H. Implementation of the SuSAv2-MEC and RMF models in MC event generators and extension to semi-inclusive processes

In Section VII, the SuSAv2-MEC model has been shown to be capable of reproducing the nuclear dynamics and superscaling properties observed in (e, e') reactions which serves as a stringent test for nuclear models, whilst also providing an accurate description of existing neutrino data. Up to now, SuSAv2-MEC is the only fully relativistic model that can be extended without kinematical restrictions or further approximations to the full-energy range of interest for present and future neutrino experiments. This has motivated the implementation of SuSAv2-MEC 1p1h and 2p2h contributions in the GENIEv3 MonteCarlo neutrino interaction simulation [109] in order to use it to better

characterise nuclear effects in T2K and MINERvA neutrino scattering cross-section measurements. Work is also in progress to implement it in NEUT [251].

Accordingly, we present in this section the implementation and validation of the SuSAv2-MEC 1p1h and 2p2h models in the GENIE neutrino-nucleus interaction event generator and a comparison of the subsequent predictions to measurements of lepton and hadron kinematics from the T2K experiment. These predictions are also compared to those of other available models in GENIE. We additionally compare the semi-inclusive predictions of the implemented 1p1h model to those of the microscopic model on which SuSAv2 is based - Relativistic Mean Field (RMF) - to begin to test the validity of widely-used 'factorisation' assumptions employed by generators to predict hadron kinematics from inclusive input models. The results highlight that a more precise treatment of hadron kinematics in generators is essential in order to attain the few-% level uncertainty on neutrino interactions necessary for the next generation of accelerator-based long-baseline neutrino oscillation experiments. More details about this analysis and the implementation can be found in [109].

The recent experimental interest on more exclusive measurements is related to the information about the final state nucleons that they provide, such as those which have recently been performed by T2K [328] and Minerva [329], which have been demonstrated to have a much more acute sensitivity to the different nuclear effects involved in neutrino-nucleus interactions. Unfortunately a comparison of these measurements directly to microscopic models requires semi-inclusive or exclusive predictions which the majority of models are not able to make, as they simplify their calculations by integrating over outgoing nucleon kinematics. An exception to this is the RMF model, used to construct the SuSAv2 predictions, which is capable of semi-inclusive predictions for neutrino reactions[14]. As described in [109], the simulations used by experiments circumvent this limitation by factorising the leptonic and hadronic components of the interaction. Among other approximations, this approach relies strongly on a semi-classical description of FSI and the distribution of initial state nucleon kinematics seen by the probe being independent of its energy and momentum transfer.

The implementation of the SuSAv2 1p1h model in GENIE provides a first opportunity to test the factorisation approach in event generators as well as to compare with other models available in event generators. In Figs. 50 and 51 we show a comparison of the SuSAv2 and Valencia model [77, 103] predictions (1p1h and 2p2h) as implemented in GENIE on top of GENIE's Berger-Sehgal pion production prediction for T2K inclusive CC0π and 'semi-semi-inclusive' CC0πNp results, being the latter a semi-inclusive cross section where the final state proton is below 500 MeV/c. This clearly shows that the implemented Valencia and SuSA models differ substantially, with only the SuSA model able to describe the very forward data and the Valencia model describing the mid-angle data a little better. The discrepancies between the model and data for the inclusive and semi-inclusive results are consistent, suggesting that they at least partially stem from the underlying inclusive cross section model.

Beyond the inclusive comparison, the 'semi-semi-inclusive' predictions within the kinematic region where SuSAv2 is a good description of RMF allows us to study the validity of the factorisation approach used in event generators. Here it can be seen that the implementation with both the kinematic-dependent binding energy and with FSI is closest to reproducing the RMF microscopic model prediction, but still appears to peak at too low muon momentum and also fails to describe the higher momentum region. It can also be seen that variations to the hadronic component of the interaction cause substantial alterations to the predictions, highlighting the role of these nonphysical freedoms available within the factorisation approach. Further work will focus on more stringent tests through the implementation of the RMF spectral function into event generators and by exploring the predictions in a wider region of hadronic kinematic phase-space.

The T2K semi-inclusive CC0π measurement of interactions with protons less than 500 MeV [328] also provides an opportunity to compare the RMF semi-inclusive model predictions to data, which is shown in Fig. 52 alongside the SuSAv2-GENIE predictions using the factorisation approach. In order to make this comparison the RMF predictions are added to the SuSAv2-MEC (2p2h) and pion-absorption predictions from GENIE (for pion production the Berger-Sehgal model was used [330]). In general, we observe a fair agreement of both RMF+GENIE (SuSAv2-2p2h+π-abs) and GENIE (SuSAv2-1p1h+SuSAv2-2p2h+π-abs). The overestimation of data at very forward angles by the SuSAv2-GENIE is ascribed to the aforementioned low energy transfer scaling violations absent in the SuSAv2-model but present in RMF, thereby explaining the better agreement achieved with the latter. On the contrary, the larger results from SuSAv2-1p1h at very backward angles compared to RMF are related to the previously discussed FSI treatment alterations. In general, it is clear that RMF performs better within the most forward angular bins (where additional RMF effects are most important). The recently developed Energy-Dependent RMF (ED-RMF) model [207, 315], which keeps the original RMF potentials at low kinematics but make them softer for increasing nucleon momenta, following the SuSAv2 approach, will solve the limitations of the SuSAv2 model at forward angles while solving the

---

[14] The RMF model has proven its validity to address exclusive predictions for electron scattering [37] and work is underway to fully extend it to neutrino reactions.
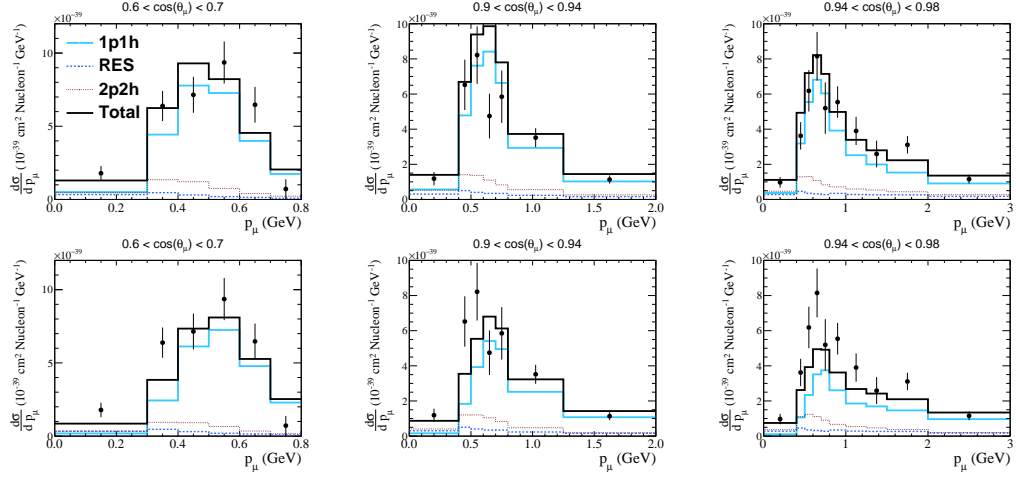
FIG. 50. Comparison of the T2K CC0π measurement of muon-neutrino interactions on Carbon with the SuSAv2 and Valencia models (1p1h+2p2h) implemented in GENIE with additional pion-absorption effects (from GENIE's Berger-Sehgal model). The top plots are the SuSAv2 predictions whilst the Valencia ones are below. The data points are taken from [295].
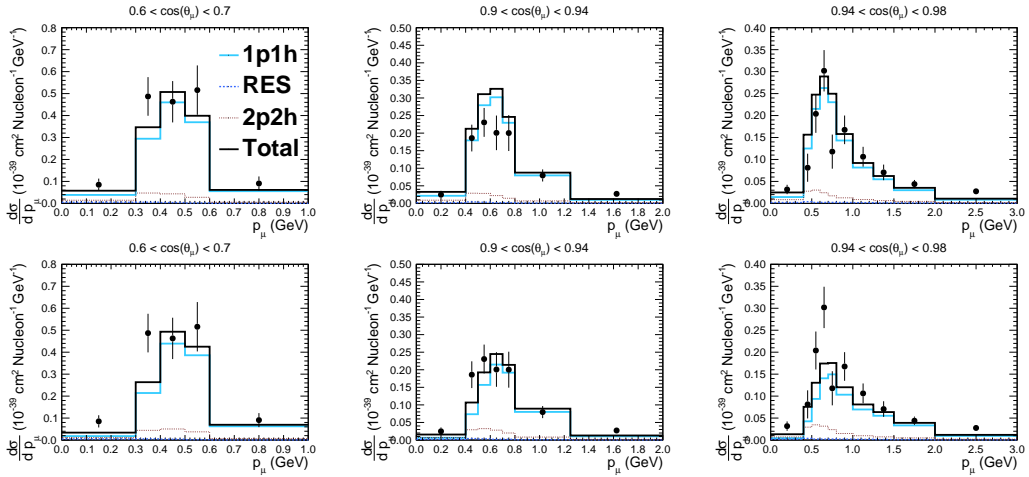

FIG. 51. Comparison of the T2K CC0π measurement of muon-neutrino interactions on Carbon where there are no protons above 500 MeV with the SuSAv2 and Valencia models (1p1h+2p2h) implemented in GENIE with additional pion-absorption effects (from GENIE's Berger-Sehgal model). The top plots are the SuSAv2 predictions whilst the Valencia ones are below. The data points are taken from [328].

drawbacks of the RMF at very high kinematics, constituting a promising candidate to be implemented in neutrino event generators. This will help to reduce nuclear-medium uncertainties and to improve systematics in neutrino oscillation experiments.

VIII. Conclusions

The advent of next generation neutrino oscillation experiments demands more and more sophisticated nuclear modelling, necessary to extract significant information on the properties of neutrinos and physics beyond the Standard Model of electroweak interactions. Nuclear theory plays a crucial role in these analyses, which strongly rely on the
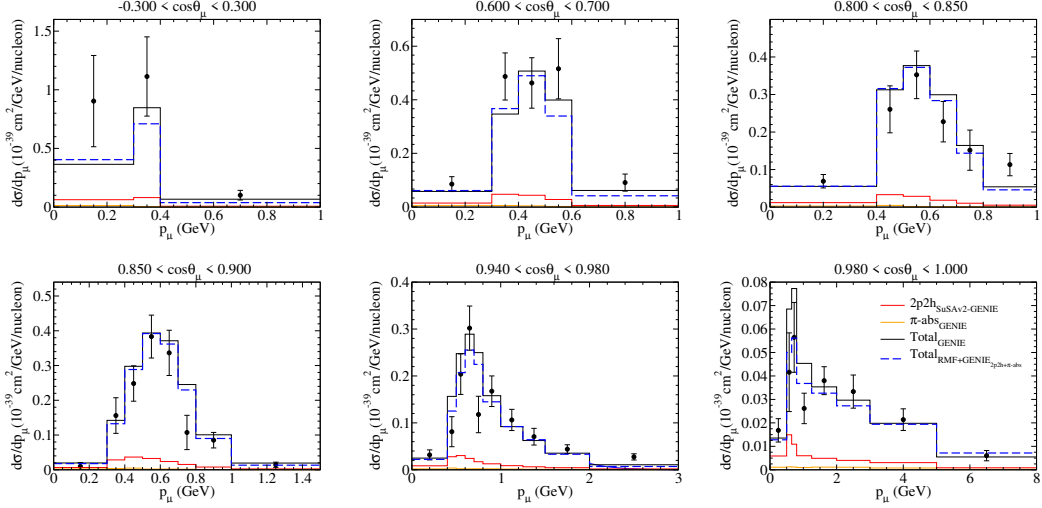
FIG. 52. Comparisons of single differential CC0π muon-neutrino cross sections on Carbon at T2K kinematics as a function of the muon kinematics when there are no protons (with momenta above 500 MeV). Two 1p1h predictions are used (one from RMF, the other from SuSAv2 implemented in GENIE), in addition to the SuSAv2 2p2h and Berger-Sehgal pion absorption contributions from GENIE. Goodness of fit are calculated to be $\chi^2_{RMF} = 171.87$ (59 bins) and $\chi^2_{SuSA} = 168.92$ (60 bins), where the latter includes a single extra bin from -1.0 to -0.3 $\cos\theta$ (not shown). The data points are taken from [328].

accurate description of neutrino interactions with the detector, made of medium/heavy nuclei, implemented in Monte Carlo generators.

Contrary to the case of electron scattering, where many precise data from previous experiments exist, neutrino scattering data are rare and have large error bars. Beyond that, the identification of the primary reaction suffers from the absence of monochromatic neutrino beams. Therefore, electron scattering represents not only a necessary test but also a useful tool to understand and control nuclear effects in oscillation experiments.

In this paper we have reviewed the current status of the description of lepton-nucleus scattering at different kinematics, going from the quasi-elastic up to the deep-inelastic regime. We have focused in particular on the SuSAv2+MEC model, developed and improved by our group, collecting the main results obtained in the last few years. The model is based on the Relativistic Mean Field description of the nucleus, complemented with the contribution of two-body currents. We have shown that the model is capable of describing in a very satisfactory way both electron and neutrino data in the case of inclusive reactions, in which only the outgoing lepton is detected. This outcome, although reassuring, is not sufficient to guarantee the required precision - of a few % - on the description of nuclear effects in neutrino oscillation experiments. Work is in progress on the study of exclusive reactions, where one or more hadrons are detected in coincidence with the lepton, in the same relativistic framework. The extension of nuclear models to semi-inclusive reactions is a challenge to be faced by theorists working in the field. A proper description of the hadrons and mesons in the final state will be essential for the next-generation of neutrino experiments. This requires having a reasonable control on the reconstruction of the energy neutrino which can be only achieved by analyzing the kinematics of the final particles.

A. Scaling and superscaling: definitions

In this appendix we recall the definitions of the scaling and superscaling functions, along with the ψ-scaling variable [18–20, 22, 331] for inclusive electron scattering off a nucleus. We work in the target rest frame and we use fully relativistic kinematics.

The scaling variable ψ naturally emerges in the Relativistic Fermi Gas calculation of the quasielastic responses (see Sect. III A and Appendix C). It is defined in terms of the lowest kinetic energy $T_{min} \equiv T_{min}(q,\omega)$ of the struck nucleon inside the Fermi sphere for given q and ω, according to Eqs (43,44))

$$\psi = \pm\sqrt{\frac{T_{min}}{T_F}} = \text{sgn}(\lambda - \tau)\sqrt{\frac{\epsilon_0 - 1}{\epsilon_F - 1}}, \tag{A1}$$

where $\epsilon_F = (k_F^2 + m_N^2)^{\frac{1}{2}}/m_N$, k_F being the Fermi momentum, and

$$\epsilon_0 = \text{Max}\left\{\kappa\sqrt{1 + \frac{1}{\tau}} - \lambda, \epsilon_F - 2\lambda\right\}. \tag{A2}$$

We recall the definition of the dimensionless energy, momentum and four-momentum transfers,

$$\lambda = \omega/2m_N, \quad \kappa = q/2m_N, \quad \tau = \kappa^2 - \lambda^2. \tag{A3}$$

The second value inside the Max in (A2) takes into account Pauli blocking, which prevents the ejected nucleon from occupying a state with $k < k_F$. For $q > 2k_F$ no Pauli blocking effects are present in the RFG model and $\epsilon_0 = \kappa\sqrt{1 + 1/\tau}$.

The variable ψ vanishes at the QEP and is negative (positive) for transferred energies lower (higher) than the energy of the maximum of the QEP

$$\omega_{QEP} = \sqrt{q^2 + m_N^2} - m_N. \tag{A4}$$

When comparing to experimental data one finds that the maximum of the QEP is shifted by the nucleon separation energy. This energy shift E_{shift} is taken into account by modifying the scaling variable $\psi \to \psi'$, with λ replaced by $\lambda' = (\omega - E_{shift})/(2m_N)$ and likewise $\tau \to \tau' = \kappa^2 - \lambda'^2$.

An alternative expression for ψ, valid only in the non Pauli-blocked regime (the interesting regime for scaling arguments) is

$$\psi = \frac{1}{\sqrt{\xi_F}} \frac{\lambda - \tau}{\sqrt{(1+\lambda)\tau + \kappa\sqrt{\tau(1+\tau)}}}, \tag{A5}$$

where $\xi_F = \epsilon_F - 1$.

The variable ψ can be extended to the inelastic region. For the excitation of a resonance N^* of mass m^* one can introduce the inelasticity function [264]

$$\rho = 1 + \frac{\mu^2 - 1}{4\tau}, \quad \mu = \frac{m^*}{m_N} \tag{A6}$$

through the replacements

$$\lambda \to \lambda\rho, \quad \kappa \to \kappa\rho, \quad \tau \to \tau\rho^2 \tag{A7}$$

in (A5). This yields the resonance scaling variable

$$\psi^* = \frac{1}{\sqrt{\xi_F}} \frac{\lambda - \tau\rho}{\sqrt{(1+\lambda\rho)\tau + \kappa\sqrt{\tau(1+\tau\rho^2)}}}. \tag{A8}$$

Likewise, the inelastic scaling variable ψ_X can be defined for any inelastic channel by setting $\mu = \mu_X = \frac{W_X}{m_N}$, being W_X the invariant mass of the final state.

The *superscaling function* becomes a function the variable ψ only if superscaling occurs. It is defined as

$$f(q,\omega) = k_F \frac{d^2\sigma/d\Omega_e d\omega}{\overline{\sigma}_{eN}}, \tag{A9}$$

where $d^2\sigma/d\Omega_e d\omega$ is the double differential cross section with respect to the outgoing electron solid angle Ω_e and energy transfer ω. The dividing factor is some average value of the single-nucleon cross section compatible with the kinematics. Note that $\overline{\sigma_{eN}}$ is not the free stationary elastic eN cross section, because the hit nucleon is moving inside the nucleus and it is off-shell. The treatment of off-shell effects introduces ambiguities which are more or less important depending on the kinematics. In this work we use the averaged single-nucleon cross section arising from the RFG model, given by

$$\overline{\sigma_{eN}} = \sigma_{Mott}(v_L G_L + v_T G_T) \tag{A10}$$

$$G_{L,T} = \frac{\xi_F}{\eta_F^2 \kappa}(Z U_{L,T}^p + N U_{L,T}^n), \tag{A11}$$

where the proton and neutron structure functions $U_{L,T}^{p,n}$ are defined in Eqs. (49,50).

B. Single nucleon tensor

In this appendix we derive the single nucleon tensor and responses for a nucleon transition $\mathbf{p} \to \mathbf{p}'$ in the Fermi gas before integration. The starting point is the single nucleon tensor given in Eq. (22). We consider for definiteness the tensor induced by the weak CC interaction, which is the sum of vector and axial currents, given in Eqs. (24,25). The electromagnetic tensor can easily obtained from the below expressions by considering only the vector part of the current.

We start, using the properties of the Dirac spinors, writing the sum over spin indices in Eq. (22 as a trace of Dirac matrices

$$w_{s.n.}^{\mu\nu}(\mathbf{p}',\mathbf{p}) = \frac{1}{2}\text{Tr}\left[\frac{\not{p}+m_N}{2m_N}(\Gamma_V - \widetilde{\Gamma}_A)^\mu \frac{\not{p}'+m_N}{2m_N}(\Gamma_V - \Gamma_A)^\nu\right], \tag{B1}$$

where Γ_V^μ is the spin matrix of the vector current after using Gordon identity

$$\Gamma_V^\mu = 2G_M^V \gamma^\mu - 2F_2^V \frac{(p+p')^\mu}{2m_N}, \tag{B2}$$

while Γ_A^μ is the spin matrix of the axial current

$$\Gamma_A^\mu = G_A \gamma^\mu \gamma^5 + G_P \frac{Q^\mu}{2m_N}\gamma^5. \tag{B3}$$

Finally $\widetilde{\Gamma}_A^\mu = \gamma^0 \Gamma_A^{\mu\dagger}\gamma^0$ or

$$\widetilde{\Gamma}_A^\mu = G_A \gamma^\mu \gamma^5 - G_P \frac{Q^\mu}{2m_N}\gamma^5. \tag{B4}$$

We see that the $V - A$ dependence of the weak current allows to single out four contributions labeled VV, AA, VA and AV

$$w_{s.n.}^{\mu\nu}(\mathbf{p}',\mathbf{p}) = w_{VV}^{\mu\nu} + w_{AA}^{\mu\nu} + w_{VA}^{\mu\nu} + w_{AV}^{\mu\nu}. \tag{B5}$$

Performing the corresponding traces, it is straightforward to obtain the result:

$$w_{VV}^{\mu\nu} = \frac{1}{m_N^2}\left[(G_M^V)^2(Q^2 g^{\mu\nu} - Q^\mu Q^\nu) + \left((F_1^V)^2 + \tau(F_2^V)^2\right)(p+p')^\mu(p+p')^\nu\right] \tag{B6}$$

$$w_{AA}^{\mu\nu} = \frac{1}{4m_N^2}\left[G_A^2\left((p+p')^\mu(p+p')^\nu - Q^\mu Q^\nu - \left(4m_N^2 - Q^2\right)g^{\mu\nu}\right) - \left(2G_A G_P + G_P^2 \frac{Q^2}{4m_N^2}\right)Q^\mu Q^\nu\right] \tag{B7}$$

$$w_{VA}^{\mu\nu} + w_{AV}^{\mu\nu} = i\frac{2G_M^V G_A}{m_N^2}\epsilon^{\alpha\beta\mu\nu}p_\alpha p'_\beta. \tag{B8}$$

Note that the VA interference tensor is purely imaginary and antisymmetric and therefore it only contributes to the T' response function, see Eqs. (37-41).

Using $p'_\mu = p_\mu + Q_\mu$ we can write the hadronic tensor in the more standard form

$$w^{\mu\nu}_{s.n.} = -w_1\left(g^{\mu\nu} - \frac{Q^\mu Q^\nu}{Q^2}\right) + w_2 K^\mu K^\nu - \frac{i}{m_N}w_3\epsilon^{\alpha\beta\mu\nu}Q_\alpha K_\beta + w_4\frac{Q^\mu Q^\nu}{m_N^2}, \tag{B9}$$

where the invariant structure functions $w_i = w_i(Q^2)$ only depend on Q^2, and we have defined the four vector

$$K^\mu = \frac{1}{m_N}\left(p^\mu - \frac{p \cdot Q}{Q^2}Q^\mu\right). \tag{B10}$$

After a straightforward calculation, using Eqs. (B6,B7,B8), we obtain

$$w_1 = \tau(2G_M^V)^2 + (1+\tau)G_A^2 \tag{B11}$$

$$w_2 = \frac{(2G_E^V)^2 + \tau(2G_M^V)^2}{1+\tau} + G_A^2 \tag{B12}$$

$$w_3 = 2G_M^V G_A \tag{B13}$$

$$w_4 = \frac{1}{4\tau}(G_A - \tau G_P)^2. \tag{B14}$$

Finally we extract the suitable components of the hadron tensor to obtain the corresponding single nucleon responses to be used later for computing the nuclear responses in the RFG.

The single-nucleon CC response function, using Eq. (B9), can be written as

$$r_{CC} = w^{00}_{s.n.} = -w_1\left(1 - \frac{\omega^2}{Q^2}\right) + w_2(K^0)^2 + w_4\frac{\omega^2}{m_N^2}. \tag{B15}$$

Writing it in terms of the dimensionless variables λ, κ, τ, introduced in Eq. (A3), and the reduced initial nucleon energy $\varepsilon \equiv E/m_N$, we find

$$r_{CC} = -w_1\frac{\kappa^2}{\tau} + w_2(\varepsilon + \lambda)^2 + 4w_4\lambda^2. \tag{B16}$$

Analogously, for the case of the CL and LL single-nucleon responses

$$r_{CL} = -\frac{1}{2}(w^{03}_{s.n.} + w^{30}_{s.n.}) = -\frac{\lambda}{\kappa}\left[-w_1\frac{\kappa^2}{\tau} + w_2(\varepsilon + \lambda)^2\right] - 4w_4\lambda\kappa \tag{B17}$$

$$r_{LL} = w^{33}_{s.n.} = \frac{\lambda^2}{\kappa^2}\left[-w_1\frac{\kappa^2}{\tau} + w_2(\varepsilon + \lambda)^2\right] + 4w_4\kappa^2. \tag{B18}$$

Note that the first term of r_{CL}, between squared parentheses, and multiplied by $-\lambda/\kappa$, comes from current conservation of the terms with w_1 and w_2 of the hadronic tensor. The same comment applies to the first term of the r_{LL} response, with the factor λ^2/κ^2.

The transverse response is the component

$$r_T = w^{11}_{s.n.} + w^{22}_{s.n.} = 2w_1 + w_2[(K^1)^2 + (K^2)^2]. \tag{B19}$$

Using the definition of the vector K^μ, Eq. (B10), we have

$$(K^1)^2 + (K^2)^2 = \eta^2 - \eta_3^2, \tag{B20}$$

where $\eta_i = p_i/m_N$ is the reduced initial nucleon momentum vector with length η. Using the condition for on-shell nucleons $\mathbf{p} \cdot \mathbf{q} = E\omega + Q^2/2$ written in terms of dimensionless variables

$$\eta_3 = \frac{\varepsilon\lambda - \tau}{\kappa} \tag{B21}$$

and $\eta^2 = \varepsilon^2 - 1$, we can finally write

$$r_T = 2w_1 + w_2\frac{\varepsilon^2\tau - \kappa^2 - \tau^2 + 2\varepsilon\lambda\tau}{\kappa^2}. \tag{B22}$$

Finally, the $r_{T'}$ response comes from the antisymmetric part of the hadronic tensor[15]

$$r_{T'} = -\frac{i}{2}(w_{s.n}^{12} - w_{s.n}^{21}) = -\frac{1}{m_N}w_3(-qK^0 + \omega K^3).$$ (B23)

Using $K^0 = \varepsilon + \lambda$ and $K^3 = \omega K^0/q$, we obtain

$$r_{T'} = 2w_3\frac{\tau}{\kappa}(\varepsilon + \lambda).$$ (B24)

C. Derivation of response functions in the RFG model

We outline here the main steps used to obtain the analytical expression of the response functions in the RFG, as this material can only be found for electron scattering and not for neutrino scattering in such detailed form.

We start with the definition of the response function R_K for neutrino (antineutrino) CC quasielastic scattering. Taking the corresponding components of the hadronic tensor from Eq. (21), we have

$$R_K(q,\omega) = \frac{3\mathcal{N}m_N^2}{4\pi k_F^3}\int d^3p\,\delta(E'-E-\omega)\frac{1}{EE'}r_K(\mathbf{p},q,\omega)\theta(k_F-p)\theta(p'-k_F),$$ (C1)

where $\mathcal{N} = N$ for neutrinos and Z for antineutrinos. The single nucleon responses r_K have been obtained in the previous appendix B for on shell nucleons with momenta $\mathbf{p}' = \mathbf{p} + \mathbf{q}$. Note that r_K depends on q,ω via the variables κ, λ, and τ, and that it depends on $\mathbf{p}$ only through the reduced initial energy ε, see Eqs. (B16, B17, B18, B22, B24).

To perform the integral over the initial nucleon momentum, we change variables $(p,\theta,\phi) \longrightarrow (E,E',\phi)$, where $E^2 = m_N^2 + \mathbf{p}^2$ and $E'^2 = m_N^2 + (\mathbf{p}+\mathbf{q})^2$ are the initial and final nucleon energies. The volume element transforms as

$$d^3p = \frac{EE'}{q}dEdE'd\phi$$ (C2)

and the integral with the appropriate integration limits becomes

$$R_K(q,\omega) = \frac{3\mathcal{N}m_N^2}{4\pi k_F^3}\frac{1}{q}\int_{m_N}^{E_F}dE\int_{E_{p-q}}^{E_{p+q}}dE'\int_0^{2\pi}d\phi\,\delta(E'-E-\omega)r_K(\mathbf{p},q,\omega)\theta(E'-E_F),$$ (C3)

where E_F is the relativistic Fermi energy, $E_{p+q}^2 = m_N^2 + (p+q)^2$, and $E_{p-q}^2 = m_N^2 + (p-q)^2$. The integral over ϕ gives a factor 2π because the single nucleon responses do not depend on the azimuthal angle. Using the delta function to integrate over $E' = E + \omega$, the result can be written as an integral over the initial energy

$$R_K(q,\omega) = \frac{3\mathcal{N}}{4\eta_F^3\kappa m_N^2}\int_{m_N}^{E_F}dE\,\theta(E_{p+q}-E-\omega)\theta(E+\omega-E_{p-q})\theta(E'-E_F)r_K(E,q,\omega),$$ (C4)

where we have used the reduced variable $\eta_F = k_F/m_N$ and $\kappa = q/2m_N$. Note that the single nucleon responses only depend on the initial energy.

The step functions and the integration limits are equivalent to the following constraints to the energy:

$$E_{p-q} < E + \omega < E_{p+q}$$ (C5)
$$E_F < E + \omega < E_F + \omega.$$ (C6)

Taking the square of (C5) and introducing the reduced variables: momentum, $\eta = p/m_N$, energy, ε and λ, κ and τ, it is straightforward to obtain

$$|\varepsilon\lambda - \tau| < \kappa\eta$$ (C7)

which in turn can be squared again, using $\eta^2 = \varepsilon^2 - 1$, in terms of ε, yielding

$$\kappa^2\left(1 + \frac{1}{\tau}\right) < (\varepsilon + \lambda)^2.$$ (C8)

---

[15] Our convention is $\epsilon_{0123} = 1$ for the Levi-Civita four tensor.

Solving for ε we get the following lower bound for given q, ω

$$\kappa\sqrt{1 + \frac{1}{\tau}} - \lambda < \varepsilon. \tag{C9}$$

On the other hand, from (C6), ε must verify the Pauli blocking condition as a second lower bound

$$\varepsilon_F - 2\lambda < \varepsilon, \tag{C10}$$

where $\varepsilon_F = E_F/m_N$. Both lower bounds for ε imply

$$\text{Max}\left\{\kappa\sqrt{1 + \frac{1}{\tau}} - \lambda, \varepsilon_F - 2\lambda\right\} \equiv \varepsilon_0 < \varepsilon. \tag{C11}$$

Note now that the following inequality always holds

$$\kappa\sqrt{1 + \frac{1}{\tau}} - \lambda \geq 1. \tag{C12}$$

This can be demonstrated by moving λ to the right-hand side and taking the square on both sides of the inequality. Hence $1 < \varepsilon_0 < \varepsilon$ and therefore ε correspond to an allowed nucleon energy. The response function can thus be written as the following integral over ε

$$R_K(q, \omega) = \frac{3\mathcal{N}}{4\eta_F^3 \kappa m_N} \theta(\varepsilon_F - \varepsilon_0) \int_{\varepsilon_0}^{\varepsilon_F} r_K(\varepsilon, \kappa, \lambda) d\varepsilon. \tag{C13}$$

Note that there is a dependence of the response functions on the variable ε_0 through the lower limit of the integral. In the scaling approach ε_0 is written in terms of the scaling variable ψ, defined by

$$\psi = \sqrt{\frac{\varepsilon_0 - 1}{\varepsilon_F - 1}} \text{sign}(\lambda - \tau). \tag{C14}$$

The scaling variable is defined such as it is positive to the right side of the QE peak ($\lambda = \tau$) and negative otherwise. The inverse relation is

$$\varepsilon_0 = 1 + \psi^2 \xi_F, \tag{C15}$$

where $\xi_F = \varepsilon_F - 1$ is the kinetic Fermi energy in units of the nucleon mass. The single nucleon responses, obtained in App. B, depend on ε as a second-degree polynomial at most. Therefore, in terms of this scaling variable, the only relevant integrals are the following:

$$\int_{\varepsilon_0}^{\varepsilon_F} d\varepsilon = \xi_F(1 - \psi^2) \tag{C16}$$

$$\int_{\varepsilon_0}^{\varepsilon_F} \varepsilon \, d\varepsilon = \xi_F(1 - \psi^2)(1 + \frac{1}{2}\xi_F(1 + \psi^2)) \tag{C17}$$

$$\int_{\varepsilon_0}^{\varepsilon_F} \varepsilon^2 \, d\varepsilon = \xi_F(1 - \psi^2)(1 + \xi_F(1 + \psi^2) + \frac{1}{3}\xi_F^2(1 + \psi^2 + \psi^4)). \tag{C18}$$

Applying these results to the response R_{CC} we can directly write

$$R_{CC} = \frac{3\mathcal{N}}{4m_N \eta_F^3 \kappa} \theta(1 - \psi^2)\xi_F(1 - \psi^2)\left\{-w_1 \frac{\kappa^2}{\tau} + w_2\lambda^2 + 4w_4\lambda^2\right.$$

$$\left. + 2w_2\lambda(1 + \frac{1}{2}\xi_F(1 + \psi^2)) + w_2(1 + \xi_F(1 + \psi^2) + \frac{1}{3}\xi_F^2(1 + \psi^2 + \psi^4))\right\} \tag{C19}$$

$$= \frac{1}{k_F} \frac{\mathcal{N}\xi_F}{\eta_F^2 \kappa} f(\psi) U_{CC}, \tag{C20}$$

where $f(\psi)$ is the RFG scaling function defined in Eq. (42).

To write this expression in terms of the quantity Δ introduced in Eq. (51) we add and subtract the elastic limit of the function U_{CC}, corresponding to $\eta_F = \xi_F = 0$ and $\lambda = \tau$:

$$U_{CC}^0 = U_{CC}(\xi_F = 0, \lambda = \tau) = \frac{\kappa^2}{\tau}\left[-w_1 + (1 + \tau)w_2 + 4\tau w_4 \frac{\lambda^2}{\kappa^2}\right]. \tag{C21}$$

The small quantity Δ, reflecting the deviation from the elastic value due to the Fermi motion of the nucleons, is $U_{CC} - U_{CC}^0 = (\kappa^2/\tau)w_2\Delta$. Therefore

$$U_{CC} = U_{CC}^0 + U_{CC} - U_{CC}^0 = \frac{\kappa^2}{\tau}\left[-w_1 + (1 + \tau)w_2 + 4\tau w_4 \frac{\lambda^2}{\kappa^2} + w_2\Delta\right]. \tag{C22}$$

Finally, we replace the values of the w_i structure functions, given in Eqs. (B11–B14), obtaining Eqs. (52–57).

Proceeding similarly to the R_{CC} responses, we find that all the responses R_{CL}, R_{LL}, R_T and $R_{T'}$ can be factorized as in Eq. (C20),

$$R_K = \frac{1}{k_F}\frac{\mathcal{N}\xi_F}{\eta_F^2 \kappa}f(\psi)U_K. \tag{C23}$$

The functions U_{CL} and U_{LL} can be obtained more easily by writing them as sums of two pieces, coming from the conserved and non-conserved parts of the hadron tensor. First note that

$$U_{CC} = (U_{CC})_{c.} + (U_{CC})_{n.c.}, \tag{C24}$$

where the conserved and non conserved parts are

$$(U_{CC})_{c.} = \frac{\kappa^2}{\tau}[-w_1 + (1 + \tau)w_2 + w_2\Delta] \tag{C25}$$

$$(U_{CC})_{n.c.} = 4\lambda^2 w_4. \tag{C26}$$

Note that the non conserved part $(U_{CC})_{n.c.}$ is precisely the term of r_{CC}, in Eq. (B16), containing the w_4 structure function. This is so because this single-nucleon contribution is independent of ε and it factorizes out of the energy integration. The same can be said for the non conserved parts of r_{CL} and r_{LL} (Eqs. (B17,B18)).

Consequently, applying current conservation to the conserved part, we can write

$$(U_{CL})_{c.} = -\frac{\lambda}{\kappa}(U_{CC})_{c.} \tag{C27}$$

$$(U_{LL})_{c.} = \frac{\lambda^2}{\kappa^2}(U_{CC})_{c.} \tag{C28}$$

On the other hand for the non conserved part due to the factorization property

$$(U_{CL})_{n.c.} = -4\lambda\kappa w_4 \tag{C29}$$

$$(U_{LL})_{n.c.} = 4\kappa^2 w_4. \tag{C30}$$

$$\tag{C31}$$

Proceeding in the same lines for the T response we obtain

$$U_T = 2w_1 - w_2\frac{\kappa^2 + \tau^2}{\kappa^2} + w_2\frac{2\lambda\tau}{\kappa^2}\left[1 + \frac{1}{2}\xi_F(1 + \psi^2)\right] + w_2\frac{\tau}{\kappa^2}\left[1 + \xi_F(1 + \psi^2) + \frac{1}{3}\xi_F^2(1 + \psi^2 + \psi^4)\right] \tag{C32}$$

$$= 2w_1 + w_2\Delta, \tag{C33}$$

where the same term Δ as before is obtained as the deviation from the elastic limit for $k_F = 0$.

Finally, the T' response gives

$$U_{T'} = 2w_3\frac{\tau}{\kappa}\left[1 + \lambda + \frac{1}{2}\xi_F(1 + \psi^2)\right]$$

$$= 2w_3\sqrt{\tau(\tau + 1)}\left[1 + \widetilde{\Delta}\right], \tag{C34}$$

where $\widetilde{\Delta}$ was defined in Eq. (66) and results from adding and subtracting the elastic limit for $k_F = 0$ and $\lambda = \tau$.

[1] S. Boffi, C. Giusti, F. d. Pacati, and M. Radici, *Electromagnetic Response of Atomic Nuclei*, Oxford Studies in Nuclear Physics, Vol. 20. 20 (Clarendon Press, Oxford UK, 1996).

[2] J. D. Walecka, *Theoretical Nuclear And Subnuclear Physics* (Editorial World Scientific Pub. Co. Inc., 2004).

[3] L. Alvarez-Ruso *et al.*, Progress in Particle and Nuclear Physics **100**, 1 (2018).

[4] T. Katori and M. Martini, Journal of Physics G: Nuclear and Particle Physics **45**, 013001 (2017).

[5] T. W. Donnelly and A. S. Raskin, Annals Phys. **169**, 247 (1986).

[6] O. Moreno, T. W. Donnelly, J. W. Van Orden, and W. P. Ford, Phys. Rev. **D90**, 013014 (2014).

[7] M. J. Musolf and T. W. Donnelly, Nucl. Phys. **A546**, 509 (1992), [Erratum: Nucl. Phys.A550,564(1992)].

[8] T. W. Donnelly, M. J. Musolf, W. M. Alberico, M. B. Barbaro, A. De Pace, and A. Molinari, Nucl. Phys. **A541**, 525 (1992).

[9] R. González-Jiménez, J. A. Caballero, and T. W. Donnelly, Phys. Rep. **524**, 1 (2013).

[10] W. M. Alberico, M. B. Barbaro, A. De Pace, T. W. Donnelly, and A. Molinari, Nucl. Phys. **A563**, 605 (1993).

[11] M. B. Barbaro, A. De Pace, T. W. Donnelly, and A. Molinari, Nucl. Phys. **A569**, 701 (1994).

[12] M. B. Barbaro, A. De Pace, T. W. Donnelly, and A. Molinari, Nucl. Phys. **A596**, 553 (1996).

[13] M. B. Barbaro, A. De Pace, T. W. Donnelly, and A. Molinari, Nucl. Phys. **A598**, 503 (1996).

[14] R. González-Jiménez, J. A. Caballero, and T. W. Donnelly, Phys. Rev. **C91**, 045502 (2015).

[15] O. Benhar, D. Day, and I. Sick, Rev. Mod. Phys. **80**, 189 (2008).

[16] H. Dai *et al.* (Jefferson Lab Hall A Collaboration), Phys. Rev. C **98**, 014617 (2018).

[17] H. Dai *et al.* (Jefferson Lab Hall A Collaboration), Phys. Rev. C **99**, 054608 (2019).

[18] T. W. Donnelly and I. Sick, Phys. Rev. Lett. **82**, 3212 (1999).

[19] T. W. Donnelly and I. Sick, Phys. Rev. C **60**, 065502 (1999).

[20] W. M. Alberico, A. Molinari, T. W. Donnelly, E. L. Kronenberg, and J. W. Van Orden, Phys. Rev. **C38**, 1801 (1988).

[21] J. E. Amaro, M. B. Barbaro, J. A. Caballero, T. W. Donnelly, A. Molinari, and I. Sick, Phys. Rev. **C71**, 015501 (2005).

[22] D. B. Day, J. S. McCarthy, T. W. Donnelly, and I. Sick, Ann. Rev. Nucl. Part. Sci. **40**, 357 (1990).

[23] J. Jourdan, Nucl. Phys. **A603**, 117 (1996).

[24] S. Frullani and J. Mougey, Adv. Nucl. Phys. **14**, 1 (1984).

[25] J. J. Kelly, Adv. Nucl. Phys. **23**, 75 (1996).

[26] T. W. Donnelly, J. A. Formaggio, B. R. Holstein, R. G. Milner, and B. Surrow, *Foundations of Nuclear and Particle Physics* (Cambridge University Press, 2017).

[27] T. De Forest, Nucl. Phys. **A392**, 232 (1983).

[28] J. E. Amaro, M. B. Barbaro, J. A. Caballero, T. W. Donnelly, and C. Maieron, Phys. Rev. **C71**, 065501 (2005).

[29] J. E. Amaro, A. M. Lallena, and G. Co', Int. Jour. Mod. Phys. E **3**, 735 (1994).

[30] J. E. Amaro, J. A. Caballero, T. W. Donnelly, A. M. Lallena, E. Moya de Guerra, and J. M. Udias, Nucl. Phys. **A602**, 263 (1996).

[31] J. E. Amaro, M. B. Barbaro, J. A. Caballero, T. W. Donnelly, and J. M. Udias, Phys. Rev. C **75**, 034613 (2007).

[32] J. E. Amaro, M. B. Barbaro, J. A. Caballero, and T. W. Donnelly, Phys. Rev. Lett. **98**, 242501 (2007).

[33] J. A. Caballero, J. E. Amaro, M. B. Barbaro, T. W. Donnelly, C. Maieron, and J. M. Udias, Phys. Rev. Lett. **95**, 252502 (2005).

[34] C. Maieron, M. C. Martínez, J. A. Caballero, and J. M. Udías, Phys. Rev. C **68**, 048501 (2003).

[35] J. A. Caballero, Phys. Rev. C **74**, 015502 (2006).

[36] J. M. Udías, P. Sarriguren, E. Moya de Guerra, E. Garrido, and J. A. Caballero, Phys. Rev. C **48**, 2731 (1993).

[37] J. M. Udías, J. A. Caballero, E. M. de Guerra, J. R. Vignote, and A. Escuderos, Phys. Rev. C **64**, 024614 (2001).

[38] W. Alberico *et al.*, Nucl. Phys. A **623**, 471 (1997).

[39] J. M. Udias, P. Sarriguren, E. Moya de Guerra, and J. A. Caballero, Phys. Rev. **C53**, R1488 (1996).

[40] J. M. Udias, P. Sarriguren, E. Moya de Guerra, E. Garrido, and J. A. Caballero, Phys. Rev. **C51**, 3246 (1995).

[41] J. M. Udias, J. A. Caballero, E. Moya de Guerra, J. E. Amaro, and T. W. Donnelly, Phys. Rev. Lett. **83**, 5451 (1999).

[42] J. A. Caballero, T. W. Donnelly, E. M. de Guerra, and J. Udías, Nuclear Physics A **632**, 323 (1998).

[43] E. Quint, PhD Thesis. University of Amsterdam (1988).

[44] I. Bobeldijk *et al.*, Phys. Rev. Lett. **73**, 2684 (1994).

[45] C. Maieron, T. W. Donnelly, and I. Sick, Phys. Rev. **C65**, 025502 (2002).

[46] J. A. Caballero, J. E. Amaro, M. B. Barbaro, T. W. Donnelly, and J. M. Udias, Phys. Lett. **B653**, 366 (2007).

[47] M. C. Martinez, J. R. Vignote, J. A. Caballero, T. W. Donnelly, E. Moya de Guerra, and J. M. Udias, Phys. Rev. **C69**, 034604 (2004).

[48] M. C. Martinez, J. A. Caballero, and T. W. Donnelly, Nucl. Phys. **A707**, 83 (2002).

[49] M. C. Martinez, J. A. Caballero, and T. W. Donnelly, Nucl. Phys. **A707**, 121 (2002).

[50] A. Meucci, M. B. Barbaro, J. A. Caballero, C. Giusti, and J. M. Udias, Phys. Rev. Lett. **107**, 172501 (2011).

[51] R. González-Jiménez, G. D. Megias, M. B. Barbaro, J. A. Caballero, and T. W. Donnelly, Phys. Rev. C **90**, 035501 (2014).

[52] R. González-Jiménez, M. V. Ivanov, M. B. Barbaro, J. A. Caballero, and J. M. Udias, Phys. Lett. B **718**, 1471 (2013).

[53] J. E. Amaro, M. B. Barbaro, J. A. Caballero, T. W. Donnelly, A. Molinari, and I. Sick, Phys. Rev. C **71**, 015501 (2005).

[54] A. Meucci, J. A. Caballero, C. Giusti, F. D. Pacati, and J. M. Udias, Phys. Rev. **C80**, 024605 (2009).

[55] C. Giusti, A. Meucci, F. D. Pacati, J. A. Caballero, and J. M. Udias, AIP Conf. Proc. **1189**, 107 (2009).

[56] A. Meucci, J. A. Caballero, C. Giusti, and J. M. Udias, Phys. Rev. **C83**, 064614 (2011).

[57] R. González-Jiménez, J. A. Caballero, A. Meucci, C. Giusti, M. B. Barbaro, M. V. Ivanov, and J. M. Udías, Phys. Rev. **C88**, 025502 (2013).

[58] M. V. Ivanov, J. R. Vignote, R. Álvarez-Rodríguez, A. Meucci, C. Giusti, and J. M. Udías, Phys. Rev. C **94**, 014608 (2016).

[59] A. Meucci, C. Giusti, and F. D. Pacati, Nucl. Phys. **A739**, 277 (2004).

[60] A. Meucci, F. Capuzzi, C. Giusti, and F. D. Pacati, Phys. Rev. C **67**, 054601 (2003).

[61] M. Anghinolfi *et al.*, Nucl. Phys. **A602**, 405 (1996).

[62] O. Benhar, N. Farina, H. Nakamura, M. Sakuda, and R. Seki, Phys. Rev. **D72**, 053005 (2005).

[63] M. V. Ivanov, A. N. Antonov, G. D. Megias, J. A. Caballero, M. B. Barbaro, J. E. Amaro, I. R. Simo, T. W. Donnelly, and J. M. Udías, AIP Conf. Proc. **2075**, 070004 (2019), [,227(2019)].

[64] I. Sick, S. Fantoni, A. Fabrocini, and O. Benhar, Phys. Lett. **B323**, 267 (1994).

[65] E. Vagnoni, O. Benhar, and D. Meloni, Phys. Rev. Lett. **118**, 142502 (2017).

[66] N. Rocco, A. Lovato, and O. Benhar, Phys. Rev. **C94**, 065501 (2016).

[67] N. Rocco, A. Lovato, and O. Benhar, Phys. Rev. Lett. **116**, 192501 (2016).

[68] O. Benhar and A. Lovato, Int. J. Mod. Phys. **E24**, 1530006 (2015).

[69] O. Benhar, Phys. Rev. **C87**, 024606 (2013).

[70] N. Rocco, C. Barbieri, O. Benhar, A. De Pace, and A. Lovato, Phys. Rev. **C99**, 025502 (2019).

[71] M. V. Ivanov, A. N. Antonov, J. A. Caballero, G. D. Megias, M. B. Barbaro, E. Moya de Guerra, and J. M. Udías, Phys. Rev. **C89**, 014607 (2014).

[72] A. N. Antonov, M. V. Ivanov, J. A. Caballero, M. B. Barbaro, J. M. Udias, E. Moya de Guerra, and T. W. Donnelly, Phys. Rev. **C83**, 045504 (2011).

[73] A. M. Ankowski and J. T. Sobczyk, Phys. Rev. **C77**, 044311 (2008).

[74] Y. Horikawa, F. Lenz, and N. C. Mukhopadhyay, Phys. Rev. C **22**, 1680 (1980).

[75] J. Sobczyk, N. Rocco, A. Lovato, and J. Nieves, Phys. Rev. C **97**, 035506 (2018).

[76] M. Martini, M. Ericson, G. Chanfray, and J. Marteau, Phys. Rev. **C80**, 065501 (2009).

[77] J. Nieves, I. Ruiz Simo, and M. J. Vicente Vacas, Phys. Lett. B **707**, 72 (2012).

[78] J. E. Amaro *et al.*, Nucl. Phys. A **602**, 263 (1996).

[79] S. Jeschonnek and T. W. Donnelly, Phys. Rev. **C57**, 2438 (1998).

[80] V. Pandey, N. Jachowicz, M. Martini, R. González-Jiménez, J. Ryckebusch, T. Van Cuyck, and N. Van Dessel, Phys. Rev. **C94**, 054609 (2016).

[81] V. Pandey, N. Jachowicz, T. Van Cuyck, J. Ryckebusch, and M. Martini, Phys. Rev. C **92**, 024606 (2015).

[82] T. Van Cuyck, N. Jachowicz, R. González-Jiménez, M. Martini, V. Pandey, J. Ryckebusch, and N. Van Dessel, Phys. Rev. **C94**, 024611 (2016).

[83] M. Martini, N. Jachowicz, M. Ericson, V. Pandey, T. Van Cuyck, and N. Van Dessel, Phys. Rev. **C94**, 015501 (2016).

[84] N. Jachowicz, N. Van Dessel, and A. Nikolakopoulos, J. Phys. G **46**, 084003 (2019).

[85] A. Lovato, S. Gandolfi, J. Carlson, S. C. Pieper, and R. Schiavilla, Phys. Rev. Lett. **117**, 082501 (2016).

[86] A. Lovato, S. Gandolfi, J. Carlson, S. C. Pieper, and R. Schiavilla, Phys. Rev. **C91**, 062501 (2015).

[87] A. Lovato, S. Gandolfi, J. Carlson, E. Lusk, S. C. Pieper, and R. Schiavilla, Phys. Rev. **C97**, 022502 (2018).

[88] S. Pastore *et al.*, Phys. Rev. **C97**, 022501 (2018).

[89] J. E. Lynn, I. Tews, J. Carlson, S. Gandolfi, A. Gezerlis, K. E. Schmidt, and A. Schwenk, Phys. Rev. **C96**, 054007 (2017).

[90] A. Lovato *et al.*, EPJ Web Conf. **113**, 01010 (2016).

[91] J. Carlson *et al.*, Rev. Mod. Phys. **87**, 1067 (2015).

[92] S. Bogner *et al.*, Comput. Phys. Commun. **184**, 2235 (2013).

[93] N. Rocco, L. Alvarez-Ruso, A. Lovato, and J. Nieves, Phys. Rev. C **96**, 015504 (2017).

[94] G. D. Megias, J. E. Amaro, M. B. Barbaro, J. A. Caballero, and T. W. Donnelly, Phys. Rev. D **94**, 013012 (2016).

[95] I. Ruiz Simo, J. E. Amaro, M. B. Barbaro, A. De Pace, J. A. Caballero, and T. W. Donnelly, J. Phys. **G44**, 065105 (2017).

[96] I. Ruiz Simo, C. Albertus, J. E. Amaro, M. B. Barbaro, J. A. Caballero, and T. W. Donnelly, Phys. Rev. D **90**, 033012 (2014).

[97] E. Hernández, J. Nieves, and M. Valverde, Phys. Rev. D **76**, 033005 (2007).

[98] W. M. Alberico, M. Ericson, and A. Molinari, Annals Phys. **154**, 356 (1984).

[99] M. J. Dekker, P. J. Brussaard, and J. A. Tjon, Phys. Rev. **C49**, 2650 (1994).

[100] A. De Pace, M. Nardi, W. M. Alberico, T. W. Donnelly, and A. Molinari, Nucl. Phys. **A726**, 303 (2003).

[101] J. E. Amaro, C. Maieron, M. B. Barbaro, J. A. Caballero, and T. W. Donnelly, Phys. Rev. **C82**, 044601 (2010).

[102] M. Martini, M. Ericson, G. Chanfray, and J. Marteau, Phys. Rev. **C81**, 045502 (2010).

[103] J. Nieves, I. Ruiz Simo, and M. J. Vicente Vacas, Phys. Rev. C **83**, 045501 (2011).

[104] J. E. Amaro, A. M. Lallena, G. Co', and A. Fabrocini, Phys. Rev. **C57**, 3473 (1998).

[105] I. R. Simo, C. Albertus, J. E. Amaro, M. B. Barbaro, J. A. Caballero, and T. W. Donnelly, Phys. Rev. D **90**, 053010 (2014).

[106] J. T. Sobczyk, Phys. Rev. **C86**, 015504 (2012).

[107] G. D. Megias, J. E. Amaro, M. B. Barbaro, J. A. Caballero, T. W. Donnelly, and I. Ruiz Simo, Phys. Rev. D **94**, 093004 (2016).

[108] A. V. Butkevich and S. V. Luchuk, Phys. Rev. **C97**, 045502 (2018).

[109] S. Dolan, G. D. Megias, and S. Bolognesi, (2019), arXiv:1905.08556 [hep-ex].

[110] I. Ruiz Simo, J. E. Amaro, M. B. Barbaro, A. De Pace, J. A. Caballero, G. D. Megias, and T. W. Donnelly, Phys. Lett. **B762**, 124 (2016).

[111] R. Gran, J. Nieves, F. Sanchez, and M. J. Vicente Vacas, Phys. Rev. **D88**, 113007 (2013).

[112] I. Ruiz Simo, J. E. Amaro, M. B. Barbaro, A. De Pace, J. A. Caballero, G. D. Megias, and T. W. Donnelly, Phys. Rev. **C94**, 054610 (2016).

[113] I. Ruiz Simo, J. E. Amaro, M. B. Barbaro, J. A. Caballero, G. D. Megias, and T. W. Donnelly, Phys. Lett. **B770**, 193 (2017).

[114] I. R. Simo, J. E. Amaro, M. B. Barbaro, J. A. Caballero, G. D. Megias, and T. W. Donnelly, Annals Phys. **388**, 323 (2018).

[115] M. V. Ivanov, G. D. Megias, R. González-Jiménez, O. Moreno, M. B. Barbaro, J. A. Caballero, and T. W. Donnelly, Journal of Physics G: Nuclear and Particle Physics **43**, 045101 (2016).

[116] K. Abe *et al.* (T2K Collaboration), Phys. Rev. Lett. **113**, 241803 (2014).

[117] Y. Nakajima *et al.* (SciBooNE Collaboration), Phys. Rev. D **83**, 012005 (2011).

[118] C. Maieron, J. E. Amaro, M. B. Barbaro, J. A. Caballero, T. W. Donnelly, and C. F. Williamson, Phys. Rev. C **80**, 035504 (2009).

[119] J. Amaro, M. Barbaro, J. Caballero, T. Donnelly, and A. Molinari, Nuclear Physics A **657**, 161 (1999).

[120] O. Benhar, D. Day, and I. Sick, arXiv:nucl-ex/0603032 (2006).

[121] P. Barreau *et al.*, Nucl. Phys. **A402**, 515 (1983).

[122] A. A. Aguilar-Arevalo *et al.* (The MiniBooNE Collaboration), Phys. Rev. D **81**, 013005 (2010).

[123] A. A. Aguilar-Arevalo *et al.* (MiniBooNE Collaboration), Phys. Rev. D **83**, 052007 (2011).

[124] A. A. Aguilar-Arevalo *et al.* (MiniBooNE Collaboration), Phys. Rev. D **83**, 052009 (2011).

[125] T. Le *et al.*, Phys. Lett. B **749**, 130 (2015).

[126] B. Eberly *et al.* (MINERvA Collaboration), Phys. Rev. D **92**, 092008 (2015).

[127] C. L. McGivern *et al.* (MINERvA Collaboration), Phys. Rev. D **94**, 052005 (2016).

[128] O. Altinok *et al.*, Phys. Rev. D **96**, 072003 (2017).

[129] J. Wolcott *et al.* (MINERvA Collaboration), Phys. Rev. Lett. **117**, 111801 (2016).

[130] K. Abe *et al.* (T2K Collaboration), Phys. Rev. D **95**, 012010 (2017).

[131] J. T. Sobczyk and J. Żmuda, Phys. Rev. C **91**, 045501 (2015).

[132] U. Mosel and K. Gallmeister, Phys. Rev. C **96**, 015503 (2017).

[133] A. Nikolakopoulos, R. González-Jiménez, K. Niewczas, J. Sobczyk, and N. Jachowicz, Phys. Rev. D **97**, 093008 (2018).

[134] R. González-Jiménez, K. Niewczas, and N. Jachowicz, Phys. Rev. D **97**, 013004 (2018).

[135] L. Alvarez-Ruso, Y. Hayato, and J. Nieves, New Journal of Physics **16**, 075015 (2014).

[136] S. X. Nakamura *et al.*, Reports on Progress in Physics **80**, 056301 (2017).

[137] L. Tiator *et al.*, The European Physical Journal Special Topics **198**, 141 (2011).

[138] C. Fernández-Ramírez, E. M. de Guerra, and J. Udías, Annals of Physics **321**, 1408 (2006).

[139] C. Fernández-Ramírez, E. M. de Guerra, and J. Udías, Physics Letters B **660**, 188 (2008).

[140] W. Rarita and J. Schwinger, Phys. Rev. **60**, 61 (1941).

[141] C. L. Smith, Physics Reports **3**, 261 (1972).

[142] O. Lalakulich, E. A. Paschos, and G. Piranishvili, Phys. Rev. D **74**, 014009 (2006).

[143] E. Hernández, J. Nieves, S. K. Singh, M. Valverde, and M. J. V. Vacas, Phys. Rev. D **77**, 053009 (2008).

[144] T. Leitner, O. Buss, L. Alvarez-Ruso, and U. Mosel, Phys. Rev. C **79**, 034601 (2009).

[145] R. González-Jiménez *et al.*, Phys. Rev. D **95**, 113007 (2017).

[146] V. Pascalutsa and R. Timmermans, Phys. Rev. C **60**, 042201 (1999).

[147] C. Praet, O. Lalakulich, N. Jachowicz, and J. Ryckebusch, Phys. Rev. C **79**, 044603 (2009).

[148] E. Hernández, J. Nieves, and M. J. V. Vacas, Phys. Rev. D **87**, 113009 (2013).

[149] T. J. Leitner, *Neutrino-Nucleus Interactions In A Coupled-Channel Hadronic Transport Model*, Ph.D. thesis, Justus-Liebig-Universität Giessen (2009).

[150] M. Rafi Alam, M. Sajjad Athar, S. Chauhan, and S. K. Singh, International Journal of Modern Physics E **25**, 1650010 (2016).

[151] M. Hilt, B. C. Lehnhart, S. Scherer, and L. Tiator, Phys. Rev. C **88**, 055207 (2013).

[152] D.-L. Yao, L. Alvarez-Ruso, A. N. H. Blin, and M. J. V. Vacas, Phys. Rev. D **98**, 076004 (2018).

[153] D.-L. Yao, L. Alvarez-Ruso, and M. V. Vacas, Physics Letters B **794**, 109 (2019).

[154] J. T. Sobczyk and J. Żmuda, Phys. Rev. C **87**, 065503 (2013).

[155] O. Lalakulich, T. Leitner, O. Buss, and U. Mosel, Phys. Rev. D **82**, 093001 (2010).

[156] M. Kabirnezhad, Phys. Rev. D **97**, 013002 (2018).

[157] K. M. Graczyk and B. E. Kowal, Phys. Rev. D **99**, 053002 (2019).

[158] S. X. Nakamura, H. Kamano, and T. Sato, Phys. Rev. D **92**, 074024 (2015).

[159] G. Fogli and G. Nardulli, Nuclear Physics B **160**, 116 (1979).

[160] D. Rein and L. M. Sehgal, Annals of Physics **133**, 79 (1981).

[161] B. D. Serot and X. Zhang, Phys. Rev. C **86**, 015501 (2012).

[162] H. Kamano, S. X. Nakamura, T.-S. H. Lee, and T. Sato, Phys. Rev. D **86**, 097503 (2012).

[163] H. Kamano, S. X. Nakamura, T.-S. H. Lee, and T. Sato, Phys. Rev. C **88**, 035209 (2013).

[164] S. X. Nakamura, H. Kamano, and T. Sato, Phys. Rev. D **99**, 031301 (2019).

[165] T. Sato, D. Uno, and T.-S. H. Lee, Phys. Rev. C **67**, 065201 (2003).

[166] K. Matsui, T. Sato, and T. S. H. Lee, Phys. Rev. C **72**, 025204 (2005).

[167] D. Drechsel, S. S. Kamalov, and L. Tiator, The European Physical Journal A **34**, 69 (2007).

[168] L. Alvarez-Ruso, E. Hernández, J. Nieves, and M. J. V. Vacas, Phys. Rev. D **93**, 014016 (2016).

[169] E. Hernández and J. Nieves, Phys. Rev. D **95**, 053007 (2017).
[170] J. E. Sobczyk, E. Hernández, S. X. Nakamura, J. Nieves, and T. Sato, Phys. Rev. D **98**, 073001 (2018).
[171] G. M. Radecky *et al.*, Phys. Rev. D **25**, 1161 (1982).
[172] M. Derrick *et al.*, Phys. Lett. B **92**, 363 (1980).
[173] T. Kitagaki *et al.*, Phys. Rev. D **34**, 2554 (1986).
[174] L. Alvarez-Ruso, S. K. Singh, and M. J. Vicente Vacas, Phys. Rev. C **59**, 3386 (1999).
[175] J.-J. Wu, T. Sato, and T.-S. H. Lee, Phys. Rev. C **91**, 035203 (2015).
[176] M. Perl, *High energy hadron physics*, Wiley-Interscience publication (Wiley, 1974).
[177] N. Levy, W. Majerotto, and B. Read, Nuclear Physics B **55**, 493 (1973).
[178] M. Guidal, J.-M. Laget, and M. Vanderhaeghen, Nuclear Physics A **627**, 645 (1997).
[179] R. Omnès and M. Froissart, *Mandelstam Theory and Regge Poles: An Introduction for Experimentalists* (Literary Licensing, LLC, 2012).
[180] M. M. Kaskulov and U. Mosel, Phys. Rev. C **81**, 045202 (2010).
[181] T. Vrancx and J. Ryckebusch, Phys. Rev. C **89**, 025203 (2014).
[182] K. Park *et al.*, The European Physical Journal A **49**, 16 (2013).
[183] J. Sobczyk, J. Nowak, and K. Graczyk, Nucl. Phys. B - Proceedings Supplements **139**, 266 (2005).
[184] O. Buss, T. Gaitanos, K. Gallmeister, H. van Hees, M. Kaskulov, O. Lalakulich, A. Larionov, T. Leitner, J. Weil, and U. Mosel, Physics Reports **512**, 1 (2012), transport-theoretical Description of Nuclear Reactions.
[185] O. Lalakulich, K. Gallmeister, and U. Mosel, Phys. Rev. C **86**, 014607 (2012).
[186] A. Bodek and J. L. Ritchie, Phys. Rev. **D23**, 1070 (1981).
[187] A. Bodek and U. Yang, Nuclear Physics B - Proceedings Supplements **112**, 70 (2002).
[188] T. Sjöstrand *et al.*, Computer Physics Communications **135**, 238 (2001).
[189] P. Brauel *et al.*, Physics Letters B **65**, 181 (1976).
[190] P. Brauel *et al.*, Physics Letters B **65**, 184 (1976).
[191] P. Brauel *et al.*, Physics Letters B **69**, 253 (1977).
[192] P. Brauel *et al.*, Zeitschrift für Physik C Particles and Fields **3**, 101 (1979).
[193] T. Horn *et al.* (Jefferson Lab F_π Collaboration), Phys. Rev. Lett. **97**, 192001 (2006).
[194] V. Tadevosyan *et al.* (Jefferson Lab F_π Collaboration), Phys. Rev. C **75**, 055205 (2007).
[195] A. Airapetian *et al.*, Physics Letters B **659**, 486 (2008).
[196] T. Horn *et al.*, Phys. Rev. C **78**, 058201 (2008).
[197] H. P. Blok *et al.* (Jefferson Lab F_π Collaboration), Phys. Rev. C **78**, 045202 (2008).
[198] X. Qian *et al.*, Phys. Rev. C **81**, 055209 (2010).
[199] https://hallcweb.jlab.org/resdata/database.
[200] C. Wilkinson, P. Rodrigues, S. Cartwright, L. Thompson, and K. McFarland, Phys. Rev. D **90**, 112017 (2014).
[201] S. Ahmad, M. S. Athar, and S. K. Singh, Phys. Rev. D **74**, 073008 (2006).
[202] B. Szczerbinska, T. Sato, K. Kubodera, and T.-S. Lee, Physics Letters B **649**, 132 (2007).
[203] X. Zhang and B. D. Serot, Phys. Rev. C **86**, 035502 (2012).
[204] M. Martini and M. Ericson, Phys. Rev. C **90**, 025501 (2014).
[205] N. Rocco, S. X. Nakamura, T. S. H. Lee, and A. Lovato, Phys. Rev. **C100**, 045503 (2019), arXiv:1907.01093 [nucl-th].
[206] C. Fernández-Ramírez, M. Martínez, J. R. Vignote, and J. Udías, Physics Letters B **664**, 57 (2008).
[207] R. González-Jiménez, A. Nikolakopoulos, N. Jachowicz, and J. M. Udías, Phys. Rev. **C100**, 045501 (2019).
[208] K. S. Kim and L. E. Wright, Phys. Rev. C **68**, 027601 (2003).
[209] A. Meucci, J. A. Caballero, C. Giusti, F. D. Pacati, and J. M. Udías, Phys. Rev. C **80**, 024605 (2009).
[210] K. S. Kim and L. E. Wright, Phys. Rev. C **76**, 044613 (2007).
[211] A. V. Butkevich and S. A. Kulagin, Phys. Rev. C **76**, 045502 (2007).
[212] F. Capuzzi, C. Giusti, and F. Pacati, Nuclear Physics A **524**, 681 (1991).
[213] E. D. Cooper, S. Hama, B. C. Clark, and R. L. Mercer, Phys. Rev. C **47**, 297 (1993).
[214] E. D. Cooper, S. Hama, and B. C. Clark, Phys. Rev. C **80**, 034605 (2009).
[215] A. Nagl, V. Devanathan, and H. Überall, *Nuclear Pion Photoproduction* (Springer-Verlag, 1991).
[216] R. González-Jiménez (2019) arXiv:1905.00535v2 [nucl-th].
[217] M. C. Martínez *et al.*, Phys. Rev. C **73**, 024607 (2006).
[218] L. Tiator and L. E. Wright, Phys. Rev. C **30**, 989 (1984).
[219] T. Leitner, U. Mosel, and S. Winkelmann, Phys. Rev. C **79**, 057601 (2009).
[220] H. Kim, S. Schramm, and C. J. Horowitz, Phys. Rev. C **53**, 2468 (1996).
[221] S. Singh, M. Vicente-Vacas, and E. Oset, Physics Letters B **416**, 23 (1998).
[222] E. Oset and L. Salcedo, Nucl. Phys. A **468**, 631 (1987).
[223] J. Nieves, E. Oset, and C. Garcia-Recio, Nucl. Phys. A **554**, 554 (1993).
[224] A. Gil, J. Nieves, and E. Oset, Nucl. Phys. A **627**, 543 (1997).
[225] O. Lalakulich and U. Mosel, Phys. Rev. C **87**, 014602 (2013).
[226] R. González-Jiménez, T. Van Cuyck, N. Van Dessel, V. Pandey, and N. Jachowicz, JPS Conf. Proc. **12**, 010047 (2016).
[227] J. Cugnon and M.-C. Lemaire, Nuclear Physics A **489**, 781 (1988).
[228] P. Arve and J. Helgesson, Nuclear Physics A **572**, 600 (1994).
[229] T.-S. H. Lee, Phys. Rev. C **54**, 1350 (1996).

[230] H. Kim, S. Schramm, and S. H. Lee, Phys. Rev. C **56**, 1582 (1997).

[231] S. Ghosh, S. Sarkar, and S. Mitra, Phys. Rev. D **95**, 056010 (2017).

[232] T. Golan, C. Juszczak, and J. T. Sobczyk, Phys. Rev. C **86**, 015505 (2012).

[233] L. Salcedo, E. Oset, M. Vicente-Vacas, and C. Garcia-Recio, Nucl. Phys. A **484**, 557 (1988).

[234] K. Niewczas and J. T. Sobczyk, Phys. Rev. C **100**, 015505 (2019).

[235] O. Lalakulich, E. A. Paschos, and G. Piranishvili, Phys. Rev. **D74**, 014009 (2006), arXiv:hep-ph/0602210 [hep-ph].

[236] V. D. Burkert and T. S. H. Lee, Int. J. Mod. Phys. **E13**, 1035 (2004).

[237] V. D. Burkert, R. De Vita, M. Battaglieri, M. Ripani, and V. Mokeev, Phys. Rev. **C67**, 035204 (2003).

[238] I. G. Aznauryan, V. D. Burkert, H. Egiyan, K. Joo, R. Minehart, and L. C. Smith, Phys. Rev. **C71**, 015201 (2005).

[239] L. Tiator *et al.*, Eur. Phys. J. **A19**, 55 (2004).

[240] D. Drechsel, O. Hanstein, S. S. Kamalov, and L. Tiator, Nucl. Phys. **A645**, 145 (1999).

[241] O. Lalakulich and E. A. Paschos, Acta Phys. Polon. **B37**, 2311 (2006).

[242] O. Lalakulich and E. A. Paschos, Phys. Rev. **D71**, 074003 (2005).

[243] T. Leitner, L. Alvarez-Ruso, and U. Mosel, Phys. Rev. **C73**, 065502 (2006).

[244] M. Rafi Alam, M. Sajjad Athar, S. Chauhan, and S. K. Singh, Int. J. Mod. Phys. **E25**, 1650010 (2016).

[245] M. Rafi Alam, I. Ruiz Simo, L. Alvarez-Ruso, M. Sajjad Athar, and M. J. Vicente Vacas, AIP Conf. Proc. **1680**, 020001 (2015).

[246] M. Rafi Alam, L. Alvarez-Ruso, M. Sajjad Athar, and M. J. Vicente Vacas, AIP Conf. Proc. **1663**, 120014 (2015).

[247] R. P. Feynman, M. Kislinger, and F. Ravndal, Phys. Rev. **D3**, 2706 (1971).

[248] P. Stowell *et al.* (MINERvA), Phys. Rev. **D100**, 072005 (2019).

[249] C. Andreopoulos *et al.*, Nucl. Instrum. Meth. **A614**, 87 (2010).

[250] C. Andreopoulos *et al.*, (2015), arXiv:1510.05494 [hep-ph].

[251] Y. Hayato, Acta Phys. Polon. **B40**, 2477 (2009).

[252] D. Casper, Nucl. Phys. Proc. Suppl. **112**, 161 (2002), [,161(2002)].

[253] K. S. Kuzmin, V. V. Lyubushkin, and V. A. Naumov, Mod. Phys. Lett. **A19**, 2815 (2004), [,125(2003)].

[254] K. S. Kuzmin, V. V. Lyubushkin, and V. A. Naumov, Nucl. Phys. Proc. Suppl. **139**, 158 (2005), [,158(2004)].

[255] S. Singh and M. Vicente Vacas, Phys. Rev. D **74**, 053009 (2006), arXiv:hep-ph/0606235.

[256] M. Rafi Alam, I. Ruiz Simo, M. Sajjad Athar, and M. J. Vicente Vacas, Phys. Rev. **D82**, 033001 (2010).

[257] G. Adera, B. Van Der Ventel, D. van Niekerk, and T. Mart, Phys. Rev. C **82**, 025501 (2010), arXiv:1112.5748 [nucl-th].

[258] M. R. Alam, I. R. Simo, M. S. Athar, and M. J. Vicente Vacas, Phys. Rev. **D85**, 013014 (2012).

[259] M. Rafi Alam and I. Ruiz Simo, Phys. Rev. **D100**, 033001 (2019).

[260] M. Rafi Alam, I. Ruiz Simo, M. Sajjad Athar, and M. J. Vicente Vacas, Phys. Rev. **D87**, 053008 (2013).

[261] A. Fatima, M. S. Athar, and S. Singh, Front. in Phys. **7**, 13 (2019), arXiv:1807.08314 [hep-ph].

[262] A. Fatima, M. Sajjad Athar, and S. Singh, Phys. Rev. D **98**, 033005 (2018), arXiv:1806.08597 [hep-ph].

[263] F. Akbar, M. Sajjad Athar, A. Fatima, and S. Singh, Eur. Phys. J. A **53**, 154 (2017), arXiv:1704.04580 [hep-ph].

[264] M. B. Barbaro, J. A. Caballero, T. W. Donnelly, and C. Maieron, Phys. Rev. **C69**, 035502 (2004).

[265] A. Bodek and J. L. Ritchie, Phys. Rev. **D24**, 1400 (1981).

[266] A. Bodek *et al.*, Phys. Rev. **D20**, 1471 (1979).

[267] S. Stein *et al.*, Phys. Rev. **D12**, 1884 (1975).

[268] M. E. Christy and P. E. Bosted, Phys. Rev. C **81**, 055213 (2010).

[269] P. E. Bosted and M. E. Christy, Phys. Rev. C **77**, 065206 (2008).

[270] G. D. Megias, Ph.D. thesis, University of Seville, Spain (2017).

[271] S. Bilenky, *Basics of introduction to Feynman diagrams and Electroweak interaction Physics* (Frontières, 1994).

[272] M. Glueck, E. Reya, and A. Vogt, Eur. Phys. J. C **5**, 461 (1998).

[273] E. Perez and E. Rizvi, Rep. Prog. Phys. **76**, 046201 (2013).

[274] Particle Data Group Collaboration, K. Nakamura, *et al.*, J. Phys. G **37**, 075021 (2010).

[275] A. W. Thomas and W. Weise, *The Structure of the Nucleon* (Wiley-VCH Verlag Berlin GmbH, 2001).

[276] H. Haider, M. Sajjad-Athar, S. K. Singh, and I. Ruiz-Simo, Nucl. Phys. A **940**, 138 (2015).

[277] T. Hobbs and W. Melnitchouk, Phys. Rev. D **77**, 114023 (2008).

[278] J. H. Kim *et al.*, Phys. Rev. Lett. **81**, 3595 (1998).

[279] CCFR Collaboration, J. H. Kim, *et al.*, Phys. Rev. Lett. **79**, 1213 (1997).

[280] M. Ghermann, R. G. Ross, and M. R. Whalley, J. Phys. G **25**, 12 (1999).

[281] O. Benhar, D. Day, and I. Sick, Rev. Mod. Phys. **80**, 189 (2008).

[282] E. L. Lomon, Phys. Rev. C **64**, 035204 (2001).

[283] E. L. Lomon, Phys. Rev. C **66**, 045501 (2002).

[284] C. Crawford *et al.*, Phys. Rev. C **82**, 045211 (2010).

[285] G. D. Megias, J. E. Amaro, M. B. Barbaro, J. A. Caballero, and T. W. Donnelly, Phys. Lett. B **725**, 170 (2013).

[286] J. Morgenstern and Z. E. Meziani, Phys. Lett. **B515**, 269 (2001).

[287] J. E. Amaro, G. Co', and A. M. Lallena, arXiv:nucl-th/9902072 (1999).

[288] A. Meucci, M. Vorabbi, P. Finelli, C. Giusti, and F. D. Pacati, Phys. Rev. C **87**, 054620 (2013).

[289] J. E. Amaro, M. B. Barbaro, J. A. Caballero, A. De Pace, T. W. Donnelly, G. D. Megias, and I. Ruiz Simo, Phys. Rev. **C95**, 065502 (2017).

[290] J. S. O'Connell *et al.*, Phys. Rev. **C35**, 1063 (1987).

[291] C. Williamson *et al.*, Phys. Rev. C **56**, 3152 (1997).

[292] Z. E. Meziani *et al.*, Phys. Rev. Lett. **52**, 2130 (1984).
[293] M. B. Barbaro, A. De Pace, T. W. Donnelly, J. A. Caballero, G. D. Megias, and J. W. Van Orden, Phys. Rev. **C98**, 035501 (2018).
[294] M. B. Barbaro, J. A. Caballero, A. De Pace, T. W. Donnelly, R. González-Jiménez, and G. D. Megias, Phys. Rev. **C99**, 042501 (2019).
[295] K. Abe *et al.* (T2K), Phys. Rev. **D93**, 112012 (2016).
[296] K. Abe *et al.* (T2K Collaboration), Phys. Rev. D **97**, 012001 (2018).
[297] C. E. Patrick *et al.* (MINERvA), Phys. Rev. **D97**, 052002 (2018).
[298] D. Ruterbories *et al.* (MINERvA), Phys. Rev. **D99**, 012004 (2019).
[299] A. A. Aguilar-Arevalo *et al.* (MiniBooNE Collaboration), Phys. Rev. D **81**, 092005 (2010).
[300] A. A. Aguilar-Arevalo *et al.* (MiniBooNE Collaboration), Phys. Rev. D **88**, 032001 (2013).
[301] M. Martini, M. Ericson, and G. Chanfray, Phys. Rev. D **85**, 093012 (2012).
[302] K. Gallmeister, U. Mosel, and J. Weil, Phys. Rev. C **94**, 035502 (2016).
[303] A. Meucci and C. Giusti, Phys. Rev. D **85**, 093002 (2012).
[304] A. Meucci and C. Giusti, Phys. Rev. D **91**, 093004 (2015).
[305] A. V. Butkevich and S. V. Luchuk, Phys. Rev. D **99**, 093001 (2019).
[306] M. Martini, M. Ericson, and G. Chanfray, Phys. Rev. C **84**, 055502 (2011).
[307] J. Nieves, I. Ruiz Simo, and M. J. Vicente Vacas, Phys. Lett. B **721**, 90 (2013).
[308] M. Martini and M. Ericson, Phys. Rev. C **87**, 065501 (2013), arXiv:1303.7199 [nucl-th].
[309] U. Mosel, O. Lalakulich, and K. Gallmeister, Phys. Rev. D **89**, 093003 (2014), arXiv:1402.0297 [nucl-th].
[310] A. Meucci and C. Giusti, Phys. Rev. **D89**, 117301 (2014).
[311] M. Ericson and M. Martini, Phys. Rev. C **91**, 035501 (2015).
[312] U. Mosel and K. Gallmeister, Phys. Rev. C **97**, 045501 (2018).
[313] S. Dolan, U. Mosel, K. Gallmeister, L. Pickering, and S. Bolognesi, Phys. Rev. C **98**, 045502 (2018).
[314] G. D. Megias, J. E. Amaro, M. B. Barbaro, J. A. Caballero, T. W. Donnelly, I. Ruiz-Simo, and J. W. V. Orden, Journal of Physics G: Nucl. Part. Phys. **46**, 015104 (2018).
[315] R. González-Jiménez, M. B. Barbaro, J. A. Caballero, T. W. Donnelly, N. Jachowicz, G. D. Megias, K. Niewczas, A. Nikolakopoulos, and J. M. Udías, Phys. Rev. C **101**, 015503 (2020).
[316] K. Abe *et al.* (T2K), (2020), arXiv:2004.05434 [hep-ex].
[317] G. D. Megias, M. B. Barbaro, J. A. Caballero, and S. Dolan, Phys. Rev. D **99**, 113002 (2019).
[318] G. D. Megias, M. V. Ivanov, R. González-Jiménez, M. B. Barbaro, J. A. Caballero, T. W. Donnelly, and J. M. Udías, Phys. Rev. D **89**, 093002 (2014).
[319] V. Lyubushkin *et al.* (NOMAD Collaboration), Eur. Phys. J. C **63**, 355 (2009).
[320] F. Iachello, A. Jackson, and A. Lande, Phys. Lett. **B43**, 191 (1973).
[321] R. Bijker and F. Iachello, Phys. Rev. **C69**, 068201 (2004).
[322] Q. Wan and F. Iachello, Int. J. Mod. Phys. **A20**, 1846 (2005).
[323] F. Iachello and Q. Wan, Phys. Rev. **C69**, 055204 (2004).
[324] R. Bijker, J. Phys. **G32**, L49 (2006).
[325] E. Tomasi-Gustafsson, G. Gakh, and C. Adamuscin, Phys. Rev. **C73**, 045204 (2006).
[326] C. Adamuscin, E. Tomasi-Gustafsson, E. Santopinto, and R. Bijker, Phys. Rev. **C78**, 035201 (2008).
[327] G. D. Megias, S. Bolognesi, M. B. Barbaro, and E. Tomasi-Gustafsson, (2019), arXiv:1910.13263 [hep-ph].
[328] K. Abe *et al.* (T2K), Phys. Rev. **D98**, 032003 (2018).
[329] X.-G. Lu *et al.* (MINERvA Collaboration), Phys. Rev. Lett. **121**, 022504 (2018).
[330] C. Berger and L. M. Sehgal, Phys. Rev. D **76**, 113004 (2007).
[331] M. B. Barbaro, R. Cenni, A. De Pace, T. W. Donnelly, and A. Molinari, Nucl. Phys. **A643**, 137 (1998).